Development of Additive Manufacturing Technology using High-power Diode Laser and Hot-wire Method

（高出力半導体レーザとホットワイヤ法を用いた高能率 AM 技術の開発）

September, 2022

ZHU SONG

Department of Mechanical Science and Engineering
Graduate School of Engineering
Hiroshima University

Abstract

Recently, additive manufacturing (AM) is a family of new techniques that have developed rapidly in various industries, such as aerospace, automobile, and marine due to the time-saving characteristics, high material utilization rate, and high design flexibility. Different from traditional subtractive and formative manufacturing processes, AM technology has the potential to build complicated structures with near-net-shape from the three-dimensional (3D) model in layer-upon-layer forms. According to the raw materials, Metallic additive manufacturing (MAM) technologies are mainly classified into powder-feeding metal additive manufacturing (PMAM) and wire-feeding metal additive manufacturing (WMAM). PMAM provides thin-scale parts with a low laser consumption, high dimension accuracy, high flexibility, and good surface quality. However, the MAM method that uses recycling powder also has some weaknesses, such as oxidation and pore defect formations, low deposition rate, and materials waste. The use of wire materials can improve the deposition rate and material utilization rate significantly compared with the use of powder materials with a lower utilization rate. Thus, WMAM technology has been successfully applied in fabricating large geometries and high near-net-shape ratio metallic components.

WMAM technology can be categorized into three types according to the heat source: wire and arc additive manufacturing (WAAM), electron beam freeform fabrication (EBF^3), and laser additive manufacturing (LAM). Although wire and arc additive manufacturing has the advantages of a high fabrication efficiency, low equipment cost, large component manufacturing capability, and defect-forming prevention compared with other AM technologies, it has challenges, such as control of heat input, low cooling rates, large distortion, and surface fouling. Development of the EBF^3 method has been accelerated because of its ability to manufacture high-quality near-net-shape components with better mechanical properties. This method also has problems, such as a low deposition rate, the requirement for a vacuum environment, and a high equipment price. The LAM method has been applied widely and uses a high-energy density laser that is irradiated on a substrate or previous layer. However, the conventional MAM process that uses cold wire materials remains an ongoing challenge because of the high reflectivity on some materials, the inability to control base metal melting and cold wire melting independently, and small process condition tolerances. Therefore, the LAM method combined with a hot-wire system is interesting because of its high productivity and controllability.

The objective of this thesis was to develop a high-efficiency and high-quality (with no defects) additive manufacturing technology using a combination of a high-power diode laser and hot-wire method with three types of metallic materials: Stainless steel, Ni-based alloy, and 5xxx-series Aluminum alloy. In hot-wire laser additive manufacturing (HLAM), a laser beam with high controllability serves as the main heat source, and another heat source is Joule heat that is generated by a hot-wire current, which heats the filler cold-wire to its melting point independently from the heat input of the main heat source for base metal melting.

Firstly, a simple calculation method to predict the appropriate wire current was proposed and confirmed by hot-wire feeding experiments without laser irradiation. The results of theoretical calculation and experimental value of the appropriate heating current were investigated. In order to clear the experiment verification, this experiment used a high-speed camera to observe the hot-wire heating phenomenon. As a result, the appropriate hot-wire current for heating the wire tip to nearly its melting point for four wires (SUS308L, SUS630, Inconel625, and A5356WY) was obtained. It is found that the hot-wire heating current is an important parameter to achieve stable and smooth wire feeding. Excessively low and high wire currents result in insufficient wire-tip temperature with poking on the base metal surface and fusing and spatter formation, respectively. In the calculation method, the appropriate current value under different conditions (e.g. wire feeding speed, temperature-dependent specific heat, temperature-dependent specific gravity, and temperature-dependent specific electrical resistivity) was studied in detail. As a result, the wire temperature increment in segment length L is positively correlated with the square of the wire current I, and negatively correlated with the wire feed speed V_F and the diameter of filler wire. Moreover, the estimated current is in good agreement with the experimental values over a wide range of wire feeding speeds from 0 to 20 m/min for all four filler materials, considering both heat loss from heat convection and heat generation by contact resistance.

Through this calculation method, the appropriate current of filler material could be obtained under various wire feeding speeds. The final aim of this study is to a combination of the diode laser irradiation and hot wire method. Thus, the hot-wire laser AM by using SUS308L wire was investigated at first. High-speed imaging was performed to monitor clear wire melting phenomena and molten pool formation during AM processing by combining hot-wire feeding and diode laser irradiation. The two-layer and three-layer deposited samples were then proposed and evaluated. As a result, a process windows for a laser power from 3 to 5.5 kW, process speeds from 0.3 to 0.5 m/min, and a wire feeding rate from 20 to 40 were obtained. A large width above 10 mm and a high deposition rate above 800 cm^3/h were achieved. There are many parameters involved in the process conditions, including laser power, process speed, wire feeding rate, and energy heat input, mainly affect the melting phenomenon and bead appearance of three-layer deposition. It is found that the energy heat input was proposed as being key to obtaining adequate and stable melting phenomena. Each wire feeding rate from 20 to 40 had a lower limitation of energy heat input from 35 to 60 J/mm^3 to create sound deposited layers. Moreover, the effects of laser spot size on a bead shape and cross-sectional characteristics were investigated. As a result, a sufficiently high wire feeding speed (rate) should be used according to the laser beam width and processing speed before optimizing other parameters in the proposed HLAM process.

Then, the AM conditions for the three types of wires (SUS308L, Inconel625, and A5356WY) were also investigated using the appropriate wire current calculated using the proposed method. It is found that the laser power and process speed affected the effective width and effective height and maximum height, respectively.

The wire feeding rate had the biggest effect on height and the near net shape rate. The optimized AM process parameters were obtained from the viewpoint of higher material utilization and more stable bead formation according to cross-sectional evaluations. As a results, sound three-layers and cross-sections without any defects were obtained for the three materials types using the optimized process parameters. A wide effective width of 9–11 mm, and a high wire feeding speed of 12–20 m/min (deposition rate of approximately 800–1300 cm^3/h) were achieved. Moreover, three large wall-type parts with the effective width of ~10 mm, effective height above ~40 mm, and length above ~200 mm were fabricated by using optimized process conditions, and tensile tests were performed. Large-wall samples for the three materials types with a maximum height of 42.4-59.3 mm and a high near net shape rate of 75-83% were obtained by using only 15 layers. A sufficient tensile strength and elongation of large-wall of three materials were achieved. However, the thin-wall of various materials also need to apply in special industries.

Finally, a hot-wire with narrow diode laser spot AM technique was investigated for the deposition of 630 stainless steel. The effect of processing conditions including the wire feeding position, defocus length and welding direction on the stability of deposition along with the effect of the energy density distribution and process speed. As a result, the wire feeding position significantly affected the stability of the HLAM process. The wire feeding position that is too close ($D \leq 0$ mm) or too far ($D \geq r$ mm) from laser beam center results in wire dripping or wire stubbing, respectively. When the wire feeding position ($0 < D < r$ mm) was appropriate, the homogeneous width deposited metal without any defects could be obtained. A process map between the energy heat input and wire feeding rate was established for predicting the suitable defocus length. The sound bead with no defects could be fabricated under the suitable energy heat input ranging from ~10 to 21 J/mm^3 when the wire feeding rate is from 6.7 to 10. The substrate can be melted with the limitation of energy heat input was ~10.5 J/mm^3. Compared with hot-wire leading, the laser leading process that pushed a forward flow of the liquid metal and acids the backward flow along the edges of the molten pool. The laser leading condition can significantly avoid the humping defects and improved the shape of the bead. The effect of process speed on the neat net shape rate and microstructure of the deposited three-layer was also investigated. It is found that the microstructure of the materials fabricated at difference process speed was evaluated. The phases of 630 stainless steel deposited three-layer mainly composed of a large number residual δ-ferrite and a small amount of γ-austenite. The deposited metals solidify in F mode, and the morphologies of ferrite are vermicular, skeletal and lathy.

Table of Contents

Chapter 1

Introduction

1.1 Research background

1.1.1 Background of Additive Manufacturing

Additive manufacturing (AM) is a family of new techniques that have developed rapidly in various industries, such as shipbuilding, medical, automobile, military, and aerospace over the past decades due to the time-saving characteristics, high material utilization rate, and high design flexibility [1-3]. Compared with traditional subtractive manufacturing methodologies, AM technology yields continuous material accumulation by layer-by-layer addition and high-accuracy and complex 3D components through computer-controlled technology [4, 5]. In AM technique, the conventional products could be manufactured as long as the CAD data, materials, and equipment are available given. Therefore, AM technology could achieve an integrated and quick response to the demand because the instructions of this technology come directly from the digital model data without the need for complicated manufacturing steps such as the die or casting molds [6-8]. In order to reduce overproduction and transportation fee, it is also possible to produce the only necessary amount of parts in stock when needed, thus this one-step manufacturing enables the manufacturers to create small quantities and near-net-shape products at a low cost. Because of these characteristics, AM technique is of great significance from the perspective of global and next-generation manufacturing technology.

Research, development, and practical application of additive manufacturing (AM) technologies, such as three-dimensional (3D) printing processes, have been carried out actively over recent years [9]. The adoption timeline of AM technique was shown in Fig.1.1. In the early 1925s, wire arc additive manufacturing (WAAM) technology has been firstly proposed by Baker [10], and he used the electric arc as the main thermal source and metallic wire as feedstock to manufacture the product. From the 1980s to the 2000s, with the emergence of stereolithography (SL) technology, electronic computers, and industrial lasers, as well as the research of fused deposition modeling (FDM), selective laser sintering (SLS), selective laser melting (SLM), and direct metal deposition (DMD) which indicated the arrival of early metal laser additive manufacturing (LAM) [11-14]. The main application of AM technique was applied in product design, part production, rapid prototyping, and concept modeling. In the U.S., President Obama launched the "Advances Manufacturing Partnership" in 2011. In the European Union, the "The Economist" magazine believed that AM technology can promote the third industrial revolution.

The “Additive Manufacturing Aiming Towards Zero Waste & Efficient Production of High-Tech Metal Products (AMAZE)” led by the Europe Space Agency (ESA) started in early 2013 with a budget of approximately 2 billion euros. In Japan, the "Ministry of Economy Trade and Industry (METI)” established a study group on new manufacturing in October 2013 and compiled a report in February 2014 [15-19]. This report pointed out that AM technology has played an important role in the innovation of Japanese manufacturing processes and products. Especially in the shipbuilding and aerospace industries, they are very keen to take advantage of the characteristics of different metal additive manufacturing. Figure 1.2 shows the total AM market between 2014 to 2027, and it is estimated that the total annual growth rate of the global AM market is about 20% [20]. Due to the growing demand for metal AM technology, it is necessary to better understand the relationship between material processing methods, mechanical properties, and microstructures in order to produce qualified and reliable products suitable for various industries [21].

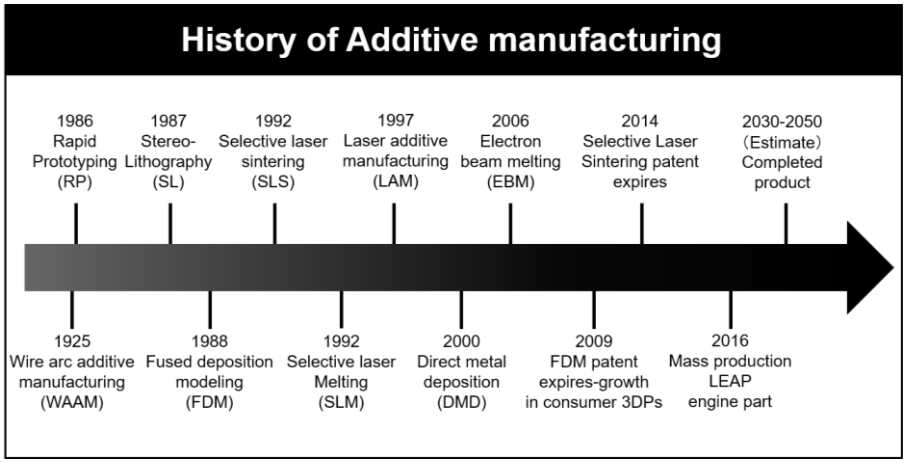

Fig. 1.1. Additive manufacturing adoption timeline [15].

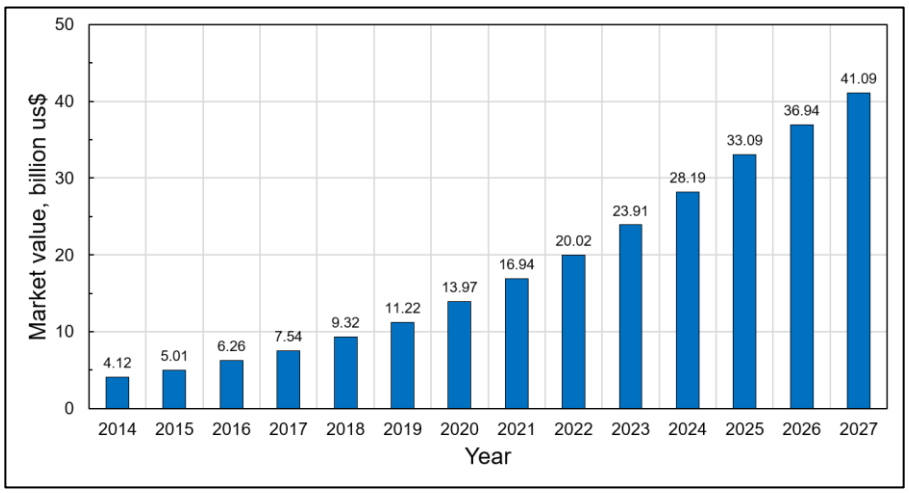

Fig. 1.2. Total Additive manufacturing market value [20].

1.1.2 Current state of metal additive manufacturing technology

Metal-based additive manufacturing (MAM) is to use metallic raw materials as a feedstock on a substrate and then a deposited layer-upon-layer which eventually produced the desired geometry [22-24]. There are many types of technologies in MAM, as shown in Fig.1.3. According to the metallic raw materials, MAM technologies are mainly classified into powder-feeding metal additive manufacturing (PMAM) and wire-feeding metal additive manufacturing (WMAM). In PMAM, four powder material feeding processes are proposed: laser powder bed fusion (L-PBF), laser direct energy deposition (L-DED), electron beam powder bed fusion (EB-PFB), and plasma arc direct energy deposition (PA-DED), which are distinguished by the various thermal energy heat source, such as laser beam, electron beam, and plasma arc [25-27]. In PMAM, these processes can provide thin-scale parts with high dimension accuracy (10-30 μm) and good surface quality [28, 29]. However, the MAM method that uses powder materials also has disadvantages, such as a low deposition rate of 30-100 cm^3/h, high material cost, small tolerances of process conditions, and defect formations [30, 31]. Moreover, the choice for recycled powder also has some weaknesses such as oxidation, moisture, and materials waste. Compared with the PMAM, MAM processes consider wire metal as the raw material that significantly improves material utilization ratio, deposition efficiency, and avoids pollution by using powder [32]. Thus, WMAM technology has been successfully applied in fabricating complicated geometries and high near-net-shape ratio metallic components.

WMAM can be categorized into gas metal arc direct energy deposition (GMA-DED), gas tungsten arc direct energy deposition (GTA-DED), plasma arc direct energy deposition (PA-DED), electron beam direct energy deposition (PA-DED), and laser direct energy deposition (L-DED) [33, 34]. The WMAM that uses the arc heat source was collectively referred to as wire arc additive manufacturing (WAAM). As for WAAM, the deposition rate can achieved 350-800 cm^3/h due to the higher energy arc source. WAAM has advantages such as large and middle part fabrication, high deposition rate, and high fabrication efficiency. However, it has the limitations of excessive heat input, high distortion, and surface uncleanness [35, 36]. In EB-DED, the prototype with a different size was built under the deposition rate between 300-400 cm^3/h. With the rapid development of the EB-DED method, high-quality near-net-shape components were proposed with high efficiency and low material waste by an electron beam for the heat source in a vacuum chamber. This method has made it challenging due to the evacuation vacuum environment and the high price of the equipment [37, 38]. Because the deposition process of EB-DED needs to be under a precision welding environment, the equipment fees of EB-DED are higher than WAAM and L-DED. L-DED method is deposited by a high-energy laser which irradiated on the substrate or the previous layer has been widely applied, especially the metallic wire used as the additive material. However, the L-DED process using wire materials remains an ongoing challenge due to relatively low deposition rate of 200-400 cm^3/h, and small tolerances of process conditions [39, 40]. As opposed to

the laser cold-wire method, the advantage of the laser hot-wire method can effectively increase productivity, and the degree of freedom of control of the material is high. For the above-mentioned various reasons, the high power diode laser with hot-wire feeding system would be targeted as an interesting method because of its impressive high productivity (400-1000 cm^3/h) and high material use rate (80%-100%) [41, 42].

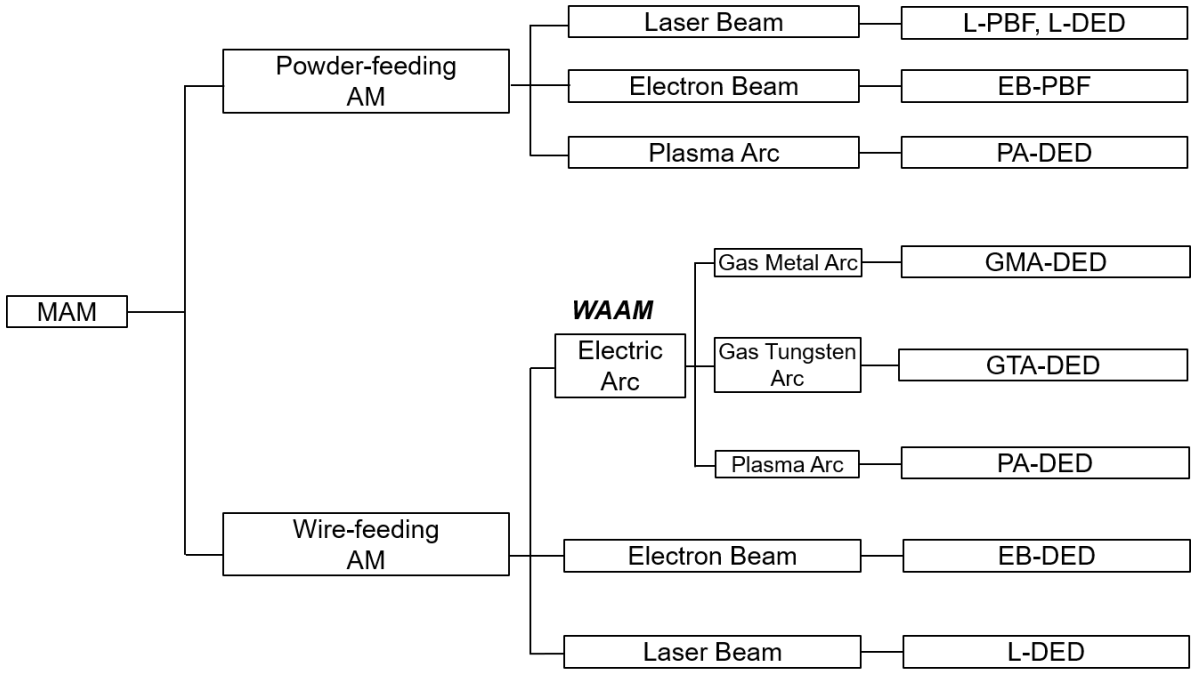

Fig. 1.3. Categorization of MAM technology [43].

1.1.3 Metal feedstocks of laser additive manufacturing

Strong demands in the automotive, shipbuilding, and aerospace fields have led many researchers to focus on additive manufactured metallic materials, such as stainless steel, nickel-based alloys, and aluminum alloys [43-45]. Therefore, there is an urgent need to develop a AM technology for fabricating various materials at a low cost.

Compared with other AM technology, laser additive manufacturing (LAM) technology gained more attention in various metal materials manufacturing due to its high accuracy, high flexibility, and complex structure merits [46, 47]. As for LAM technology, this method uses a high-power-density laser beam as the heat source, which has been manufacturing customized and high-quality components [48]. In order to improve material utilization efficiency, it is significant to study the laser reflectivity rate of the metallic materials. Figure 1.4 shows the laser reflectivity rate

for various metal materials under the temperature of 294 K. It can be concluded that the laser reflectivity rate of various filler metal materials is related to the wavelength of the laser radiation. Compared with 1.06 μm, the laser radiation wavelength of 0.81 μm has a lower reflectivity. The reflected laser of metal, especially pure copper (90%) and aluminum alloys (85%), resulted in damage to the laser instrument. In addition, some problems like cracks or incomplete penetration occur, difficulty in control of heat input, and limitations for wider applications [49,50]. When the wavelength of 0.532, named green laser, the reflectivity of pure copper decrease to 46%. The traditional LAM with the aid of the green laser made it possible to apply in the pure copper industry.

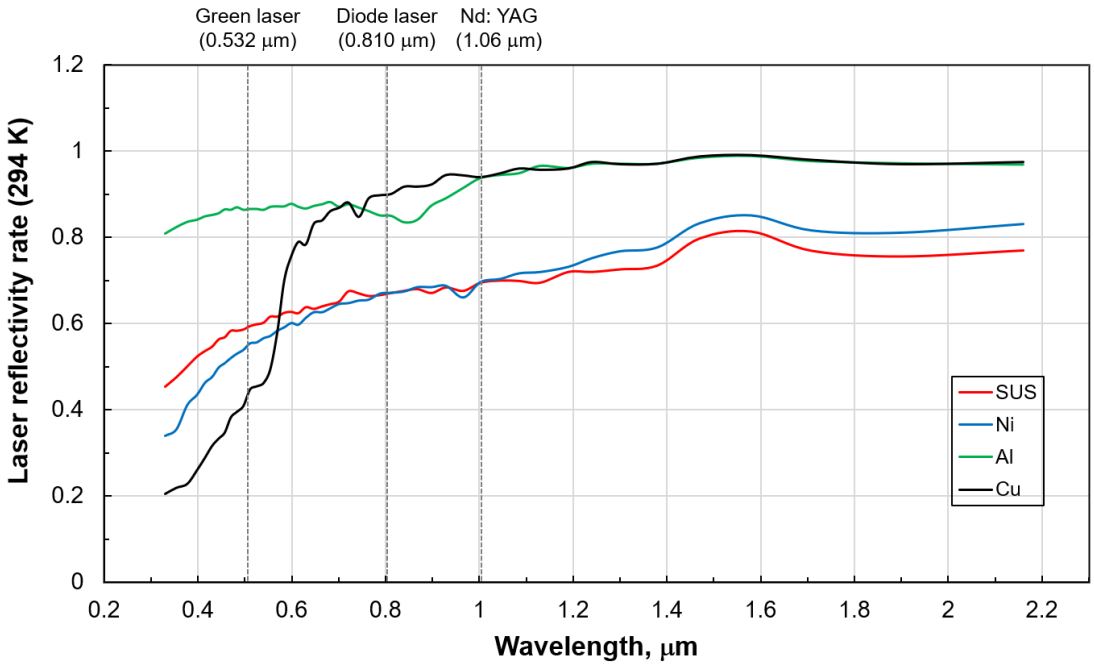

Fig. 1.4 Laser reflectivity rate for various metal materials [50].

1.2 Development of combination diode laser and hot-wire system additive manufacturing technology

Hot-wire laser additive manufacturing (HLAM) technology is a promising and potential manufacturing method because of its high deposition efficiency at a low laser power that results from its dual heat sources, as shown in Fig.1.5. A laser beam with a high controllability serves as the main heat source, and another heat source is Joule heat that is generated by a wire current, which heats the filler wire to its melting point independently from the heat input of the main heat source for base metal melting.

On the one hand, the characteristic of the diode laser is that the energy distribution of the laser spot is hat-shaped, so the energy density in the laser irradiation area is uniform. A diode laser has advantages over CO_2, disk, and fiber lasers, such as high oscillation efficiency, large and flexible beam creation, and a highly controllable energy distribution in the beam spot [51-53]. By using an optical element to arbitrarily change the spot shape, it is possible to fabricate the product according to its thickness. In addition, the use of the large beam shape and uniform energy distribution of the optical system can form a low-dilution flat covering layer over a wide range. In spite of the extremely large amount of deposition, the heat input of this method is lower than that of arc welding, so it is expected that there will be fewer problems such as temperature control of the formed product during layering, bead dripping and reduced spatter and fume.

On the other hand, the hot-wire method can significantly improve the deposition efficiency and save laser energy [54]. In HLAM, the preheated filler hot wire could be melted easier with laser irradiation and heat conduction from the molten pool. This method has become possible to achieve various materials even if it has a high reflectivity rate. It is expected that even materials with low laser absorption can be melted with hot wire which is heated to its melting point. The energy heat input for melting the base metal and preheating the filling filament can be independently controlled, resulting in low heat input and high deposition efficiency [55, 56]. The advantages of the HLAM method compared with the cold-wire LAM method are a higher productivity without an increase in heat input, a high freedom in material choice, and a high material utilization. Therefore, the HLAM method combined with a hot-wire system is interesting because of its high productivity and controllability.

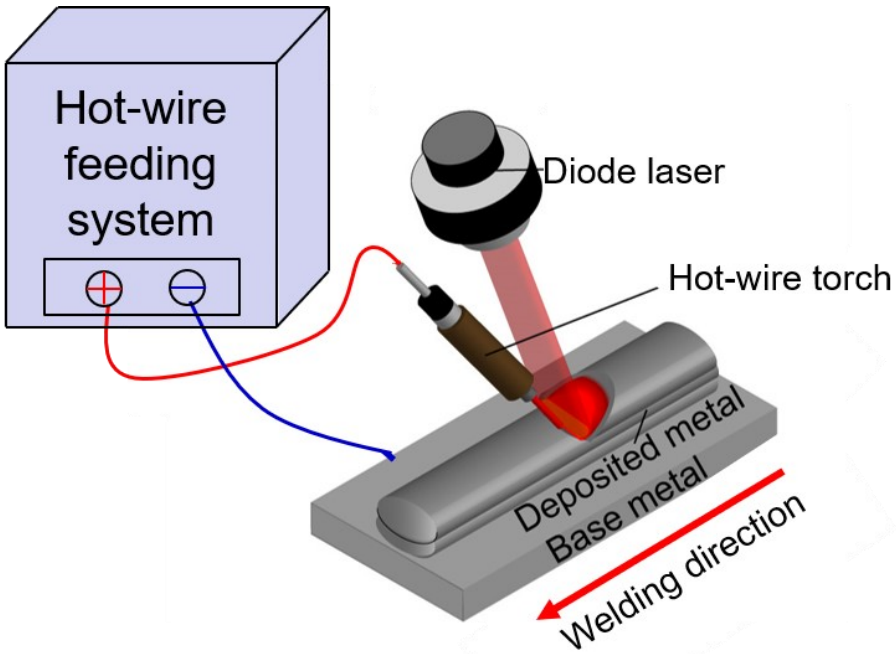

Fig. 1.5. Schematic illustration of hot-wire laser deposition method.

1.3 Objective and Construction of the thesis

The objective of this paper was to develop a high-efficiency and high-quality (with no defects) additive manufacturing technology using a combination of a high-power diode laser and hot-wire method with three types of metallic materials: Stainless steel, Ni-based alloy, and 5xxx-series Aluminum alloy.

Firstly, A simple calculation method to predict the appropriate wire current is proposed and confirmed by hot-wire feeding experiments without laser irradiation. The results of theoretical calculation and experimental value of the appropriate heating current were studied in detail. In order to clear the experiment verification, this experiment used a high-speed camera to observe the melting phenomenon. The appropriate hot-wire current for heating the wire tip to nearly its melting point for four wire materials (SUS308L, SUS630, Inconel625, and A5356WY) was obtained. Hot-wire feeding experiments without laser irradiation were performed to experimentally obtain the appropriate wire current and confirm the calculated values.

Secondly, The hot-wire laser AM by using SUS308L wire was investigated. High-speed imaging was performed to monitor clear wire melting phenomena and molten pool formation during AM processing by combining hot-wire feeding and diode laser irradiation. The two-layer deposited samples were then proposed and evaluated. The effect of wire feeding rate (wire feeding speed / process speed) on first and second-layer evaluated parameters (e.g. bead width and bead height) were investigated. A window of three-layer deposition for a combination of process parameters has been developed. The effect of energy heat input on melting phenomenon and bead appearance of three-layer deposition was investigated.

Then, the AM conditions for the three wire materials (SUS308L, Inconel625, and A5356WY) were also investigated using the appropriate wire current calculated using the proposed method. The effect of process parameters, such as laser power, process speed, and the wire feeding rate on bead characteristics was investigated by cross-sectional evaluations on three-layer depositions. The optimized AM process parameters were obtained from the viewpoint of higher material utilization and more stable bead formation according to cross-sectional evaluations. Three 50-mm-height, 8-mm-width, and over 200-mm-length samples were fabricated by using optimized process conditions, and tensile tests were performed by using the large sample.

Finally, a hot-wire with narrow diode laser spot AM technique was investigated for the deposition of 630 stainless steel. The effect of processing conditions including the wire feeding position, defocus length and welding direction on the stability of deposition along with the effect of the energy density distribution and process speed on the neat net shape rate of the deposited three-layer was investigated. Moreover, the microstructure of the materials fabricated at difference process speed was evaluated.

Chapter 1 introduces the background and objective of this research, illustrates the overall construction of the thesis.

Chapter 2 reviews the previous and present situation of the researches on AM technology.

In Chapter 3, the appropriate hot-wire current for heating the wire tip to nearly its melting point for four types of wires (SUS308L, SUS630, Inconel625, and A5356WY) was investigated.

In Chapter 4, a high-efficiency hot-wire laser AM technology for SUS308L wire was developed. The two-layer deposited samples were then proposed and evaluated. A window of three-layer deposition for a combination of process parameters has been developed.

In Chapter 5, the optimized AM conditions for the three types of wires (SUS308L, Inconel625, and A5356WY) were also investigated using the appropriate wire current calculated using the proposed method. The effect of process parameters on three-layer depositions was investigated by cross-sectional evaluations. Three large-wall parts and tensile tests were performed by using the large-wall sample.

In Chapter 6, a hot-wire with narrow diode laser spot AM technique was investigated for the deposition of 630 stainless steel. The effect of processing conditions including the wire feeding position, defocus length and welding direction on the stability of deposition. The microstructure of the materials fabricated at different process speed was evaluated.

In Chapter 7, summaries this thesis and proposes the future work.

Chapter 1: Introduction and research objectives

⇩

Chapter 2: Literature review

⇩

Chapter 3: A study of the appropriate current calculation methods for various wires using hot-wire method

- Investigation of hot-wire heating phenomena and appropriate hot-wire current
- Simple calculation method for estimating appropriate hot-wire current
- Effect of contact resistance and heat loss coefficient on estimated results

⇩

Chapter 4: Development of the AM technology by using hot-wire system and high-power diode laser

- Investigation of molten pool and bead formation of two-layer deposition by using hot-wire laser method
- The effect of energy heat input on three-layer deposition phenomena
- The effect of laser spot size on bead and cross-sections

⇩

Chapter 5: Investigation of phenomena and optimization parameters of various materials for the large-wall formation

- The effect of process parameters on cross-sectional characteristics
- Optimization parameter of three types of wires (SUS308L, Inconel625, and A5356WY) for the large-wall formation
- 15-layer Large-wall modelling fabricating and tensile test

⇩

Chapter 6: Optimization of process conditions in application of narrow beam by using SUS630 wire

- Investigation of the wire feeding position on wire melting phenomena
- Optimization of match between the energy density distribution and process speed on deposition
- Effect of process speed on bead shape and microstructure

⇩

Chapter 7: Summary and future work

Fig. 1.6 Construction of the thesis.

Chapter 2

Literature Review

2.1 Introduction

This chapter reviews the theoretical backgrounds and relative research on metal additive manufacturing (MAM) technology. Firstly, the present research trends of powder-feeding MAM techniques, such as selective laser melting (SLM), selective laser sintering (SLS), and powder directed energy deposition (P-DED) are discussed in detail. The applications and problems of powder-feeding MAM are introduced. Then, the wire-feeding MAM technologies with three types of thermal sources (e.g. arc, electron beam, laser beam) are studied. The MAM technologies of various metallic materials (e.g. Stainless steel, Ni-based alloys, Aluminum alloy) are summarized. Finally, the history and progress of a novel technology, which is combined with a hot-wire system and a high-power diode laser system, was discussed in detail.

2.2 Research and development status of MAM technology

2.2.1 Powder-feeding MAM

Powder-feeding MAM has been developed in order to produce high precision and complex 3D part. Many literatures proposed that MAM using metal powder as the raw material has the advantage of a high accuracy appearance and a low surface roughness [57, 58]. Table 2.1 shows the literature summary regarding powder-feeding MAM technologies, such as SLM, SLS, and P-DED. It is clearly found that compared with DED, the SLM and SLS method can be used to fabricate higher dimensional accuracy parts at high flexibility in the same workstation [59].

Mumtaz et al [60]. used Inconel 625 powder to produce thin-walled parts with a layer thickness of 10~50 μm and a precision of ± 0.04 mm by using SLM process. He found that the minimum side surface and top surface roughness is 9~10 μm. Zhu et al [61]. successfully fabricated walled parts with a deposition rate of 0.006 kg/h, dimensional accuracy of ± 0.05 mm, and surface roughness of 14~16 μm by using the SLS method. Compared with PBF, P-DED can significantly improve the layer thickness of 200~500 μm and deposition rate [61-63].

Table 2.1 Literature summary regarding metal powder feeding AM technologies

Process	Layer Thickness (μm)	Deposition rate (cm^3/h)	Dimensional accuracy (mm)	Surface roughness (μm)	Reference
SLM	10~50	~20	± 0.04	9~10	Mumtaz (2009)[60]
SLS	75	~30	± 0.05	14~16	Zhu. (2003) [61]
P-DED	200~500	60~360	0.5~1.0	4~10	Keist (2016) [62]; Shah(2010) [63]

2.2.2.1 Powder bed fusion

PBF is that spread metal powder on the bed and uses the high-energy laser as a heat source to selectively melt, solidify or sinter the parts to be formed, as shown in Fig. 2.1. It is significant for PBF is to control the transformation between solid phase and liquid phases of deposited powder in each layer. PBF provides high flexibility parts with a low laser power (<500 W) and high precision [64, 65]. However, PBF has several major disadvantages. Firstly, PBF is the most expensive MAM technology due to its expensive powder materials, slow deposition efficiency, and high equipment costs. Then, PBF has serious environmental pollution and other problems. In order to avoid the degradation of mechanical properties caused by the oxidation of the powder in the air, the process is carried out in a vacuum or a closed chamber with inert gas [66]. Moreover, PBF has a greatly restricted in manufacturing large parts due to its large amount of powder materials which need to manage and store [67]. Finally, the powder material undergoes rapid heating and cooling during melting. The application of local concentrated energy resulted in localized residual stress, nonhomogeneous and anisotropic microstructure, as well as voids and pores that occurred in the microstructure. These factors induced crack initiation and degrades the mechanical properties of the deposited metal [68].

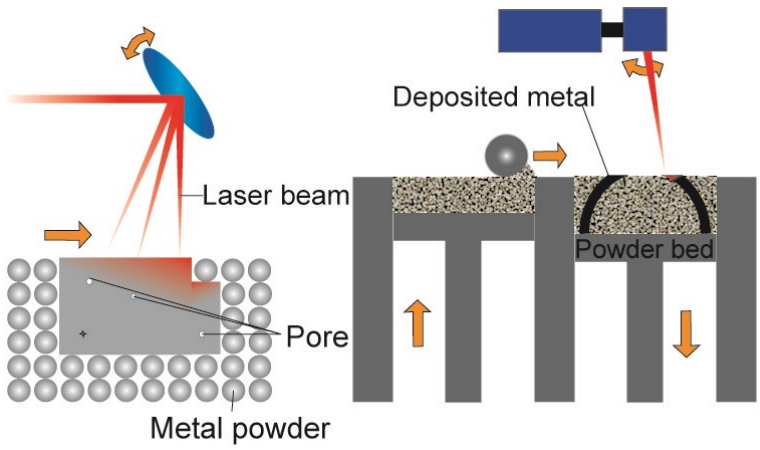

Fig. 2.1. Schematic illustration of PBF [66, 69].

2.2.2.2 Powder directed energy deposition

The powder materials in P-DED are supplied from the powder feeder, and it is carried by the internal gas through the nozzle to the melting area, as shown in Fig. 2.2. Different from the PBF method with the respreading powder, the characteristic of P-DED is that the powder flow through the nozzle, and the laser beam is simultaneously transported on the substrate [70]. During the deposition process, a protective gas (normally argon) flow, which is applied to the molten pool area, to ensure a good melting environment [71]. Compared with PBF, it is significantly better in terms of deposition rate and layer thickness of each layer. However, there are some limitations, such as required support structures and the challenge to deposit sharp corners [72].

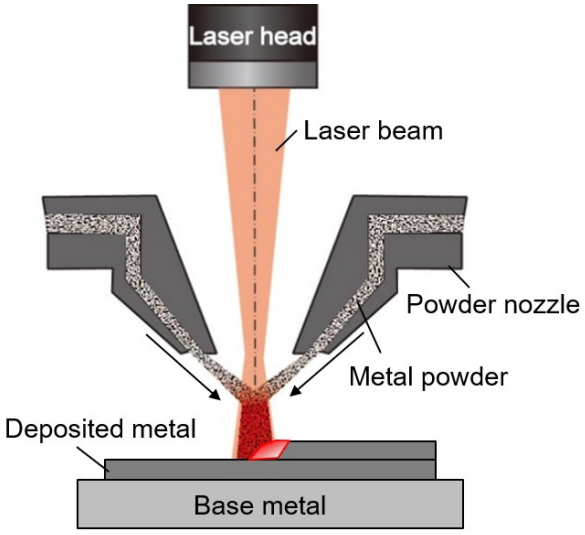

Fig. 2.2. Schematic illustration of P-DED [69, 70].

2.2.2 Wire-feeding MAM

Wire-feeding MAM technology is used to manufacture large expensive components and complex functional metal objects. In comparison with powder materials, the use of metal wires in MAM can significantly improve the material utilization rate, production efficiency, and costs [73]. Moreover, wire-feeding AM does not expose workers to the dangerous powder environment. Metal wire is thus used instead of metal powder as a feedstock material in MAM to produce large structure components with a high deposition efficiency [74].

Ding et al. [32] summarized the current research and development status of wire-feed AM technology, and pointed out that the future challenges, such as high residual stresses and distortion, caused by excessive heat input. The deposition rate of the wire-feeding AM technology is extremely high, which promotes its application

in building median and large-sized parts [75]. Table 2.2 shows the literature summary regarding wire-feeding MAM technologies. State-of-the-art studies have shown that metal-based AM technology can be categorized into three types according to the heat source: wire and arc additive manufacturing (WAAM), electron beam freeform fabrication (EBF^3), and laser additive manufacturing (LAM).

Table 2.2 Literature summary regarding wire-feeding MAM technologies

Process	Layer Thickness (μm)	Deposition rate (cm^3/h)	Dimensional accuracy (mm)	Surface roughness (μm)	Reference
EBF^3	N/A	360~720	1.0~1.5	8~15	Wu et al. (2019) [81]; Taminger et al. (2006) [82]
WAAM	1000~2000	720~1200	±0.2	200	Xiong et al. (2017) [84]; Colegrove et al. (2013) [88]
LAM	＞1000	120~1000	±0.03	8~16	Baufeld et al. (2011) [35]; Ding et al. (2015) [32]

2.2.2.1 Electron beam freeform fabrication

The EBF^3 technique, developing from rapid prototyping processes, employs electron beam as the heat source for manufacturing high-performance metallic component, as shown in Fig. 2.3. In the EBF^3 process, the metal wire is sent to the molten pool, which is created using an electron beam in a vacuum chamber. Among the wire-feeding AM technologies, the EBF^3 process has many advantages such as high deposition rates, high energy efficiency, high materials freedom, and good protection for molten pools due to the vacuum environment [76, 77].

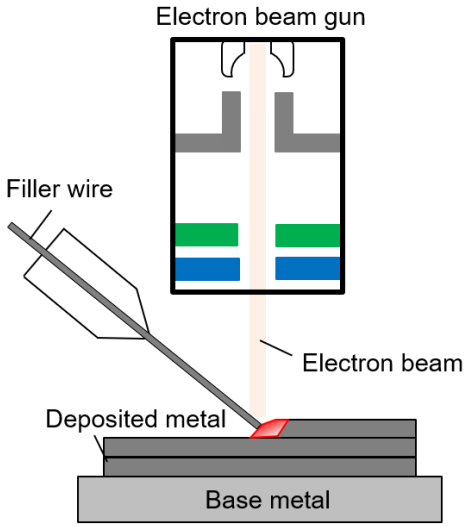

Fig. 2.3. Schematic illustration of EBF^3 [69, 76].

Xu et al. [78] prepared a Ti-6Al-4V block part by EBF^3 process and studied the microstructure and mechanical properties of the deposited samples. However, the disadvantage of EBF^3 is that this process takes a lot of time to evacuate the vacuum container, and the size of the manufacturing components is also limited by space [79-82]. Moreover, Cordero et al. [80] proposed that high energy and small focusing radius of electron beam cause a complex thermal behavior, such as rapid solidification at a large temperature gradient during EBF^3.

2.2.2.2 Wire arc additive manufacturing (WAAM)

WAAM method makes use of an electrical arc as a source of fusion to melt the metal wires for the production of medium and large complexity parts, as shown in Fig. 2.4. Williams et al. [83] proposed that a variety of components, such as Ti-6Al-4V spars, landing gear assemblies, aluminium wing ribs, steel wind tunnel models and cones have been successfully fabricated by using WAAM. Xiong et al. [84] also produced a large structural parts (~3000 mm) under a high fabricating efficiency. However, WAAM method also has some drawbacks, such as high dilution, overheating, coarse grains, and surface uncleanness [85, 86]. However, uneven heat distribution cause serious accumulation in certain areas, resulting in residual stress and deformation. Factors such as arc ignition and arc extinguishing process lead to relatively poor accuracy and surface finish of molded parts [87]. Colegrove et al. [88] also proposed that excessive heat input leads to a longer high temperature residence time, a wider welding heat-affected zone, and severe overheating, which caused the formation of coarser grain microstructure resulting in the decreases of the plasticity and toughness.

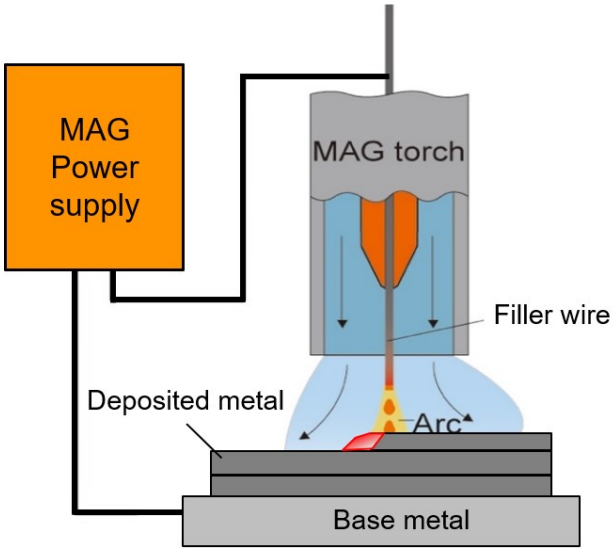

Fig. 2.4. Schematic illustration of WAAM method [69, 87].

2.2.2.3 Laser additive manufacturing (LAM)

The LAM method has been applied widely and uses a high-energy density laser that is irradiated on a substrate or previous layer using metallic wire as common additive materials [89]. As schematically shown in Fig. 2.5, this process normally consists of a laser, a robot system, accessorial mechanisms, and a wire-feeding system. The LAM that used wire materials can improve the deposition rate significantly compared with the use of powder materials with a lower utilization rate (20%) [90, 91]. In LAM, the wire feeding position, wire orientation, wire feeding angle, deposition direction and detailed parameters for different materials have been investigated by many researchers to obtain defect-free beads and achieve good process stability for multi-layer deposition [92]. However, the conventional LAM process that uses cold wire materials remains an ongoing challenge because of the high reflectivity on some materials, the inability to control base metal melting and cold wire melting independently, and small process condition tolerances [93].

Huang et al. [94] built multi-layered samples using an A5087 Al alloy wire by LAM, and found that the non-optimized process parameters led to pores and unstable layers. The LAM method using cold wire as a filler material also has significant drawbacks. The higher reflectivity of cold wire, especially aluminum alloy, reduce the energy absorption and deposition rate. It is also difficult to precisely control the heat inputs to melt the cold wire and substrate independently, which limits wider applications [95]. Therefore, the LAM method combined with a hot-wire system is interesting because of its high productivity and controllability.

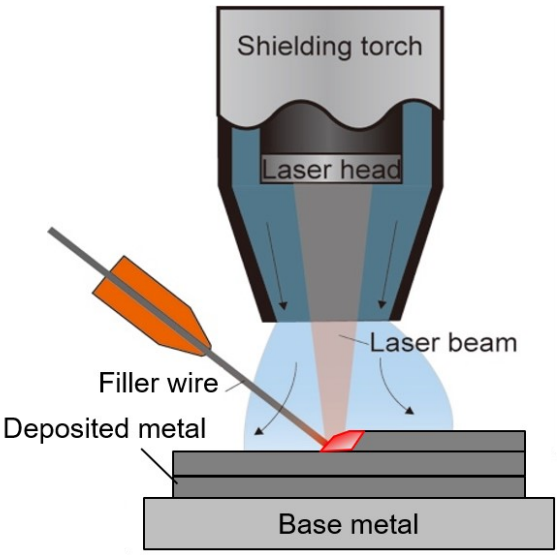

Fig. 2.5 Schematic illustration of LAM [69, 89].

2.3 Additive manufacturing technology for various metal materials

Strong demands in the automotive, shipbuilding, and aerospace fields have led many researchers to focus on additive manufactured metallic materials, such as Fe-based, Al-based, Ti-based, Co-based and Ni-based [96, 97]. It is necessary to critically analyze the metal materials and their recent research on AM techniques, which use a variety of metal materials for a wide range of applications. The metal materials under main kinds such as stainless steel, nickel-based alloys, and aluminum alloy are completely presented in the following sections.

2.3.1 Stainless steel

Presently, many industries applications have dealt with the AM technology by using the stainless steels because of its lower level of carbon, high corrosion resistance, and high mechanical properties [98]. The stainless steel can be categorized into many types according to the microstructure: austenitic, martensitic, ferritic, and austenoferritic duplex stainless steel [99]. The phase characteristic and microstructure of stainless steel is dictated by the chemical composition, such as chromium, nickel, carbon, carbon, etc., and cooling rate [100]. Thus, the industries application of stainless steel can be decided by the characteristics, such as corrosion resistance, ductility, and stability of phases in stainless steel alloy.

Xu et al. [101] investigated the effect of welding parameters on deposited metal and produced a 50 layer sample of 316L stainless steel with 60 mm height by using laser metal deposition. He found that the quality and thickness of each layer are related to the volume of deposited material per unit time and the heat input. Moreover, the solidification rate is influenced by the heat input and wire feed rate. Ocylok et al. [102] investigated the effect of the main process parameters (laser power, velocity and, wire feed rate) on the properties of deposited stainless steel 316L samples by using laser metal deposition AM technology. He found that the wire feed rate has nearly linear with the height of the layer and the heat input into the base material decreases at a higher wire feed rate at fixed laser power. Hu et. al [103] used 17-4 PH stainless steel powder to fabricate 3D parts via PBF. LeBrun et. al. [104] studied the mechanical performance at various thermal processing of tensile specimens machined from bulk 17-4 PH produced by using PBF. Le et al. [105] successfully fabricated thin-walled 308L stainless steel parts by using the WAAM and investigated the effect of processing parameters on the geometry of deposited bead and mechanical properties. They found that the microstructure of wall mainly typically composed of the columnar austenite dendrites and residual ferrite with three types morphologies, which are vermicular morphologies, and lathy. Li et al. [106] also built a 50 mm cubic-walled 308L stainless steel by using the laminar plasma additive manufacturing process, and he point out that the wall has mainly consisted of columnar and equiaxed dendrites, and the columnar dendrites gradually

transformed to equiaxed dendrites from middle region to top region. Wen et al. [107] investigated the influence of linear heat input on microstructure and corrosion behavior of austenitic stainless steel by using WAAM. He found that the primary dendrites spacing of the deposited metal increases with increases of linear heat input. In other words, the cooling rate of steel is related to the growth of primary dendrites spacing and the corrosion resistance. In the WAAM, the cooling time for the structure to transform from δ-ferrite to austenite is related to the amount of linear heat input. Larger heat input caused complex alloy elements to undergo complicated solidification processes and repeated heating processes. These processes aggravated the segregation of elements and further affect the microstructure and corrosion of stainless steel. However, these kinds of it has the limitations of excessive heat input and surface uncleanness [108, 109].

2.3.2 Nickel-based alloys

Nickel-based alloys is widely applied in marine engineering for many years because of its excellent corrosion resistance, high yield strength, and high temperature operating temperatures [110, 111]. Nickel-based alloys are mainly austenitic precipitation hardened superalloys, such as Inconel 625, Inconel 718 alloy, which composed by a amount of Ni and Cr elements. Thus, the high weldability of Nickel-based alloys is very suitable to applied in AM process [112-114]. Baufeld [115] built an Inconel 718 sample by using shaped metal deposition and compared the mechanical properties of Inconel 718 samples with as-cast material, EBF^3, and LAM process. He found that the tensile strength of sample by shaped metal deposition is slightly higher than that of as-cast materials but lower than samples built by laser and electron beam AM process due to the lower cooling rate of the wire-based tungsten inert gas welding.

Wang et al. [116] explored the effect of location on microstructure and mechanical properties of Inconel 625 samples manufactured by using gas tungsten arc welding. The microstructure analysis showed that the cellular grains without secondary dendrites in the near-substrate region. With increasing layer, the grain morphology changed to columnar dendrites structure, and transformed to the equiaxed grain in the top region. Because of the temperature gradients and cooling rates in different regions, heterogeneous microstructures are formed in the top region, with larger dendritic arm spacing and more laves phases resulting in the higher tensile strength and hardness. Some alloying elements (e.g. Nb and Cr) undergo solid solution strengthening to increase the strength of the alloy, but the disadvantage is that these alloying elements increase the solid-liquid two-phase temperature range of the solid solution (about 75 ℃). This intensifies the enrichment of some elements (e.g. Nb and Mo) during the solidification process and leads to the formation of non-beneficial phases, which seriously affects the properties of the alloy [117, 118]. Thus, Inconel 625 alloy produced by WAAM process has a high heat input and a complex heat transfer, and it is easily leads to a decline in product quality

and performance [119, 120]. Amato et al. [121] compared the microstructures and properties of Inconel 625 fabricated by electron beam melting and selective laser melting. He found that the microstructure of both processes exhibited columnar architectures by γ''bct Ni3Nb, but each contains a complex array of different precipitates due to different cooling rates. The columnar plates of γ'' (Ni3Nb) precipitates appeared in the EBM sample, and the microstructures of SLM are columnar arrays of fine γ' nanoparticles.

2.3.3 Aluminum alloy

In order to save energy and reduce pollution, countries all over the world are accelerating the process of lighting transportation tools. The manufacturing technology of lightweight materials represented by aluminum alloy has gradually replaced steel materials and has become the main development direction for lightweight manufacturing of vehicles and ships [122, 123]. The structural integration and low-cost manufacturing requirements make the development of aluminum alloy AM an inevitable trend. Aluminum alloys have been widely used in aerospace, rail transit, automobile manufacturing, medical equipment due to its high specific strength, low density, high electrical, thermal conductivity, and good corrosion resistance [124, 125].

At present, prevalent Aluminum alloys such as 7xxx series [126], 6xxx series [127], 5xxx series [128, 129], 4xxx series [130], and 2xxx series [131, 132] have been successfully manufactured by AM process. Many researchers used the Al alloy to manufacture parts by using the WAAM process. Hauser et al. [130] investigated the porosity in WAAM of 4043 series Al alloys. He found that with the shielding gas flow ratio increases, the porosity in Al samples increases due to the high solidification rate of the molten pool by forced convection. Then, because of the high thermal conductivity and low thermal efficiency of aluminum alloy, the temperature spreads rapidly along the substrate or component. The rapid solidification rate caused the limitation of arc energy of molten pool and filler wire resulting in a low deposition rate of aluminum alloy by using the WAAM process. The excessive heat input in WAAM reduces the shape accuracy of the deposited structure, declines the stability of the deposition process, and leads to a sharp drop in mechanical properties [125, 128]. In order to reduce the porosity in arc welding, Fu et al. [132] proposed a novel method of hot-wire arc AM technology to fabricate 2024 aluminum alloy. He found that with increases of the hot-wire current, the porosity firstly decreases, and afterward increases progressively. The mechanical properties are significantly increased with the decrease of porosity by using hot-wire arc AM technology. Aboulkhair et al. [103] summarized AM process of Al-alloy using selective laser melting. He pointed out that SLM is also a challenging process to produce Al alloy due to the difficulties associated with laser-melting Al powder where parts suffer various defects. On the other hand, it is now possible to manufacture almost defect-free Al-Si alloy parts using SLM due to the presence of the Si hard phase, which poses limitations on their machinability. Huang et al. [129] successfully produced 5A06 Al alloy multi-layered samples by using laser wire-feed metal AM

technology. He found that with optimized process parameters (e.g. Wire feed angle, traverse speed, laser power, and overlap ratio), the multi-layered samples are characterized by a trace amount of porosity and are crack-free. The non-optimized process parameters led to pores and unstable layers. The LAM method using cold wire as a filler material also has significant drawbacks. The higher reflectivity of cold wire, especially aluminum alloy, reduce the energy absorption and deposition rate. It is also difficult to precisely control the heat inputs to melt the cold wire and substrate independently, which limits wider applications. Therefore, the LAM method combined with a hot-wire system is interesting because of its high productivity and controllability.

2.4 The development of hot-wire welding method

The hot-wire method has a high degree of freedom in selecting wire materials because the wire is heated to just below its melting point by only Joule heating [134]. In 2003, Hori et al. [135, 136] proposed a novel method of hot-wire Tig welding method, which uses pulsed current to heat filler wire, as shown in Fig.2.6. He found that hot-wire Tig is an effective and possible method to reduce the influence of magnetic arc blow by keeping a sufficient non-pulse period of the wire current during welding.

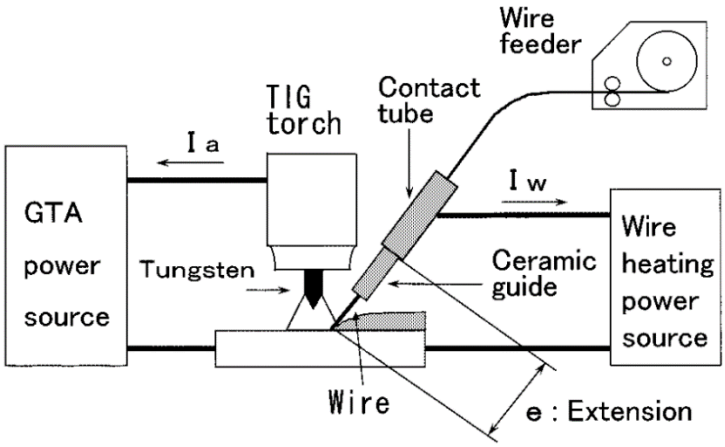

Fig. 2.6. Schematic illustration of hot-wire TIG welding [135].

A suitable process condition is very important for guaranteeing stable melting and avoiding defects during hot-wire feeding. Shinozaki et al. [134] investigated the bead appearance and melting phenomenon during the ultra-high-speed GTA welding method using pulse-heated hot-wire, as shown in Fig.2.7. He found that the bead surface with typical defects was caused by both of excessive high and excessive low current. Moreover, the welding phenomenon with filler wire excessively soften and spatters occurs because of too high wire temperature, and with filler wire bumped into the molten pool bottom because of too low wire temperature. In other words,

wire tip melting was affected mainly by the wire current, the feeding position, and the feeding angle. These process conditions need to be controlled within suitable ranges. The filler wire temperature is the main parameter that is required to maintain wire melting phenomena.

In the layer-upon-layer process, an unsuitable wire temperature results in spatter generation and a non-uniform deposited layer with defects. Shinozaki et al. [137] also investigated the temperature distribution of three kinds of filler wires (e.g., stainless steel, mild steel, and Ti) during ultra-high-speed GTA using a pulse-heated hot-wire, as shown in Fig.2.8. He found that the hot-wire current can be estimated under various welding conditions (e.g., filler wire diameter, wire material properties, wire feeding speed). A suitable hot-wire current is the dominant parameter for stable molten pool creation and hot-wire melting. Liu et al. [138] pointed out that the hot-wire temperature is related to the weld bead characteristics. Wen et al. [139] proposed that a laser process with a preheating of the filler wire to an appropriate temperature could improve the welding efficiency and deposition rate significantly and reduce the heat input.

The novel hot-wire process with a high-power diode laser has been investigated and developed. Yamamoto et al. [140] proposed the laser hot-wire welding method for the lap joint of 980 MPa class high-strength steel sheets (thickness: 1 mm) with wide gap, as shown in Fig. 2.9a. He found that the laser hot-wire method makes the penetrate hole and the molten pool by laser beam irradiation, and the hot-wire heated up through energization fills the penetrated hole of the lap joint. Kadoi et al. [142] investigated the effect of wire conditions and welding conditions on welding phenomenon and bead formation using hot-wire laser fillet joint welding method, as shown in Fig. 2.9b. Todo et al. [143] found that the laser hot-wire welding with the optimized parameters (laser power, defocus length, and wire feeding position) can achieve stable wire feeding, molten pool creation and well-formed weld bead, as shown in Fig. 2.10.

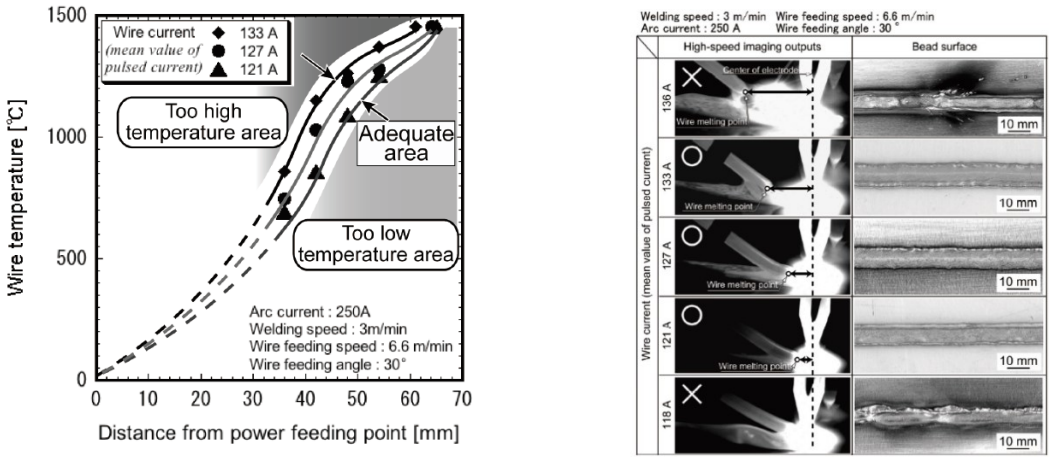

Fig. 2.7. The effect of wire current on temperature distributions, wire feeding phenomenon, and bead appearance [137].

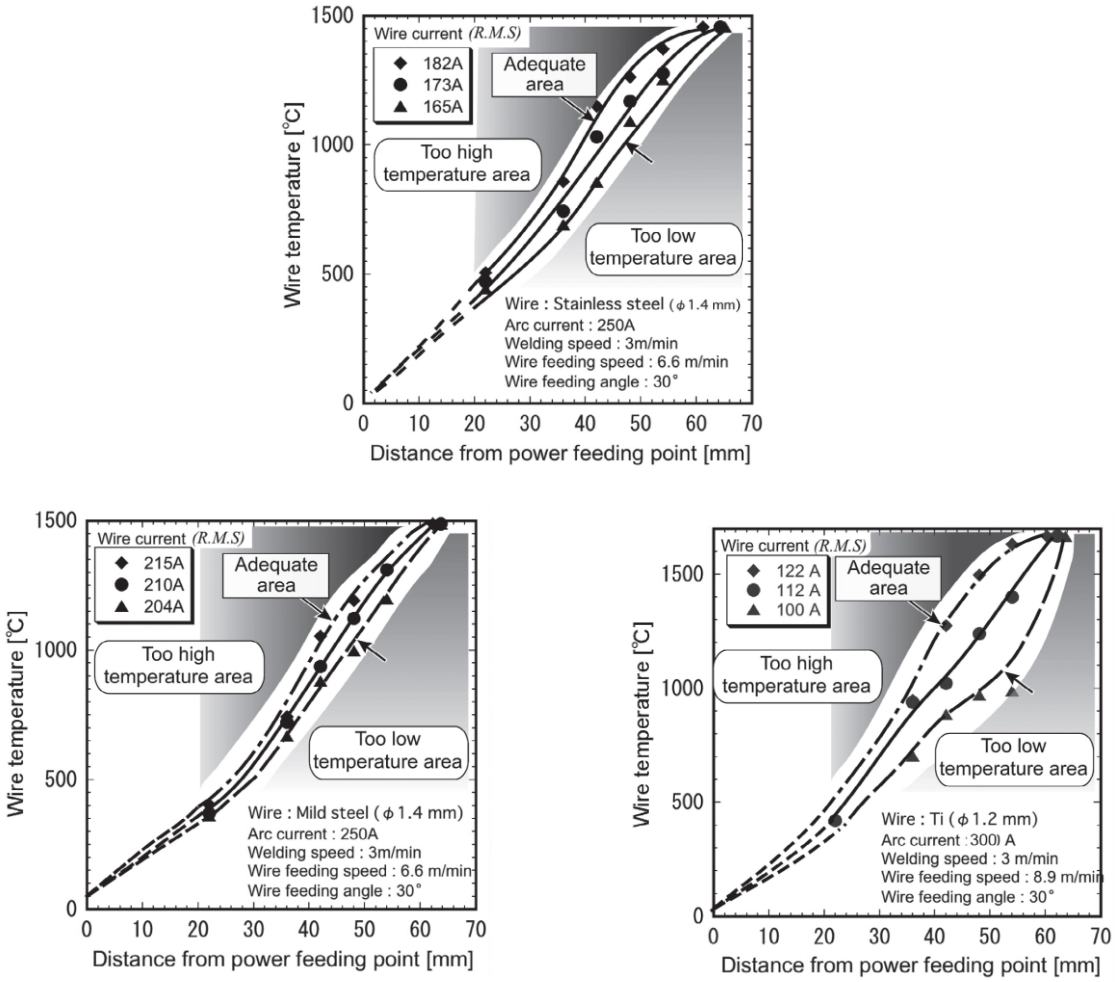

Fig. 2.8. Temperature distribution of the three types filler materials from the power feeding point [138].

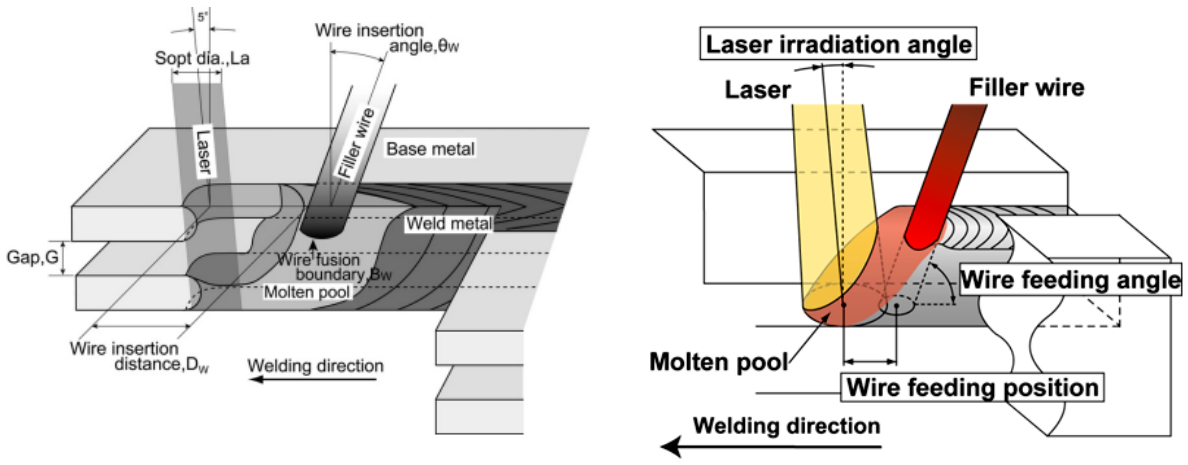

(a) (b)

Fig. 2.9. Schematic illustration of hot-wire laser welding method:
(a) lap-joint; (b) narrow-gap joints [140, 141].

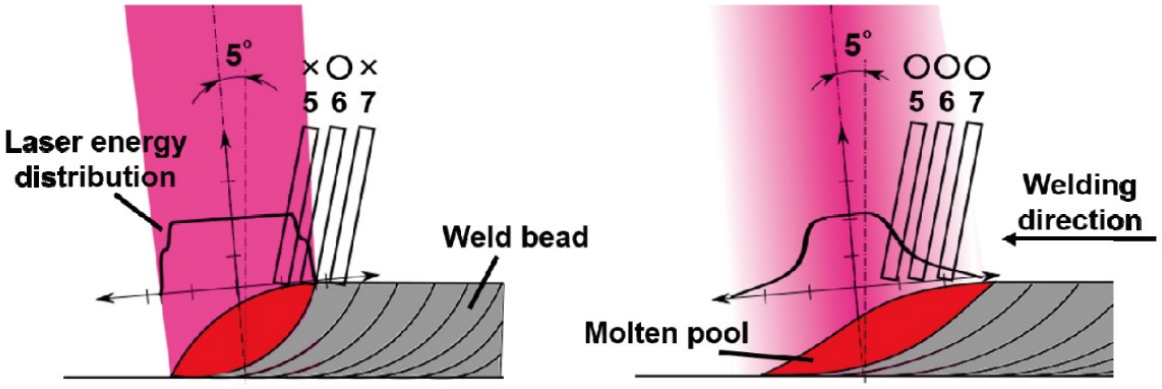

Fig. 2.10. Effect of wire feeding position on welding phenomenon [143].

The advantages of the hot-wire laser method compared with the cold-wire laser method are a higher productivity without an increase in heat input, a high freedom in material choice, and a high material utilization [140-142]. Liu et al. [138] found that the laser process with a hot wire reduced the laser power consumption and heat input. Bambach et al. [144] compared the laser deposition performance using powder, cold wire, and hot-wire of Inconel 718, and found that the hot-wire process improved the deposition rate by ~100 cm^3/h compared with the cold-wire process. Nie et al. [145] studied the high deposited rates of H13 steel with a low laser power (6 kW) by the combination of hot-wire system and laser beam. Nurminen et al. [146] compared laser processes using powder, cold-wire, and hot-wire feeding and found that the laser process with the hot wire reduced the dilution rate and increased the deposition rate. The hot-wire process improved the deposition efficiency two to four times compared with the powder and cold-wire processes. Wei et al. [147] found that the laser process with hot-wire feeding improved the energy efficiency coefficient and reduced the energy consumption by ~16% compared with the cold-wire process. Through the above-mentioned various reasons, the high power diode laser with hot-wire feeding system would be targeted as an interesting method because of its impressive high deposition rate and high material use rate (80-100%).

Hot-wire as a feedstock in WMAM processes has been used mainly with arc [148], plasma [149], laser beam heat source [145]. Hot-wire as an independent heat source in AM processes can modify cooling rate, improve deposition efficiency, and improve formation of ferrite in comparison with cold-wire. Fu et al. [132] found that the WAAM process with hot-wire could significantly reduce porosity and improve the wire deposition rate from 86 cm^3/h to 301 cm^3/h. To reduce the heat input, ultracold-wire arc AM and hot wire WAAM have been proposed by Rodrigues et al. [150] and Li et al. [148]. Poolperm et al. [151] proposed that the advantages of the hot-wire plasma welding process compared with the cold-wire plasma welding are higher design flexibility, a higher deposited quality, and a lower dilution percentage. However, the hot-wire based on arc and plasma heat source has several limitations,

such as the high heat input and messy work environment. The novel hot-wire laser process with a high-power diode laser has been investigated and developed [152, 153]. In HLAM, the diode laser has advantages of beam shape flexibility, a large beam creation (beam width over 10 mm), and a highly controllable and uniform energy distribution (1 mm × 12 mm rectangular spot) in a large beam spot compared with the fiber laser (0.4–1 mm circular spot) [154]. The HLAM combined with a high-power diode laser has a large potential to produce a large, wide, and flexible-sized product with a high productivity, a high material utilization, and a low heat input.

Chapter 3

A study of appropriate current calculation method of various wires using hot-wire method

3.1 Introduction

A suitable hot-wire current is the dominant parameter for guaranteeing stable melting. The theoretical studies [134, 137, 141-143] proposed that the appropriate temperature of the hot-wire tip is near its melting point. In the HLAM, it is time-consuming to obtain the appropriate hot-wire current for multi-layer deposition. However, there remains a lack of studies regarding calculated methods for selecting the appropriate hot-wire current for various filler materials. Thus, based on the heat equivalent and heat conservation, a simple current calculation method of hot-wire was proposed to calculate the appropriate current of various materials and estimate the wire temperature distribution.

It is also complicated to control the temperature of the preheating filler hot wire. There are many process parameters, such as the wire feeding speed, wire current, wire diameters, and material physical properties cause three modes in the hot-wire feeding such as fusing mode, continuous mode, and stick mode. Moreover, unsuitable hot-wire current value caused fusing mode and stick mode resulted in discontinuous bead with defects [55, 138, 139].

This chapter proposes a simple calculation method to predict the appropriate hot-wire current for heating the wire tip to nearly its melting point for four types of wire materials (SUS308L, SUS630, Inconel625, and A5356WY). Hot-wire feeding experiments without laser irradiation were performed to experimentally obtain the appropriate wire current and confirm the calculated values. The appropriate current value under different conditions (e.g. wire feeding speed, temperature-dependent specific heat, temperature-dependent specific gravity, and temperature-dependent specific electrical resistivity) was studied in detail. Moreover, the melting phenomenon of the filler wire was observed in detail using a high-speed camera.

3.2 Methodology of hot-wire heating phenomena and appropriate hot-wire current

3.2.1 Introduction of the equipment using in hot-wire heating experiment

Figure 3.1a shows the experimental setup of hot-wire heating on a plate without laser irradiation for the four types of filler wires. The hot-wire heating system

consisted of a hot-wire feeder / power supply, a two-axis slider, and a high-speed monitoring camera, as shown in Fig. 3.1b. The specimen was moved and fixed by the jig on the two-axis slider. The inverter hot-wire feeder / power supply equipment (Babcock-Hitachi K.K.; IV1320) was used to heating the cold wire to near its melting point, as shown in Fig. 3.2. A filler wire for hot wire is electrically heated through a positive-direct current base on Joule heating's principle. The two-axis slider (IAI RCS-2SS8C) was used to control the X-Y axis movement of the workpiece. The high-speed camera (HX-7, NAC Co., Ltd, Japan) with a lighting equipment assisted was used to monitor the wire feeding phenomenon and bead formation for various process conditions.

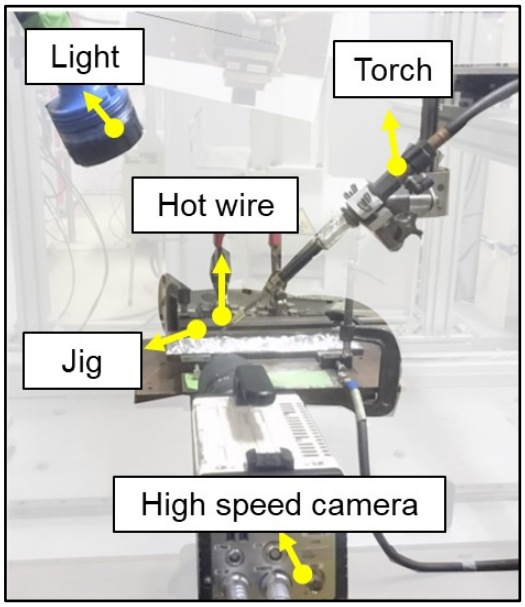

(a)

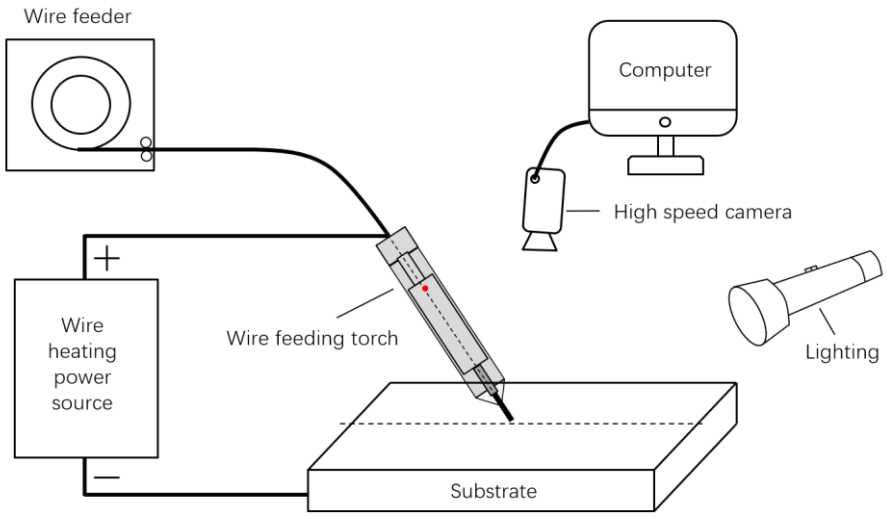

(b)

Fig. 3.1. Experimental setup of hot-wire heating on a plate without laser irradiation.

Fig. 3.2. Hot-wire feeder / power supply machine.

3.2.2 Materials used

The hot-wires heating experiment has been investigated in terms of application to the three types of metallic materials: Stainless steel, Ni-based alloy, and 5xxx series Al alloy. Four filler wires with a 1.2-mm diameter were used: 308L stainless steel, 630 stainless steel, 625 Ni-based alloy, and A5356WY Al alloy. 590 MPa-class steel plates with 12-mm thickness and 490 MPa-class steel plates with 9-mm thickness were used as a base plate for the SUS308L, SUS630, and Inconel625 filler wires. A5083O with 20-mm thickness were also used for the A5356WY filler wire, as shown in Fig. 3.3. The chemical compositions of the filler wires and base metals are shown in Tables 3.1 and 3.2. The surface of the base metal was polished and cleaned using acetone to remove oxide scaling before the experiment.

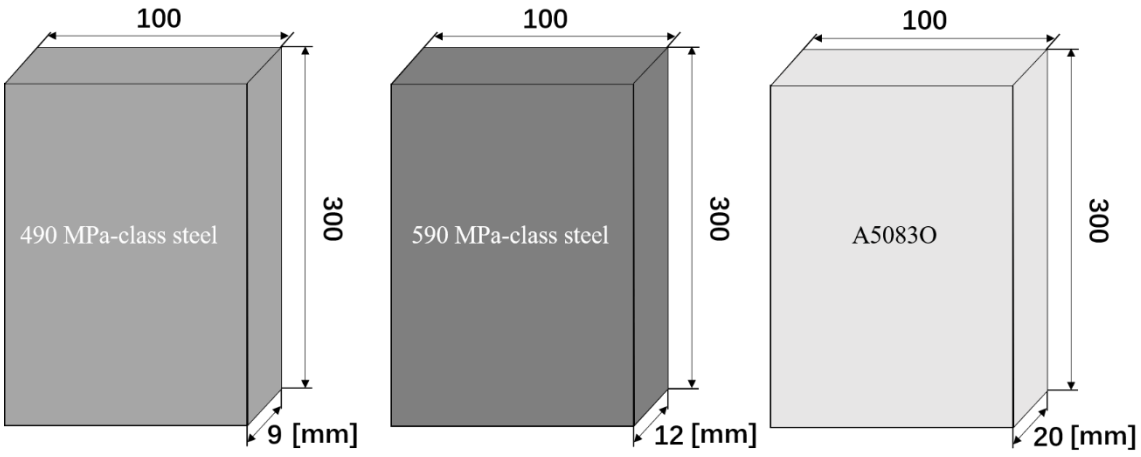

Fig. 3.3. Schematic diagrams of base metal.

Table 3.1 Chemical compositions of stainless steel and Ni-based alloy

Material	Chemical composition, mass%										
	C	Si	Mn	P	S	Ni	Cr	Mo	Cu	Nb+Ta	Fe
SUS308L	0.01	0.38	1.60	0.024	0.001	9.98	19.87	0.09	-	-	Bal.
SUS630	0.02	0.42	0.51	0.022	0.001	4.80	16.16	0.06	3.34	0.22	Bal.
Inconel625	0.02	0.09	0.01	0.003	0.001	Bal.	22.2	9.24	-	3.54	0.4
590 MPa-class steel	0.08	0.38	1.50	0.011	0.002	0.01	0.21	0.01	-	-	Bal.
490 MPa-class steel	0.15	0.45	1.52	0.007	0.002	-	-	-	-	-	Bal.

Table 3.2 Chemical compositions of Al alloys

Material	Chemical composition, mass%					
	Si	Mg	Mn	Cr	Zn	Al
A5356WY	0.25	4.5~5.5	0.05~0.20	0.05~0.20	0.1	Bal.
A5083O	<0.4	4.0~4.9	0.4~1.0	0.002	<0.25	Bal.

3.2.3 Process conditions

Table 3.3 lists the process conditions of the hot-wire heating experiment without laser irradiation. The process parameters of the wire feeding speed and wire current were varied to obtain the appropriate wire current depending on the filler wire material and wire feeding speed. The wire feeding rate (i.e., wire feeding speed / process speed), which indicates the deposition volume per length, was varied by changing the combination of process speed and wire feeding speed. The power supply distance is the distance between the power supply point and the substrate along the feeding direction. For the same hot-wire current value, the longer the power supply distance is, the longer the heating time and the higher and stabler the temperature distribution are. The wire feeding speed was various from 0 to 20 m/min, wire current was various from 93 A to 314 A, the power supply distance of 50 mm and 70 mm. The wire feeding angle fixed as 45° combine with forward wire feeding direction was used in this experiment.

Table 3.3 Process conditions of hot-wire heating experiment

Wire type	SUS308L(Φ1.2mm)					Inconel625(Φ1.2mm)			
Wire feeding rate	4.2	2.1	2.1	2.1		10	20	20	20
Wire feeding speed, m/min	5.0	10.0	15.0	20.0		5.0	10.0	15.0	20.0
Wire current, A	118	161	201	234		111	158	197	220
Process speed, m/min	1.2	4.8	7.2	9.6		0.5	0.5	1.0	1.5
Wire feeding direction	Forward					Forward			
Wire feeding angle, deg.	45					45			
Power supply point, mm	50					50			
Wire type	A5356WY(Φ1.2mm)					SUS630(Φ1.2mm)			
Wire feeding rate	1.0	1.0	1.0	1.0		4.2	2.1	2.1	2.1
Wire feeding speed, m/min	5.0	10.0	15.0	20.0		5.0	10.0	15.0	20.0
Wire current, A	173	230	284	314		93	131	161	186
Process speed, m/min	4.8	9.6	14.4	19.2		1.2	4.8	7.2	9.6
Wire feeding direction	Forward					Forward			
Wire feeding angle, deg.	45					45			
Power supply point, mm	50					70			

3.3 Hot-wire feeding experiments without laser irradiation

An appropriate hot-wire current is the key point for guaranteeing continuous and smooth wire feeding. Various hot-wire current cause such three types in the hot-

wire feeding as fusing mode, smooth mode and stick mode. Figure 3.4 shows high-speed images that indicate three typical types of hot-wire feeding phenomena without laser irradiation, sticking type, smooth feeding type, and fusing type. The SUS308L wire using a fixed wire feeding speed (V_F) of 15 m/min, process speed (V_P) of 7.2 m/min, and wire feeding rate (V_F / V_P) of 2. When the wire current was low, the hot-wire tip stuck on the substrate surface frequently, and unstable wire feeding occurred because insufficient wire heating could not increase the wire tip temperature (see Fig. 3.4a). When the wire current was excessively high, fusing and spattering occurred because the hot-wire temperature reached its melting point before contacting the substrate (see Fig. 3.4c). When the wire current was set to an appropriate value, the hot wire heated to its melting point at the wire tip on the substrate surface, and smooth and stable feeding was achieved (see Fig. 3.4b). The same tendency was confirmed for all hot-wire feeding speeds from 5 to 20 m/min. The estimates and experimental investigations showed that the wire tip temperature must be near its melting point to achieve smooth and stable hot-wire feeding with a high feeding speed by setting the appropriate wire current. Efficient hot-wire feeding can be achieved on many filler wire types by setting the appropriate wire current that was estimated by using the proposed calculation method based on each material property.

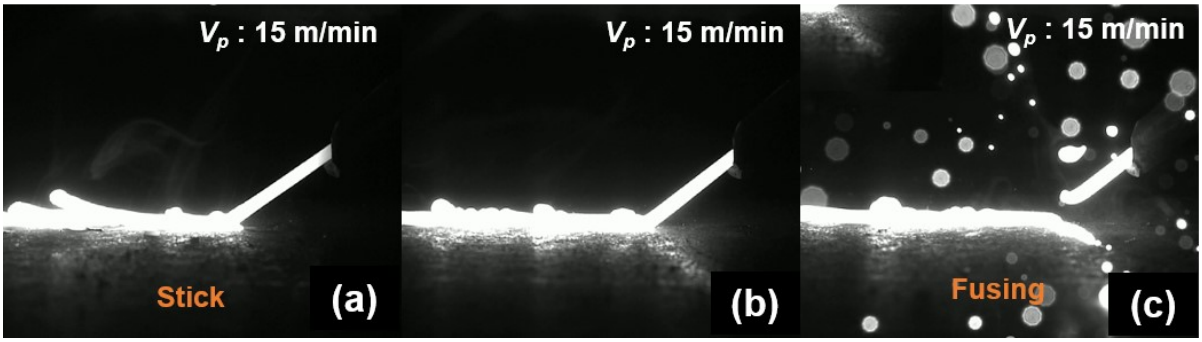

Fig. 3.4. Typical hot-wire heating phenomenon of SUS308L:
(a) stick mode; (b) smooth mode; (c) fusing mode.

Figure 3.5 shows the wire heating phenomena produced by three different wire currents (153, 158, 163 A) and Inconel625 wire using a fixed wire feeding speed of 10 m/min, process speed of 0.5 m/min, and wire feeding rate of 20. It is difficult to judge the melting phenomenon by using the Al-alloy wire, which covered with an oxide film on wire surface. Thus, the evaluation was based on the time sequence melting behavior of the hot-wire from the high-speed image of the experiment. Figure 3.6 shows the time sequence of high speed image of A5356WY produced by three different wire currents (224, 230, 236 A). At this stage, the wire feeding rate was

fixed at 1, a process speed of 9.6 m/min, a wire feeding speed of 10 m/min, and a wire feeding angle of 45 degrees was used.

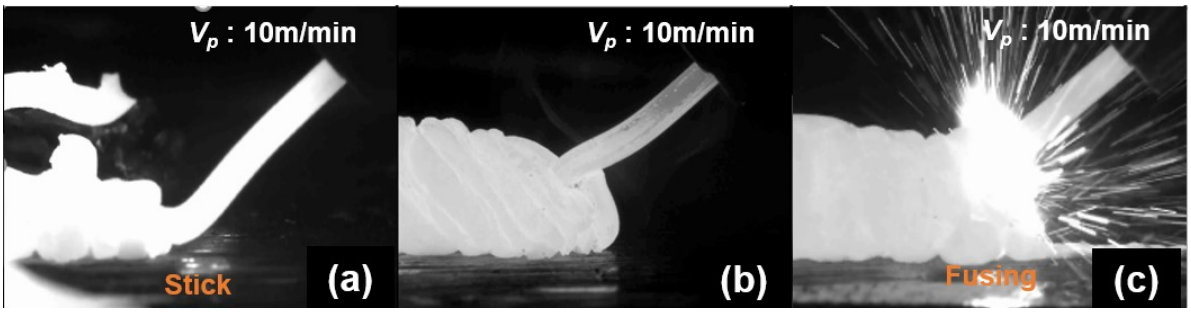

Fig. 3.5. Typical hot-wire heating phenomenon of Inconel625:
(a) 153 A; (b) 158 A; (c) 163 A.

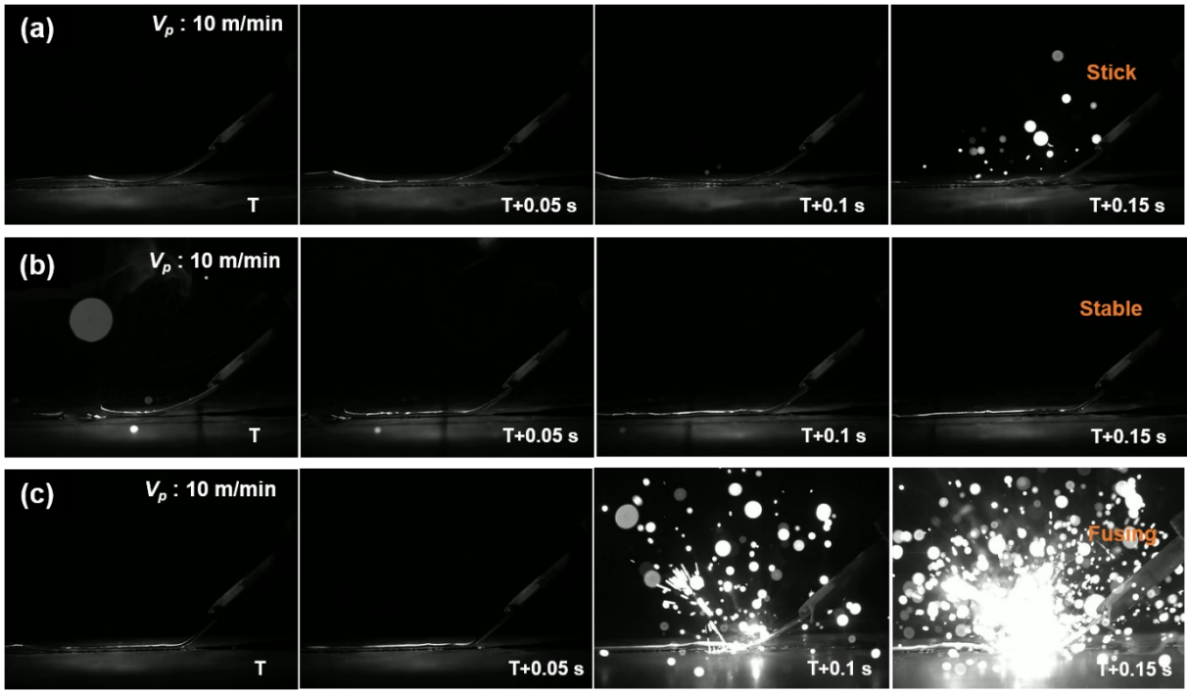

Fig. 3.6. Time sequence of high speed image of A5356WY:
(a) 224 A; (b) 230 A; (c) 236 A.

Figure 3.5a and Figure 3.6a show that the filler wire tip poked the base metal surface, and an unstable metal bead was deposited. This phenomenon occurred because of the relatively low wire current, which could not properly heat the wire tip to its melting point. The insufficient temperature of the hot-wire tip could then not achieve smooth deposition on the base plate. With the hot-wire current was increased (see Fig. 3.5c and Fig. 3.6c), the fusing frequently occurred at the hot-wire tip with spatters. This phenomenon occurred because of the excessive wire current, which brought the wire tip temperature to its melting point before contacting the base

plate surface. When the appropriate hot-wire current was applied (see Fig. 3.5b and Fig. 3.6b), smooth hot-wire feeding was observed and a uniform bead stably formed.

Figure 3.7 shows the appropriate hot-wire current of the three filler materials for wire feeding speeds varied between 5 and 20 m/min. The tendency of the wire current increment was the same, and the appropriate hot-wire current was increased when the wire feeding speed increased from 5 to 20 m/min. The appropriate current of the A5356WY wire is considerably higher than that of the SUS308L and Inconel625 wires on a fixed wire feeding speed because of its lower electric resistance.

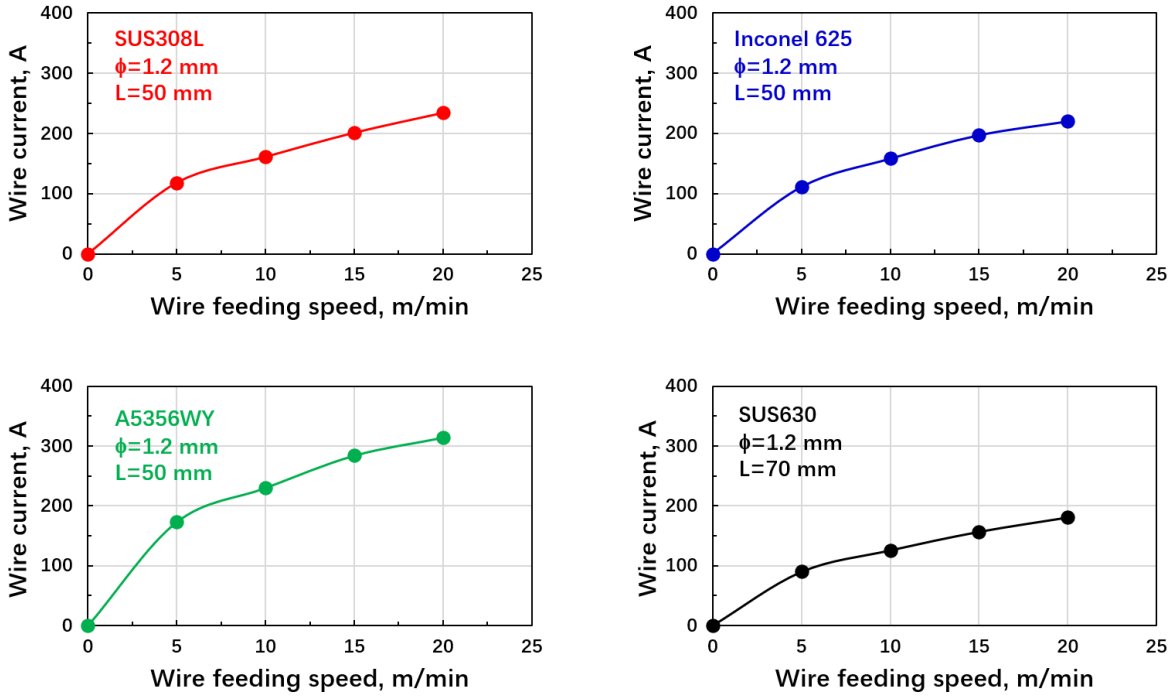

Fig. 3.7. Appropriate hot-wire currents for each filler material obtained by hot-wire heating experiments without laser irradiation.

3.4 Simple calculation method for estimating appropriate hot-wire current

3.4.1 Introduction of simple calculation model

A simple theoretical calculation method for deriving the appropriate hot-wire current is proposed to more flexibly use various materials in the HLAM process. Figure 3.8 shows a schematic diagram of the proposed calculation method. The distance between the power supply point and substrate is defined as the wire supply distance, which is the Joule heating region, as shown in Fig. 3.8a. The temperature distribution is calculated according to the power supply distance, as shown in Fig. 3.8b. This method divides the power supply distance into a small length of 0.1 mm,

and the overall temperature distribution can be obtained by calculating the temperature increment at each 0.1-mm segment. Three factors are taken into account in the simple calculation method, namely the (1) heat generated by Joule heat, (2) heat generated by contact resistance, and (3) heat loss from heat convection. The Joule heat and contact resistance are the main factors for the temperature rise of the hot-wire, whereas heat convection is considered as the main mechanism of heat loss during the wire heating process. The precise temperature distribution with power supply distance and the temperature at the hot-wire tip can be obtained by calculating the temperature increase in each segment.

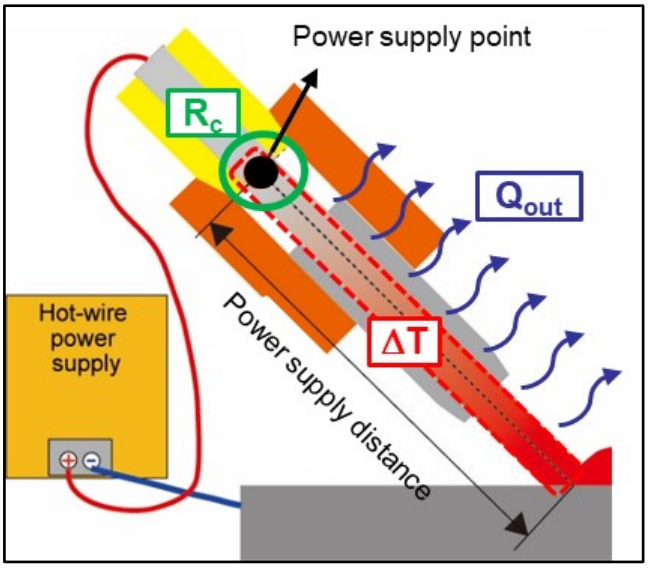

(a)

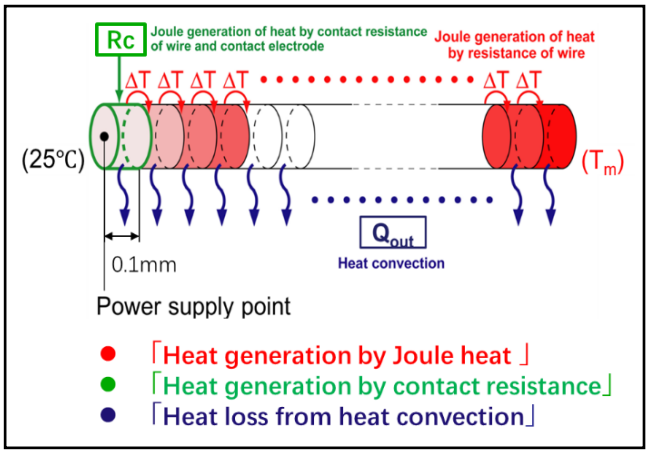

(b)

Fig. 3.8. Schematic diagrams of the simple method for calculating the appropriate hot-wire current.

3.4.2 Simple calculation equations

The amount of temperature increment for each element was calculated, and the temperature distribution of the entire wire was obtained by repeating the calculation from the feeding point to the tip of the wire and adding the amount of temperature increment, as shown in Fig. 3.8.

Firstly, the resistance for each element was calculated from the equation. Then, the energizing time for each element was calculated from the formula. Using the resistance per element and the energization time per element, the amount of heat obtained by Joule heat generation per element was calculated from the equation. Finally, the amount of temperature increment obtained by each element due to Joule heat generation was calculated from the equations. The above calculation was started from the feeding point and repeated until the end of the wire. The appropriate preheated hot-wire current is the temperature of the wire tip is near the melting point just before the tip of the wire hits the molten pool. The detail of steps and equations as follows:

Calculate the temperature increment for each segment, repeat the calculation from the power supply point to the wire tip, and add up the temperature increment. Thus, the temperature increment (ΔT) on each 0.1-mm segment is given as:

$$\Delta T = Q / (C_{(T)} \times m_{(T)} \times L \times \Pi r^2) \quad (3.1)$$

Where $C_{(T)}$ is the temperature-dependent specific heat (J/kg·°C), $m_{(T)}$ is the temperature-dependent specific gravity (kg/m^3), r is the radius of the filler wire (mm), and L is the segment length (0.1 mm).

The net heat increase Q is equal to the gap between the heat generated by the Joule heat into the segment (Q_{in}) and the heat loss from the segment (Q_{out}), which is given as:

$$Q = Q_{in} - Q_{out} \quad (3.2)$$

Where Q_{in} is the heat generated by the temperature-dependent electric resistance of the filler wire material of each 0.1-mm segment (J), and can be described as:

$$Q_{in} = R_{(T)} \times I^2 \times t \quad (3.3)$$

Where $R_{(T)}$ is the temperature-dependent resistance of the filler material (Ω), I is the hot-wire heating current (A), and t is the heating time through segment length L (s). Then, the temperature-dependent electric resistance $R_{(T)}$ is given as follows:

$$R = (R_C + \rho_{(T)}) \times L / \Pi \times r^2 \quad (3.4)$$

Where $\rho_{(T)}$ is the temperature-dependent specific electrical resistivity (Ω·m), and R_C is the contact resistance (Ω). The heating time t through a segment length L (0.1 mm) is given as:

$$t = D \times 60 \times L / V_F \quad (3.5)$$

Where D is the duty ratio (50%) of the wire heating current, and V_F is the wire feeding speed (m/min).

Q_{out} is the heat loss from heat convection to the atmosphere area during wire heating (J), and can be described as:

$$Q_{out} = h \times A \times \Delta T \quad (3.6)$$

$$A = \Pi \times r^2 \quad (3.7)$$

$$\Delta T = T_w - T_a \quad (3.8)$$

Where h is the comprehensive heat loss coefficient (W/m^2·K), A is the surface area of a segment (m^2), T_w is the temperature of the filler wire (°C), and T_a is the air temperature (°C).

By substituting Eqs. (3.2)–(3.8) into Eq. (3.1), the temperature increment ΔT on each 0.1-mm segment can be described as:

$$\Delta T = \frac{I^2}{V_F} \times \frac{60 \times L \times D \times \left(R_C + \rho_{(T)}\right)}{\pi^2 \times r^2 \times C_{(T)} \times m_{(T)}} - \frac{h \times (T_w - T_a)}{C_{(T)} \times m_{(T)} \times L} \quad (3.9)$$

Equation (3.9) shows that the temperature increment of the filler wire is related to many factors, including the physical properties of the material, diameters of the filler wire, comprehensive heat loss coefficient, wire heating current, and wire feeding speed. As for the same material, the wire temperature increment in segment length L is positively correlated with the square of the wire current I, and negatively correlated with the wire feed speed V_F and filler wire diameter. The contact resistance R_C and comprehensive heat loss coefficient h are also important factors that affect the temperature increment during wire heating.

3.4.3 Physical properties

Figure 3.9a–c shows the physical properties of four materials used in this study, namely the temperature-dependent specific electrical resistivity, temperature-dependent specific gravity, and temperature-dependent specific heat, respectively.

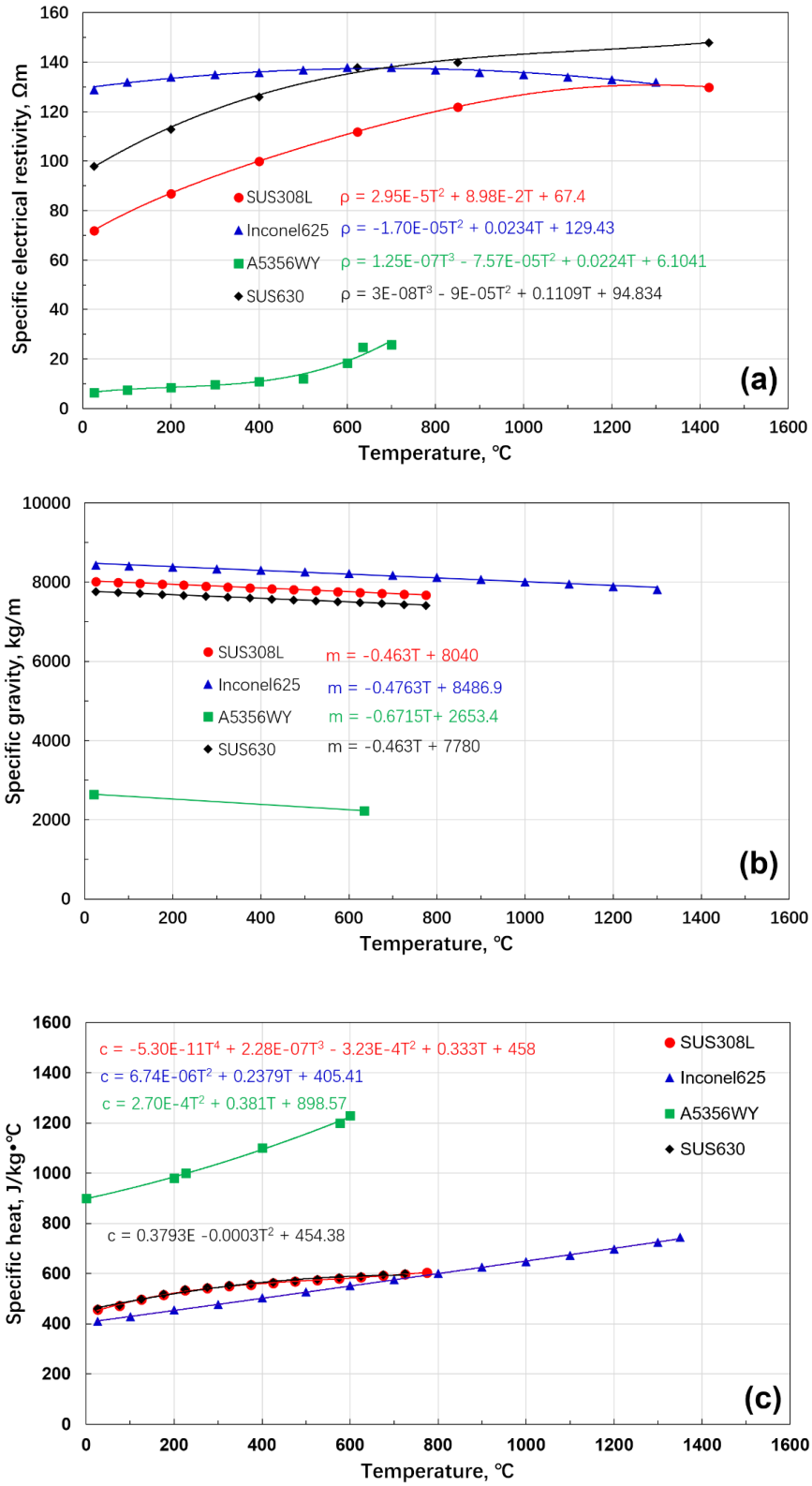

Fig. 3.9. Physical properties of the four investigated materials:
(a) temperature-dependent specific electrical resistivity; (b) temperature-dependent specific gravity; and (c) temperature-dependent specific heat [155-160].

In order to clear the physical properties of four materials, these were used in the calculation by making an approximate expression by the method of least squares. the equations of the temperature-dependent specific electrical resistivity (ρ), temperature-dependent specific gravity (m), and temperature-dependent specific heat (c) are given as:

SUS308L

$$\rho = 2.95E - 5T^2 + 8.98E - 2T + 67.4 \quad (3.10)$$

$$m = -0.4637T + 8040 \quad (3.11)$$

$$c = -5.30E - 11T^4 + 2.28E - 07T^3 - 3.23E - 4T^2 + 0.333T + 458 \quad (3.12)$$

Inconel625

$$\rho = -1.70E - 05T^2 + 0.0234T + 129.43 \quad (3.13)$$

$$m = -0.4763T + 8486.9 \quad (3.14)$$

$$c = 6.74E - 06T + 0.2379T + 405.41 \quad (3.15)$$

A5356WY

$$\rho = 1.25E - 07T^3 - 7.75E - 05T^2 + 0.0224T + 6.1041 \quad (3.16)$$

$$m = -0.6715T + 2653.4 \quad (3.17)$$

$$c = 2.70E - 4T^2 + 0.381T + 898.57 \quad (3.18)$$

SUS630

$$\rho = 3E - 08T^3 - 9E - 05T^2 + 0.1109T + 94.834 \quad (3.19)$$

$$m = -0.463T + 7780 \quad (3.20)$$

$$c = 0.3793E – 0.0003T^2 + 454.38 \quad (3.21)$$

3.4.4 Pulse current

In the calculated method, the hot-wire heating current (A) and heating time through segment length L (t) are related to the pulse current. As shown in Eq. 3.3, the Joule heating value is proportional to the square of the wire current value. The pulse current can be divided into two types: real pulse current and ideal pulse current, as shown in Fig. 3.10a. The ideal pulse current is generated with no buffer at the current rising and falling time. Therefore, the pulse current that generates the same amount of heat as the actual pulse current was reproduced and reflected in the wire temperature calculation method. The squared value of the actual pulse current and the squared value of the ideal pulse current was integrated over the unit pulse period. The ratio of the squared value of the actual pulse current to the squared value of the ideal pulse current was then calculated. This was done for 100 arbitrary pulse currents, and the average value was calculated. The squared integral of the actual pulse current was found to be 97.22% of the squared integral of the ideal pulse current, as shown in Fig. 3.10b.

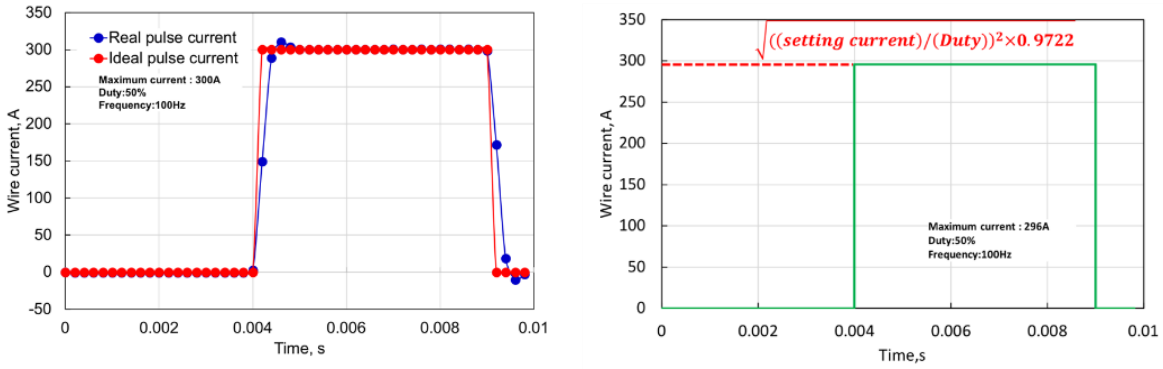

(a) (b)

Fig. 3.10. Pulse current used in hot-wire system

3.5 Effect of contact resistance and heat loss coefficient

The heat generated by the contact resistance between the filler wire and contact tip during the wire heating process must also be discussed in detail. Heat is lost from the periphery of each segment during wire heating. The heat dissipation to the periphery of the wire is calculated by assuming the comprehensive heat loss coefficient h, which is proportional to the temperature difference between the surface area of the wire and the air environment.

The hot-wire tip temperature was estimated according to the following four thermodynamic assumptions for the comprehensive heat loss coefficient and contact resistance:

1) The heat loss from heat convection and heat generation by contact resistance are ignored (h = 0, R_C = 0).
2) The heat loss from heat convection is considered, but the heat generation by contact resistance is ignored (R_C = 0).
3) The heat generation by contact resistance is considered, but the heat loss from heat convection is ignored (h = 0).
4) The heat loss from heat convection and heat generation by contact resistance are both considered.

Figures 3.11a–c show the calculated appropriate hot-wire currents for SUS308L, Inconel625, A5356WY, and SUS630, respectively. The results are calculated based on the above four assumptions, and the measured results are shown in all three graphs. When heat loss is ignored (h = 0), the appropriate wire current required to heat the wire tip to its melting point (red circles and green squares in Fig. 3.11) is lower than that when the heat loss is considered (h = 1) (blue triangles and black diamonds symbols in Fig. 3.11). There are also small differences of the calculated wire current reductions between the red and blue symbols and green and black symbols for all four filler materials. In terms of the contact resistance effect, the largest effect was observed for the A5356WY filler wire (i.e., the largest difference between the red and green symbols and blue and black symbols), whereas the smallest effect was observed for the Inconel625 filler wire (i.e., negligible differences between the associated symbols). The SUS308L and SUS630 filler wire showed intermediate differences in the calculated wire current, reflecting an intermediate effect of the contact resistance.

The above results indicate that the contact resistance largely affects the temperature increase of material with relatively low electrical resistivity at approximately room temperature (i.e., at the power supply point) because the contact resistance becomes relatively larger than the material electrical resistivity at that point. Figure 3.9a shows that the electrical resistivity follows SUS308L < SUS630 < Inconel625 when the temperature is lower than 700 °C, while the electrical resistivity follows SUS308L < Inconel625 < SUS630 when the temperature is higher than 700 °C. Compared with the other materials, the electrical resistivity of A5356WY is the lowest. A comparison of the four types of the calculated wire current and appropriate wire current obtained by the experiments shows that the assumption that considers both the heat loss from heat convection and heat generation by contact resistance yields the best agreement, as indicated by the black diamond symbols in Fig. 3.11.

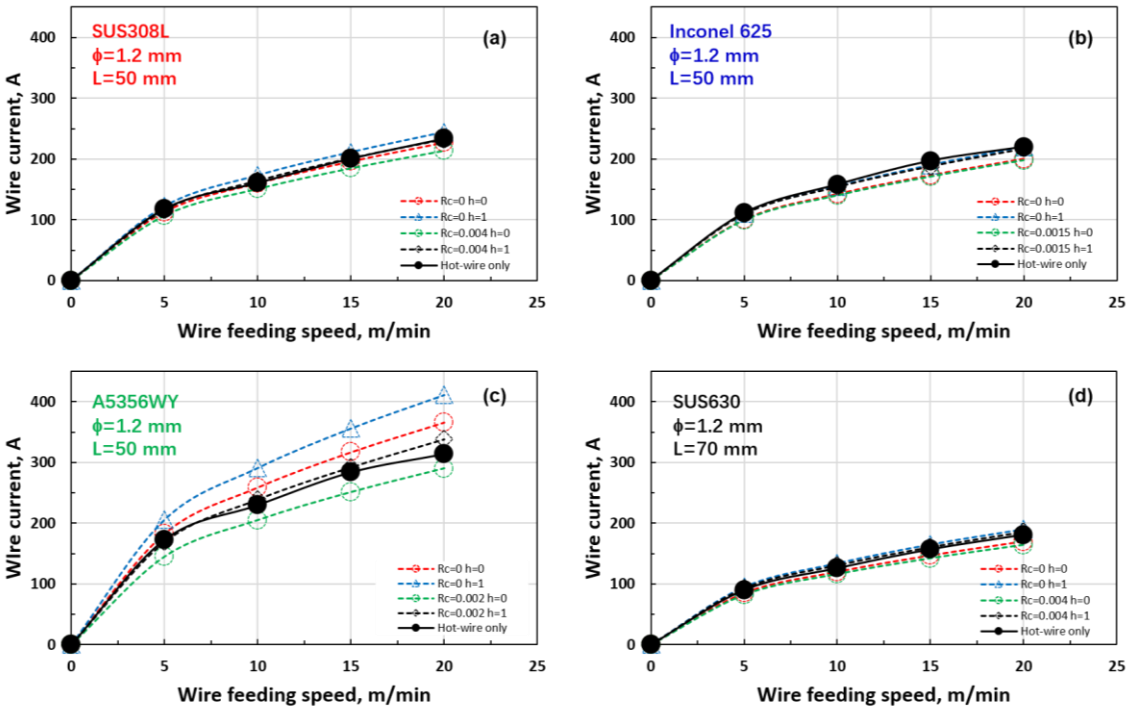

Fig. 3.11. Calculated appropriate hot-wire currents and experimental results.

3.6 Summary

In this chapter, four types of filler materials (SUS308L, Inconel 625, A5356WY, and SUS630) were used in a hot-wire heating on the plate without laser irradiation experiment. The effect of the hot-wire current on the stability of the wire feeding phenomenon was investigated. A simple calculation method is proposed and its estimated result was confirmed by the experimental investigation. The conclusions are summarized as follows:

1) The hot-wire heating current is an important parameter to achieve stable and smooth wire feeding. Excessively low and high wire currents result in insufficient wire-tip temperature with poking on the base metal surface and fusing and spatter formation, respectively.

2) A simple calculation method is proposed to estimate the appropriate hot-wire current. As for the same material, the wire temperature increment in segment length L is positively correlated with the square of the wire current I, and negatively correlated with the wire feed speed V_F and filler wire diameter.

3) The estimated current is in good agreement with the experimental values over a wide range of wire feeding speeds from 0 to 20 m/min for all four filler materials, considering both heat loss from heat convection and heat generation by contact resistance.

Chapter 4

Development of the AM technology by using hot-wire system and high-power diode laser

4.1 Introduction

According to the previous study in Chapter 3, a simple method for calculating the appropriate wire current of four types of wires was investigated. Through this calculation method, the appropriate current of filler wire could be obtained under various wire feeding speed. The originality purpose of this study is to a combination of the diode laser irradiation and hot wire method. However, calculated results and experimental results were established under the condition without the laser irradiation, it needs to be combined with a laser heat resource to realize the manufacturing of the multi-layer deposition.

In this chapter, the suitable process conditions for SUS308L filler wire were investigated by hot-wire laser AM using a high-power diode laser as the main heat source with a large rectangular beam spot. Firstly, A high-speed camera was used to observe the molten pool formation and hot-wire feeding during the HLAM experiments to clearly investigate the deposition process phenomena. Effect of wire feeding rate on first and second-layer evaluated parameters (e.g. bead width and bead height) was investigated. Secondly, a window of three-layer deposition for a combination of process parameters has been developed. There are many parameters involved in the process conditions, including laser power, process speed, wire feeding rate, and energy heat input, mainly affect the melting phenomenon and bead appearance of three-layer deposition. Finally, the effects of laser spot size on a bead shape and cross-sectional characteristics were investigated.

4.2 Introduction of multi-layer deposition equipment of the hot-wire laser AM method

Figure 4.1a shows the experimental setup of the HLAM to fabricate the multi-layer deposition. The HLAM system consisted of a 6-kW high-power diode laser with a combination of optical lenses, a hot-wire feeder / power supply, a two-axis slider, a six-axis robot, a high-speed monitoring camera, and a gas shielding box. The specimen was moved and its process speed was controlled by the two-axis slider, the six-axis robot set the laser irradiation angle, and the defocus length was set, as shown in Fig. 4.1b. The laser system used a 6 kW high-power diode laser (LDH 6000-40) and the laser head is fixed to a six-axis articulated robot (Kawasaki

Machine Systems, FS10N), so that the irradiation angle and defocus length of the laser could be changed as needed, as shown in Fig. 4.2. A high-speed camera with laser lighting and a band-pass filter were used for in-situ observation of wire melting and molten pool formation for all of the filler materials and process conditions, as shown in Fig 4.3 and Fig.4.4.

As a hot-wire system, a wire heating power supply (Babcock-Hitachi, IV1320) was used, and power was supplied from the wire feed nozzle to the base metal. The current value and wire feeding speed can be set using a built-in servo moto feeder. The heating of the wire was set to a pulse frequency of 100 Hz and a duty cycle of 50% per waveform. The temperature of the filler wire could be heating near to the melting point before entering into the molten pool. The specimens were fixed to the fixture of the processing table on the bi-axial table (IAI RCS-2SS8C).

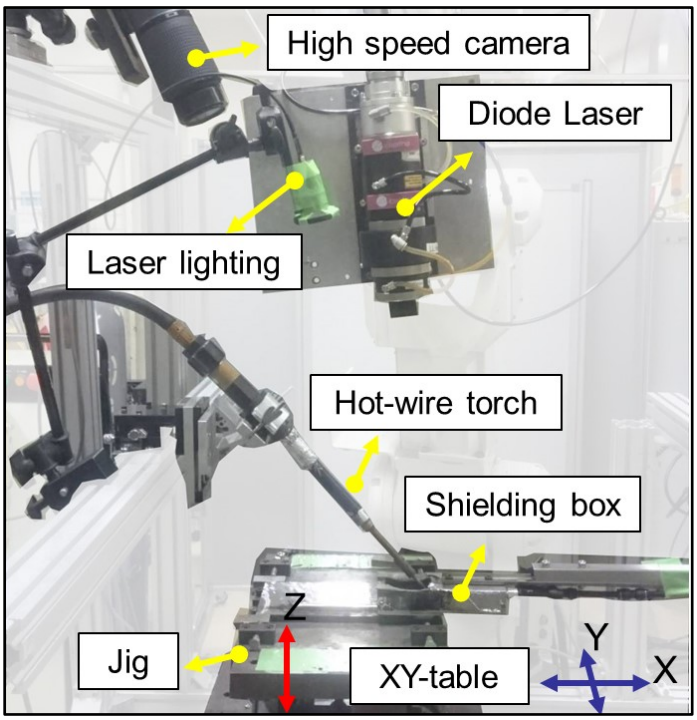

(a)

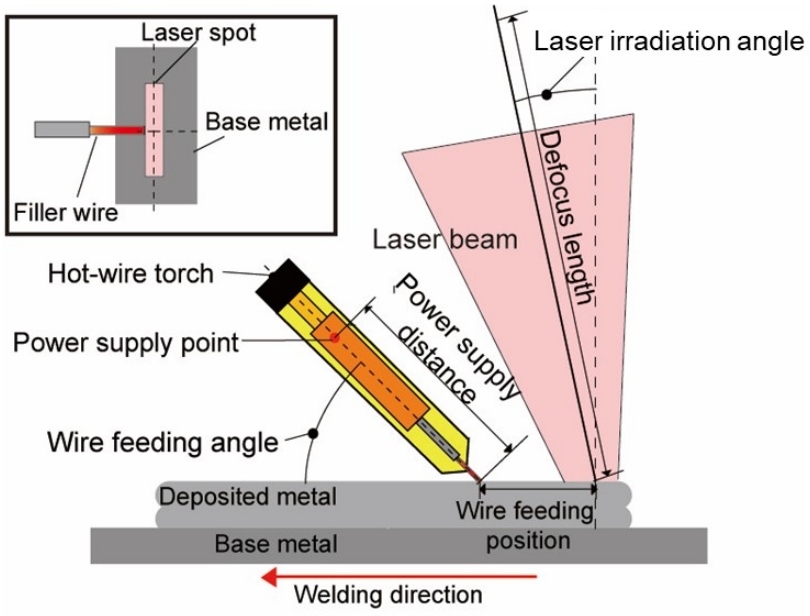

(b)

Fig. 4.1. Experimental setup of HLAM for fabricating multi-layer deposition.

Fig. 4.2. Diode laser oscillator.

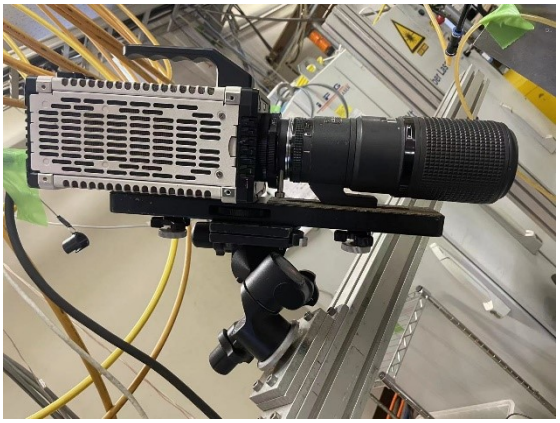

Fig. 4.3. High-speed camera.

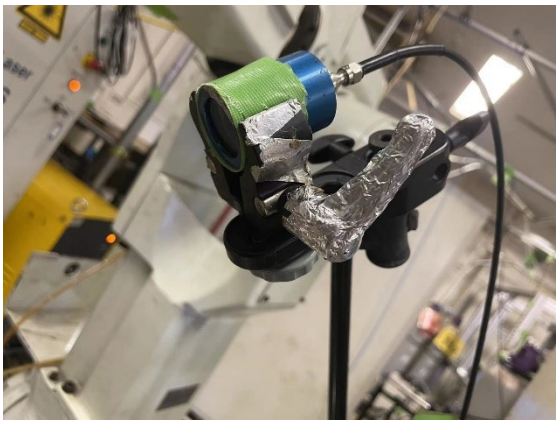

Fig. 4.4. Laser lighting equipment.

Table 4.1 Rectangular beam shapes with different focal length

Focal length (Focusing lens)								
Homogenizer (Type)		200	250	400	500	600	800	1000
Laser length	LL2.20	23	28	45	56	68	90	113
	LL2.35	13	16	26	32	39	51	64
	LL2.35-edge	13	16	26	32	39	51	64
	LL2.54	8	11	17	21	25	34	42
	LL2.85	5	7	11	13	16	21	27
	LL2.146	3	4	6	8	9	12	15
Laser width	Colli 100 mm (Core 0.4 mm)	0.8	1.0	1.6	2.0	2.4	3.2	4.0
	Colli 80 mm (Core 0.4 mm)	1.0	1.3	2.0	2.5	3.0	4.0	5.0
	Colli 100 mm (Core 1 mm)	2.0	3.0	4.0	5.0	6.0	8.0	10.0
	Colli 80 mm (Core 1 mm)	2.5	3.1	5.0	6.3	7.5	10.0	12.5

Table 4.1 shows the rectangular beam shapes with different focal length. The width and the length of laser spot can be selected by adjusting the combination of a homogenizing and focusing lenses. Figure 4.5 shows a schematic diagram of the laser head created by the combination of fiber core diameters, collimator lens, homogenizer, and focusing lens, which decided the rectangular beam width and length. In this study, the HLAM process used a 6-kW high-power diode laser with a large rectangle beam spot and a high-power wire heating power supply with a maximum current above 400 A.

Six kW is high-power compared with the PBF process; however, the HLAM process uses the much larger laser spot size — in other words, the laser energy distribution of HLAM is relatively small. In addition, the deposition rate of HLAM is much larger than that of PBF. The high-power wire heating power supply can heat the filler wire to its melting point under the high-speed condition for filler wire feeding. A specimen was fixed on a biaxial slide table to achieve precise and stable motion. The filler wire was fed from the front as the wire leading process

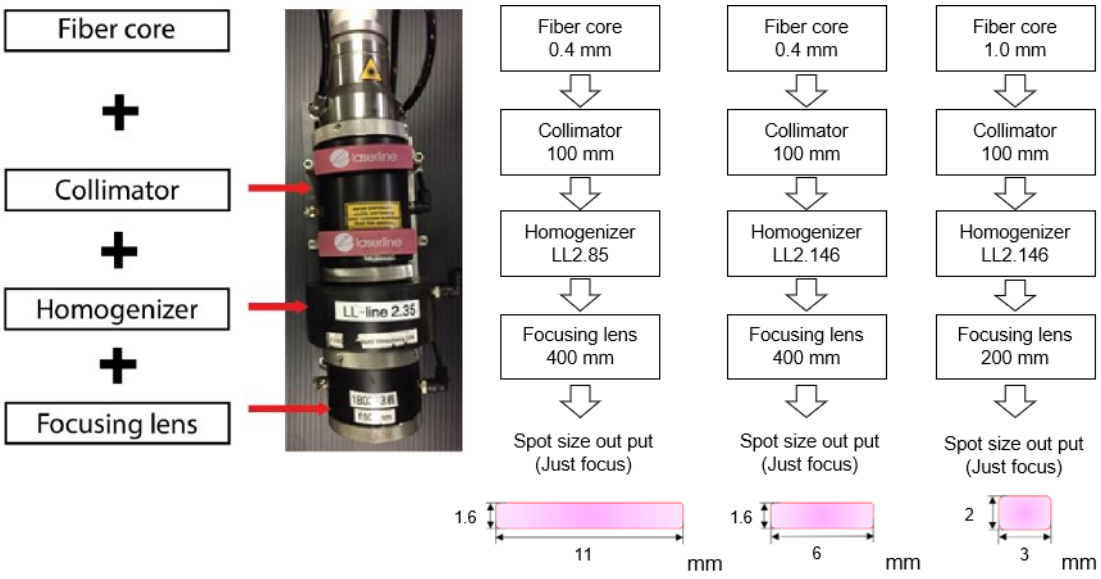

Fig. 4.5. Laser head and beam shape.

4.2.1 Materials used

A JIS-Z3321-YS308L filler wire with a 1.2-mm-diameter and a base metal of 590-MPa-class steel plate with a 200-mm length, a 100-mm width, and a 9-mm thickness were used. The chemical compositions of the filler wire and base metal are shown in Table 4.2. Oxide on the base-metal surface was polished and degreased with acetone before the experiment.

Table 4.2 Chemical compositions of filler wire and base metal

Material	Chemical composition, mass%								
	C	Si	Mn	P	S	Ni	Cr	Mo	Fe
SUS308L	0.01	0.38	1.60	0.024	0.001	9.98	19.87	0.09	Bal.
590 MPa-class steel	0.08	0.38	1.50	0.011	0.002	0.01	0.21	0.01	Bal.

4.2.2 Experimental procedure

Table 4.3 shows the range of process parameters selected from the HLAM experiment. The three types rectangular laser spot with a 5° laser irradiation angle of the laser beam were applied. The process parameters, such as laser power, process speed, wire current, and wire feeding rate (wire feeding speed / process speed) were varied respectively during the multi-layer deposition. The laser leading and the angle between the substrate and the filler wire of 45° were used. The high-purity argon gas was used for shielding the molten pool and prevent oxidation with a shielding box at a flow rate of 30 L/min.

Table 4.3 Process conditions.

Core, μm	400	400	1000
Homogenizer	LL-line2.85	LL-line2.146	LL-line2.146
Focus lens, mm	400	400	200
Collimator, mm	f100	f100	F80
Laser power, kW	3.3 ~ 5.5		
Defocus length, mm	0 (Just focus)		
Laser spot size, mm x mm	1.6^{W} x 11^{L}	1.6^{W} x 6^{L}	2.0^{W} x 3.0^{L}
Welding direction	Forward (wire leading)		
Power supply distance, mm	50		
Process speed (V_P), m/min	0.24 ~ 0.5		
Wire feeding speed(V_F), m/min	0.9 ~ 20		
Wire feeding rate, (V_F / V_P)	2.5 ~ 40		
Wire current, A	58 ~ 234		
Wire feeding angle, degree	45		
Wire feeding position, mm	0.8		
Shielding gas (Ar), L/min	30		

To clear the deposition process, the phenomenon of molten pool behavior during deposition was visually observed and recorded in situ using a high-speed camera (HX-7, NAC Co., Ltd, Japan). The monitoring conditions of the high-speed camera are listed in Table 4.4. The deposition process was illuminated with a lighting laser with a wavelength of 808 ± 5 nm to acquire bright images, while a bandpass filter with a transmitted wavelength of 808 ± 5 nm (Jena Optic Co., Ltd, Japan) was installed with an optical lens.

Table 4.4 Monitoring conditions of in-situ observation.

High-speed camera	HX-7
Frame rate, fps	1000
Aperture	Closed
Focus lens, mm	200
Band pass filter, nm/FWHM	808 ± 5
Wave length, μm	808 ± 5
Laser lighting, W	30
Shutter speed, s	1/5000

4.2.3 Typical bead appearance and melting phenomenon

Figure 4.6 shows typical bead appearances of three-layer depositions of sound beads and wire stubbing beads. After calculating the hot-wire current by the previous method, sound beads without defects were obtained by combining suitable process parameters (see Fig. 4.7a). When the process parameters were unsuitable, for example, the wire feeding rate was greater than the constant combination of laser power and process speed, and a low-quality bead like wire stubbing was observed (see Fig. 4.7b).

Fig. 4.6. Typical bead appearance of SUS308L wire.

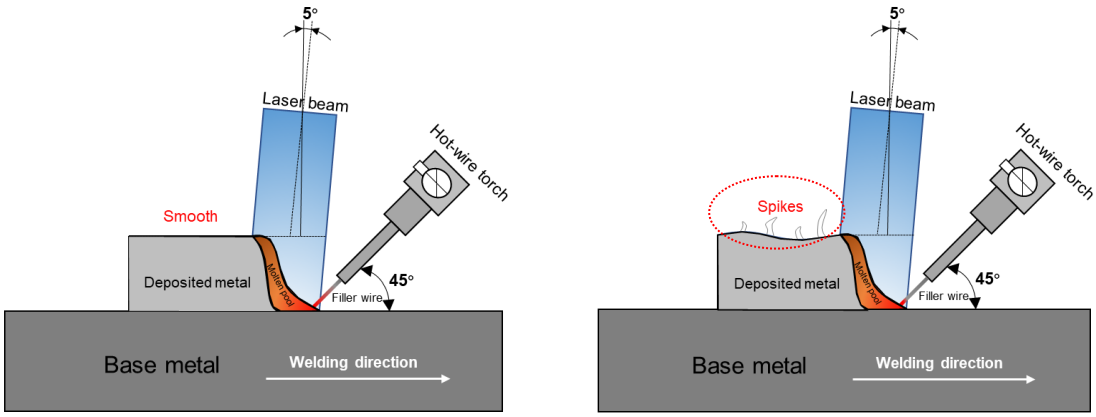

(a) (b)

Fig. 4.7. Schematic illustration of melting phenomenon:
(a) Smooth; (b) Wire stubbing.

4.2.4 Cross-sectional observation and evaluated parameters

Figure 4.8 shows a schematic diagram of cross-sectional sampling locations, with ① and ② indicating deposition starting points at 20 and 50 mm, respectively. Two cross-sections were longitudinally cut with a distance of 10 mm, and the bead width (W) and bead height (H) were measured.

Figure 4.9 shows a schematic illustration of the cutting positions for the cross-sectional observation and evaluated parameters. Three cross-sections were longitudinally cut with a distance of 20 mm, and effective width (W_E), the maximum height (H_M), the effective height (H_E), and the near net shape rate were measured. The near net shape rate is the ratio of the effective area to the deposited area, as shown in Fig. 4.9. In order to observe the penetration depth and defects, the cut samples were polished by 100, 200, 500 Silicon carbide sandpaper.

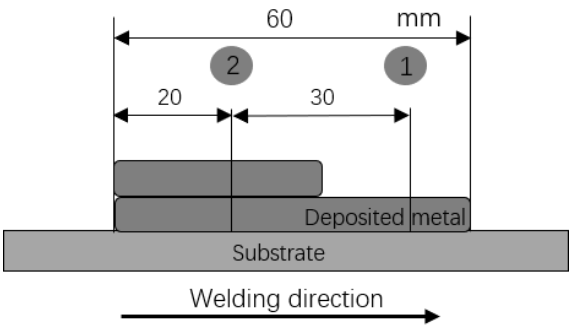

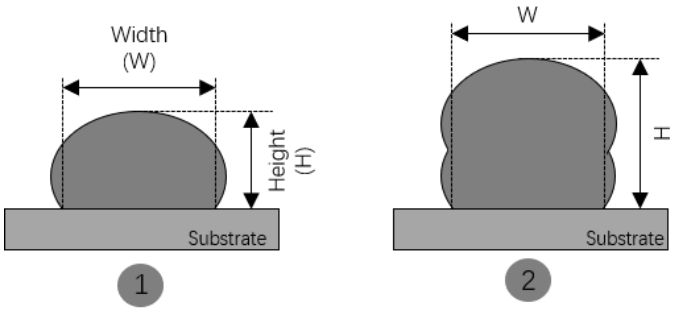

Fig. 4.8. Cutting positions for cross-sectional observation of first and second-layer and evaluated parameters.

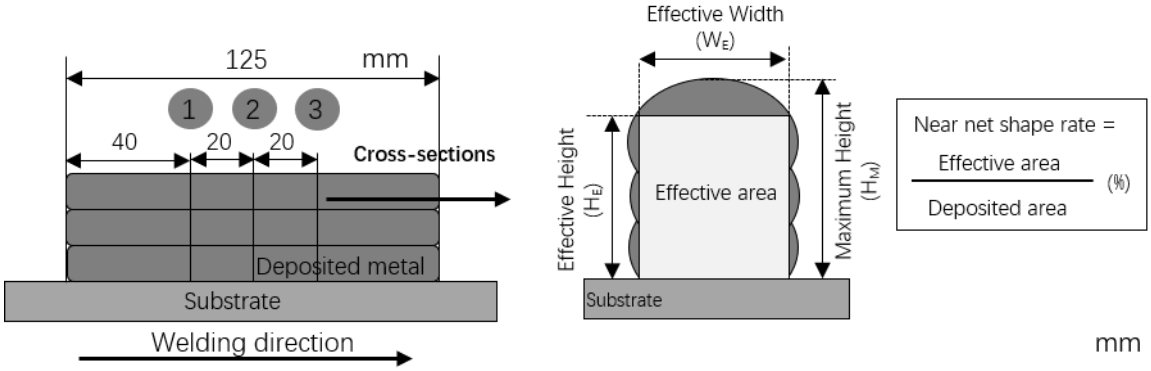

Fig. 4.9. Cutting positions for cross-sectional observation of three-layer and evaluated parameters.

4.2.5 Definition of energy heat input

The process parameters are the key to influence the quality of the deposited bead and phenomenon, namely laser power, process speed, laser spot size, and wire feeding speed. To combine these process parameters, the definition and evaluation of the energy heat input (J/mm^3) and wire feeding rate are illustrated in Equations (1) and (2).

$$\text{Energy density input} = \frac{L_P}{A_S * V_P} \tag{4.1}$$

$$\text{Wire feeding rate} = \frac{V_F}{V_P} \tag{4.2}$$

Where L_P is the laser power, in W; A_s is the area of laser spot size, in mm; V_P is the process speed, in m/min; V_F is wire feeding speed, in m/min.

4.3 Feasibility study of two-layer deposition by hot-wire laser method

4.3.1 Molten pool formation during HLAM process

A high-speed camera was used to observe the molten pool formation and hot-wire feeding during the HLAM experiments to clearly investigate the deposition process phenomena. Figure 4.10 shows the high-speed images during molten pool formation at the start region of the HLAM process using SUS308L.

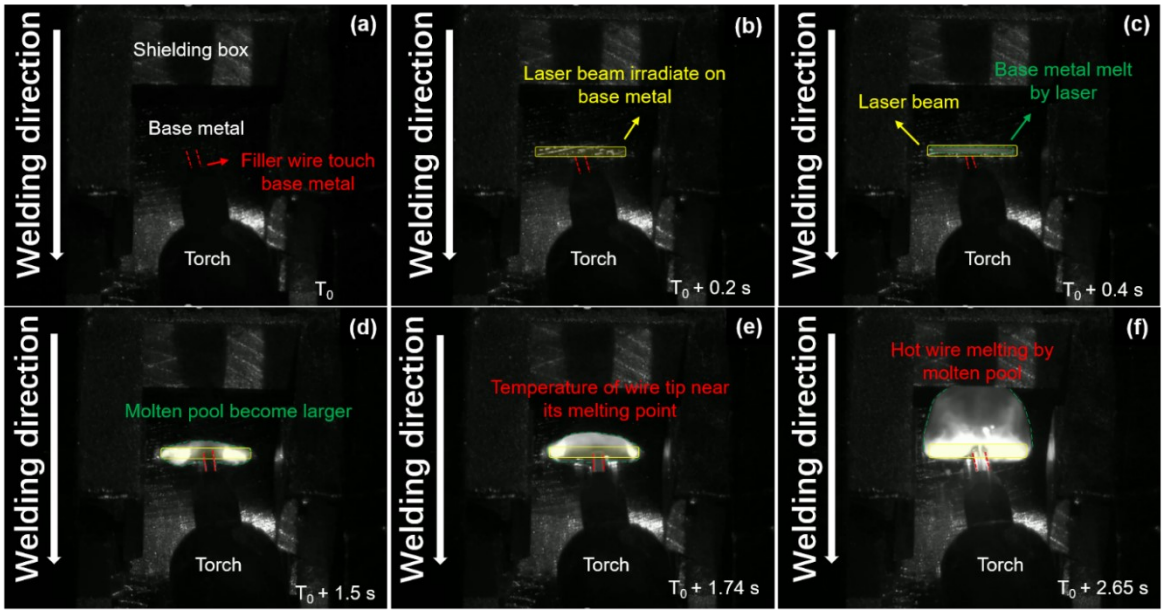

Fig. 4.10. High-speed images during molten pool formation at the HLAM process start region on SUS308L.

Before laser irradiation, the filler wire tip touched the surface of the base metal and the energization started for wire heating (Fig. 4.10a). After the laser beam began to irradiate on the base metal at a distance of 0.8 mm from the filler wire tip, the specimen on the sliding table and filler wire feed remained stationary for a short time of approximately 1 s (Fig. 4.10b). The surface of the base metal gradually melted by the laser irradiation, and a small molten pool formed (Fig. 4.10c). As time progressed, the size of the molten pool gradually increased and stabilized owing to the large-sized beam spot with low energy density, and the filler wire was not fully heated by Joule heat (Fig. 4.10d). After the wire feeding gradually started, the wire tip temperature reached its melting point by pre-Joule heating during the stationary term and heat input from the laser irradiation. The hot wire tip started melting at the edge of the laser spot and the molten pool gradually increased (Fig. 4.10e). Upon moving the table, the hot wire was steadily fed into the molten pool and fully melted. After the above beginning process period, the specimen on the slide table started to gradually

move and the filler wire feeding speed and wire current increased linearly to the appropriate condition obtained in the previous section. The molten pool grew with increasing deposition volume from the hot wire, and the molten pool rapidly cooled to form a bead (Fig. 4.10f).

4.3.2 Effect of wire feeding rate on 1st and 2nd layer

Fig. 4.11 and 4.12 show the bead appearances and cross-sections of 1st and 2nd layer when the wire feeding rate varied from 20 to 40 at a fixed process speed of 0.3 m/min and laser power of 5.5 kW. A smooth and stable bead could be obtained although the wire feeding rate changed 2 time (see Fig. 4.11). The evaluation parameters (e.g. bead width and height) of the 1st and 2nd layer cross-sections were listed in Table 4.4. As a result, the height increased with an increase in wire feeding rate since a larger amount of filler wire melted into molten pool. The bead width of all samples was around 11 mm. The height of 1st layer was from ~3.0 to ~5.5 mm and 2nd layer from ~5.4 mm to ~8.6 mm. However, a excessive wire feeding rate of 40 resulted in penetration defects in 1st layer (see Fig. 4.12c) and a swollen and rough side 2nd layer since an excessive amount of filler wire reflects the laser irradiation which cannot melt substrate fully.

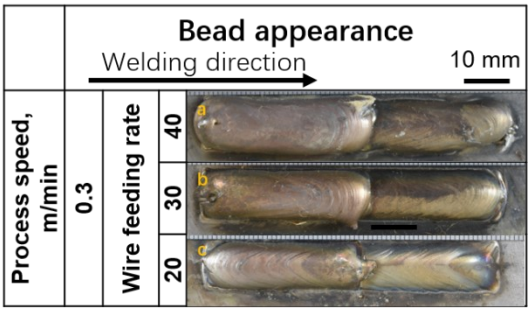

Fig. 4.11. Bead appearances.

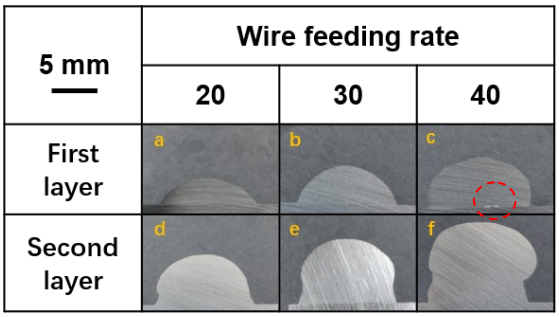

Fig. 4.12. Cross-section samples.

Table 4.4 Cross-sectional characteristics of the 1st and 2nd -layer deposition.

Materials	Wire feeding rate	First layer		Second layer	
		Width, mm	Height, mm	Width, mm	Height, mm
SUS308L	20	11.1	3.0	11.0	5.4
	30	10.9	4.1	10.8	7.1
	40	11.2	5.5	11.0	8.6

4.4 Three-layer deposition by HLAM process

4.4.1 Establishment of process parameters window of three-layer

Figure 4.13 shows the process windows of bead appearance evaluation under process parameter combinations of (a) laser power and process speed, and (b) laser power and the wire feeding rate. The red circles indicate the sound bead, and the black crosses indicate a bead with the typical defect of bead appearance. As shown in Figure 4.13a, when the wire feeding rate was fixed at 20, the lowest laser power limit existed for each process speed. As the process speed increased, a higher laser power was required to obtain the sound bead. The laser power should be combined with the appropriate process speed to achieve sufficient heat input for the sound and stable processing phenomena. When the process conditions were unsuitable, for example, the laser power was too low or the process speed was too high, and the inadequate lower heat input led to un-stable processing phenomena and poor-quality beads. As shown in Figure 4.13b, when the process speed (V_P) was fixed at 0.3 m/min, each wire feeding rate of the filler materials had laser power limitations to obtain sound bead appearances. A high and wide range of wire feeding rates (WFR) from 20 to 40 was achieved for a 6-kW laser power by using HLAM.

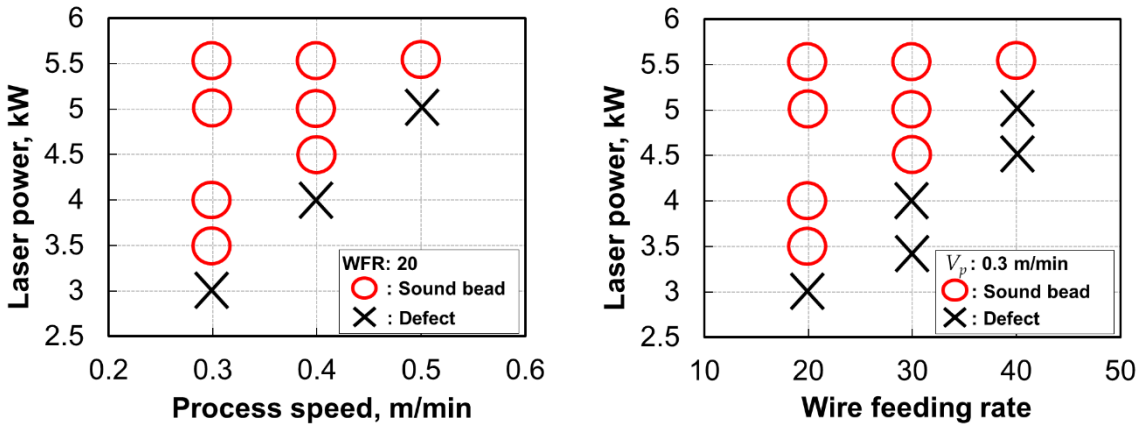

(a) (b)

Fig. 4.13. Process windows of three-layer bead appearance evaluation for process parameter combinations of
(a) Laser power and process speed and (b) Laser power and wire feeding rate.

4.4.2 Effects of process parameters on melting phenomenon

4.4.2.1 Effect of process speed and laser power

Figure 4.14 shows high-speed images during processing for various combinations of process speed and laser power using a fixed wire feeding rate of 20. Figure 4.14a shows that when the process speed (V_P) was 0.3 m/min and the laser power (L_P) was 4 kW for a fixed wire feeding rate (WFR) of 20, the filler wire was fed smoothly and continuously at the centers of the laser beam spot and molten pool front in the width direction during deposition. The same wire feeding and melting phenomena were observed at high-er process speeds of 0.4 and 0.5 m/min when a higher laser power from 4.4 to 5.5 kW was applied, as shown in Fig. 4.14c. These smooth and stable melting phenomena yielded smooth and sound bead appearances. When a higher process speed of 0.4 m/min was applied for a fixed laser power of 4 kW, the filler wire was not fed smoothly and stably into the molten pool, and it protruded from the molten pool as shown in Fig. 4.14b. The same tendency was observed at other process speeds of 0.3 and 0.5 m/min when a laser power of 3 and 5 kW was applied, respectively, as shown in Fig. 4.14d. Low-quality three-layer deposition with unmelted protruded wires at the bead sides was observed, as shown in Fig. 4.14b,d.

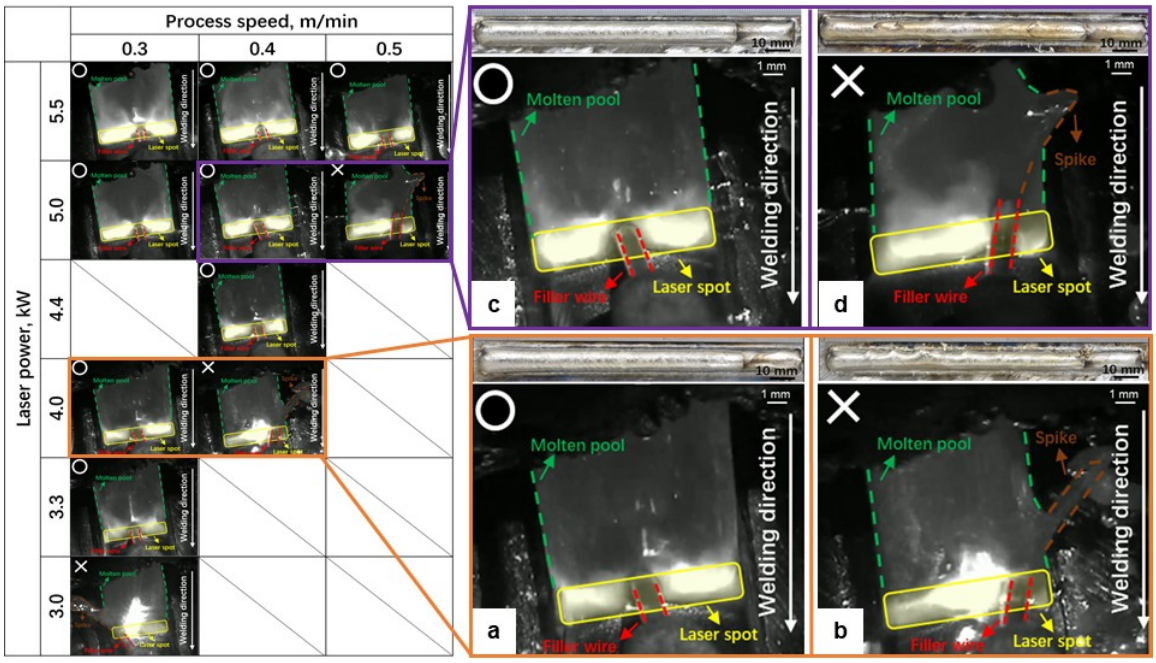

Fig. 4.14. The phenomenon of deposition for varied as process speed and laser power: (a) L_P = 4.0 kW, V_P = 0.3 m/min; (b) L_P = 4.0 kW, V_P = 0.4 m/min; (c) L_P = 5.0 kW, V_P = 0.4 m/min; (d) L_P = 5.0 kW, V_P = 0.5 m/min.

4.4.2.2 Effect of wire feeding rate and laser power

Figure 4.15 shows high-speed images during processing for various combinations of wire feeding rates and laser power using a fixed process speed of 0.3 m/min. Figure 4.15a shows that when the WFR is 30 and the laser power (L_P) is 5 kW at a fixed process speed of 0.3 m/min, the filler wire is fed smoothly and continuously at the center of the laser beam spot and molten pool front in the width direction during deposition. The same smooth and stable processing phenomena were observed at other wire feeding rates of 20 and 40 with appropriate laser powers, as shown in Fig. 4.15a. When a larger wire feeding rate of 40 was used at a fixed laser power of 5 kW, the filler wire was not fed smoothly and stably into the molten pool, and it protruded from the molten pool, as shown in Fig. 4.15d. The same tendency was observed at other wire feeding rates of 20 and 30 m/min when a lower laser power was applied, as shown in Fig. 4.15b. Almost the same processing phenomena and bead creations were observed for both combinations of laser power and process speed for a fixed wire feeding speed and laser power and wire feeding rate at a fixed process speed.

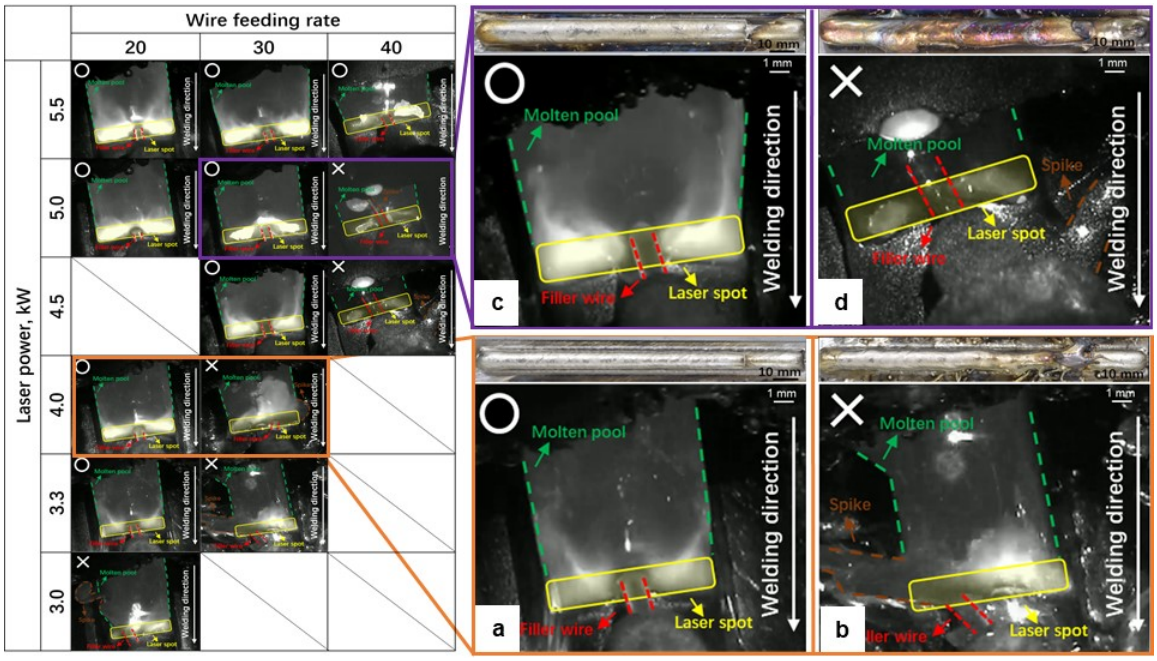

Fig. 4.15. The phenomenon of deposition for varied as wire feeding rate and laser power: (a) L_P = 3.3 kW, WFR = 20; (b) L_P = 3.3 kW, WFR = 30; (c) L_P = 4.5 kW, WFR = 30; (d) L_P = 4.5 kW, WFR = 40.

4.4.3 The map illustrating the three-layer deposition for varied energy heat input and wire feeding rate

Fig. 4.16 shows the map illustrating the three-layer deposition for varied energy heat input (Y-axis) and wire feeding rate (X-axis). In this map, the process conditions (laser power, process speed, and laser spot size) will be represented by energy density input. It is observed that the wire feeding rate has a limited energy heating input at various process speeds. The wire stubbing area increases with the increase of the wire feeding rate and decreases with the increase of energy heat input. When the wire feeding rate of 30, the energy heat input is 46 J/mm^3, the wire stubbing was observed. Increase the energy heat input to the 51 J/mm^3, the sound bead with no defects was observed. This confirms the fact that the defects could be eliminated by either increasing the energy heat input or decreasing the wire feeding rate.

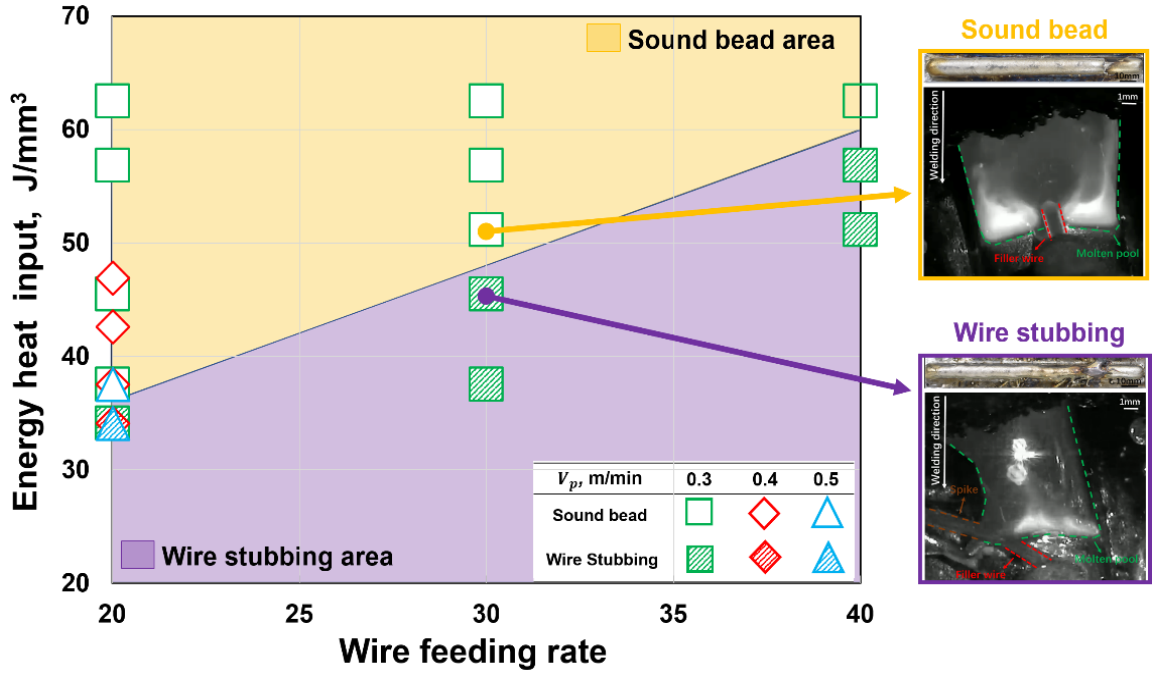

Fig. 4.16. The map illustrating the three-layer deposition of SUS308L.

4.4.4 Effect of rectangular laser beam with varied laser spot width

Fig. 4.17 shows the effect of laser spot width on effective width and wire feeding rate when the energy heat input was fixed at 52.1 J/mm^3. The effective width increases with the laser spot width increases, as shown in Fig. 4.17a. The suitable laser spot width can be selected according to the size of the model to manufacture. Moreover, the wire feeding speed is also positively related to the laser spot width, and different wire feeding rate corresponds to the suitable laser spot width.

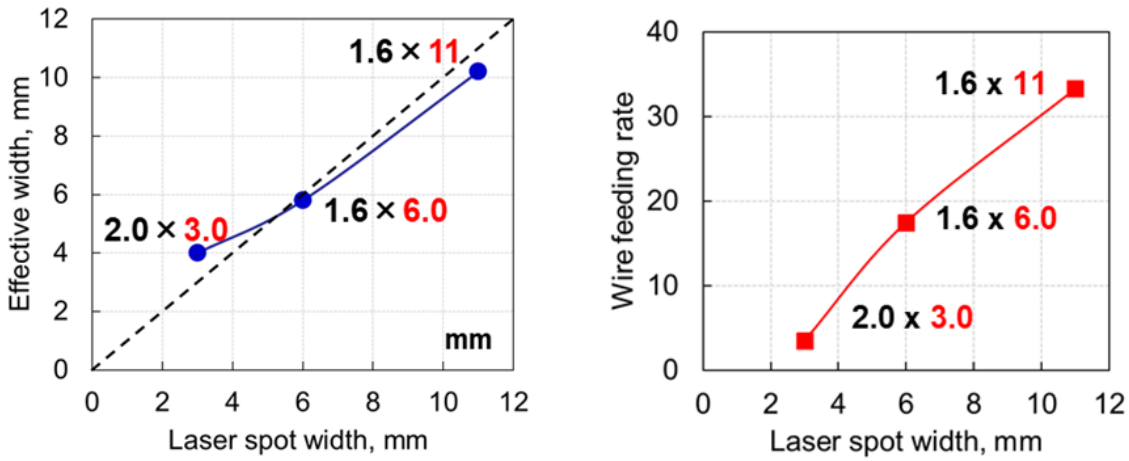

(a) (b)

Fig. 4.17. Effect of laser spot width (L_P = 5.5 kW, V_P = 0.36 m/min): (a) Effective width; (b) Wire feeding rate.

4.5 Summary

In this chapter, the process windows to obtain sound beads for various combinations of process parameters were obtained by three-layer deposition. The effect of process parameters on processing phenomena, the bead appearance, and the cross-sectional characteristics was discussed in detail by using high-speed images and cross-sectional measurements. The conclusions were as follows:

1) Process windows for a laser power from 3 to 5.5 kW, process speeds from 0.3 to 0.5 m/min, and a wire feeding rate from 20 to 40 were obtained. A large width above 10 mm and a high deposition rate above 800 cm^3/h were achieved.

2) The energy heat input was proposed as being key to obtaining adequate and stable melting phenomena. Each wire feeding rate from 20 to 40 had a lower limitation of energy heat input from 35 to 60 J/mm^3 to create sound deposited layers.

3) A sufficiently high wire feeding speed (rate) should be used according to the laser beam width and processing speed before optimizing other parameters in the proposed HLAM process.

Chapter 5

Investigation of phenomena and optimization parameters of various materials for the large-wall formation

5.1 Introduction

Nickel-based alloy was born in the 1940s. Due to its excellent mechanical properties such as structural stability, high-temperature oxidation resistance and high-temperature strength, it has gradually become the most widely used superalloy. Especially in the aerospace manufacturing industry, such as turbine blades and turbine disks. According to incomplete statistics, in the aerospace manufacturing industry, there are more than 1500 parts made of nickel-based alloys. With the promotion of the application of additive manufacturing technology in nickel-based alloys, the organization and performance of nickel-based alloy additive manufacturing components have attracted widespread attention from scholars [60,117,118].

Aluminum alloy has high specific strength, low density and good corrosion resistance. It is widely used in aerospace, rail transit, automobile manufacturing, medical equipment and other fields. In order to save energy and reduce pollution, countries all over the world are accelerating the process of lightening transportation tools. The manufacturing technology of lightweight materials represented by aluminum alloy has gradually replaced steel materials and has become the main development direction for lightweight manufacturing of vehicles and ships. The structural integration and low-cost manufacturing requirements make the development of aluminum alloy laser fuse additive manufacturing an inevitable trend [122-124].

In chapter 4, the appropriate combination of energy heat input and wire feeding rate for the SUS308L wire has been investigated. The purpose of this chapter is to obtain the optimized process parameters of three types of wires (Stainless steel, Ni-based alloy, and Al alloy). The first part is that the bead appearances and bead shape are observed to evaluate the effects of parameters on the characteristics of cross-sections such as effective width, effective height, maximum height, and near net shape rate. Then, the optimized process parameter of three types of wires (SUS308L, Inconel625, and A5356WY) for sound three-layer deposition and large wall modeling were investigated. The second part is to investigate the mechanical properties of large-wall parts of the proposed items such as tensile test and elongations compared with standard requirements.

5.2 Experiment procedure and methodology

5.2.1 Materials and specimen used

Three types of filler wires with a 1.2-mm diameter were used: SUS308L stainless steel, Inconel 625Ni-based alloy, and A5356WY Al alloy. 590 MPa-class steel plates with 12-mm thickness and 490 MPa-class steel plates with 9-mm thickness were used as a base plate for the SUS308L and Inconel625 filler wires. A5083O plates with 20-mm thickness were also used for the A5356WY filler wire. The chemical compositions of the filler wires and base metals are shown in Tables 5.1 and 5.2. The surface of the base metal was polished and cleaned using acetone to remove oxide scaling before the experiment.

Table 5.1. Chemical compositions of stainless steel and Ni-based alloy

Material	Chemical composition, mass%									
	C	Si	Mn	P	S	Ni	Cr	Mo	Nb+Ta	Fe
SUS308L	0.01	0.38	1.60	0.024	0.001	9.98	19.87	0.09	-	Bal.
Inconel625	0.02	0.09	0.01	0.003	0.001	Bal.	22.2	9.24	3.54	0.4
590 MPa-class steel	0.08	0.38	1.50	0.011	0.002	0.01	0.21	0.01	-	Bal.
490 MPa-class steel	0.15	0.45	1.52	0.007	0.002	-	-	-	-	Bal.

Table 5.2. Chemical compositions of Al alloys

Material	Chemical composition, mass%					
	Si	Mg	Mn	Cr	Zn	Al
A5356WY	0.25	4.5~5.5	0.05~0.20	0.05~0.2	0.1	Bal.
A5084O	<0.4	4.0~4.9	0.4~1.0	0.002	<0.25	Bal.

5.2.2 Process conditions

In this experiment, the three-layer deposition of SUS308L, Inconel625, and A5356WY wires were investigated. The schematic illustration of three-layer deposition and evaluated parameters was shown in Fig. 4.9. All of the equipment such as a laser

power source, hot-wire machine, a high-speed monitoring system, and so on follows in Chapter 4, as shown in Fig. 4.1.

Table 5.3 shows the range of process parameters selected for the three wires HLAM experiment. The wider and narrow (1.6 × 11 mm) rectangular laser spot with a 5° laser irradiation angle of the laser beam was applied. The combination of a 400-mm collimator, LL-line2.85 homogenizer, 400-μm core and 400-mm focusing lens creates the rectangular laser beam having the 11-mm length and 1.6-mm width at a just focus. The process parameters, such as laser power, process speed, wire current, and wire feeding rate (wire feeding speed/process speed) were varied respectively during the multi-layer deposition. The forward welding direction and the angle between the substrate and the filler wire of 45° were used. The high-purity argon gas was used for shielding the molten pool and prevent oxidation with a shielding box at a flow rate of 30 L/min.

Table 5.3. Process conditions.

Material	SUS308L	Inconel625	A5356WY
Core, μm	400		
Homogenizer	LL-line2.85		
Focus lens, mm	400		
Collimator, mm	f100		
Laser power, kW	5.0 ~ 6.0		
Defocus length, mm	0 (Just focus)		
Laser spot size, mm x mm	1.6^{W} x 11^{L}		
Welding direction	Forward (laser leading)		
Power supply distance, mm	50		
Process speed (V_P), m/min	0.24 ~ 0.6		
Wire feeding speed (V_F), m/min	6 ~ 20		
Wire feeding rate, (V_F / V_P)	20 ~ 40		
Wire current, A	123 ~ 172	164 ~ 202	212 ~ 268
Wire feeding angle, degree	45		
Wire feeding position, mm	0.8		
Shielding gas (Ar), L/min	30		

5.3 Three types of wires deposition using the hot-wire laser method

5.3.1 Effect of process parameters on cross-sectional characteristics

5.3.1.1 Laser power

Figure 5.1a shows the bead appearances and cross-sections of SUS308L filler wire when the laser power varied from 3.3 to 5.5 kW, and two types of wire feeding rates of 20 and 30 were used at a fixed process speed of 0.3 m/min. Figure 5.1b shows the bead appearances and cross-sections of Inconel625 filler wire when the laser power varied from 5 to 6 kW, and two types of wire feeding rates of 30 and 40 were

used at a fixed process speed of 0.5 m/min. Figure 5.1c shows the bead appearances and cross-sections of A5356WY filler wire when the laser power varied from 5 to 6 kW were used at a fixed process speed of 0.5 m/min and a fixed wire feeding rate of 30. It could be concluded from Fig. 5.1a and Fig. 5.1b that although the laser power was varied extensively, and the wire feeding rate changed with a 1.5 time, smooth and stable bead appearances, and sound cross-sections without any defects resulted on all deposited samples. A smaller wire feeding rate of 20 resulted in a narrower bead with increased layers, and a larger laser power resulted in a wider bead with an increase in layers for a larger wire feeding rate of 30 and 40. As for A5356WY filler wire, the higher laser power of 6 kW could not perfectly fabricate a uniform bead shape since the higher heat input cause the previous layer to remelt a lot, which resulted in larger width and the lower height of the next deposited metal or even collapses, as shown in Fig. 5.1c.

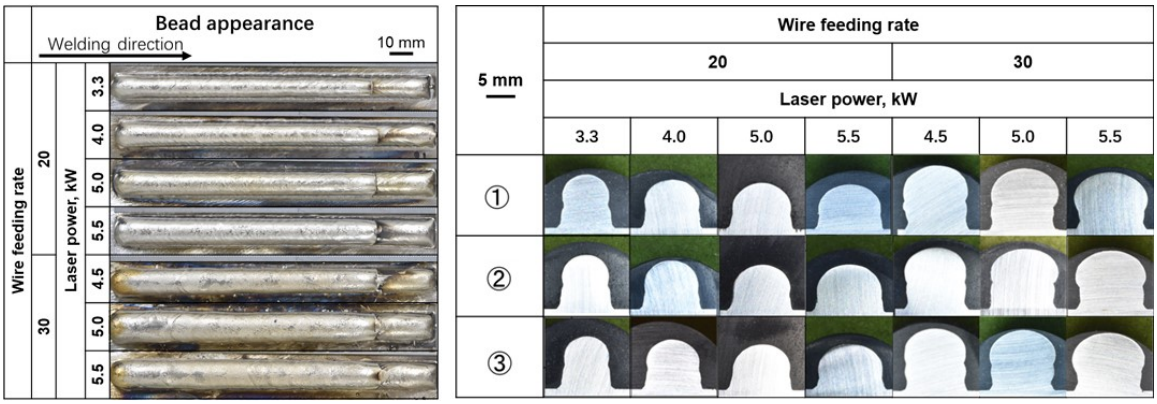

(a)

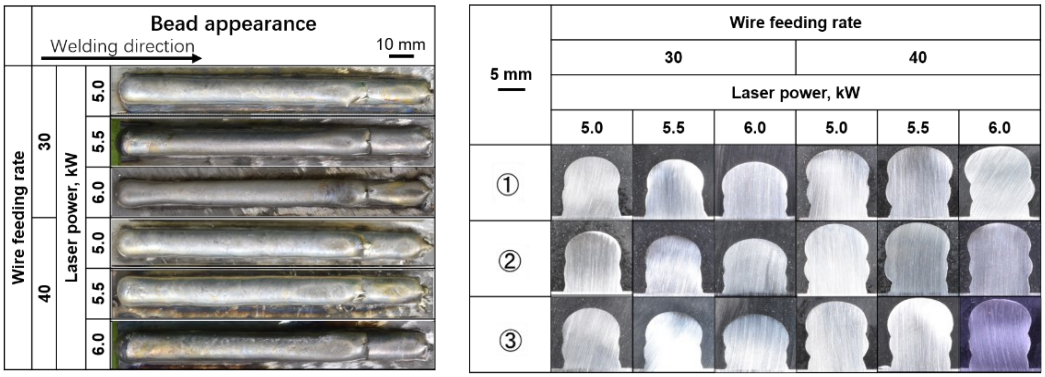

(b)

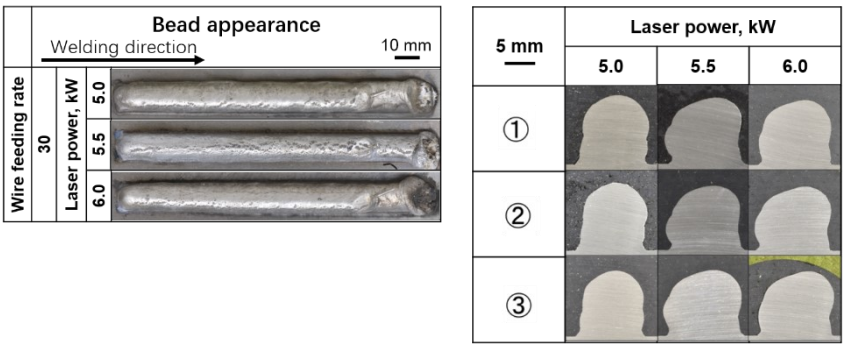

(c)

Fig. 5.1. Bead appearances and cross-sections of various laser power:
(a) SUS308L; (b) Inconel625; (c) A5356WY.

Figure 5.2 shows the effective width, the effective height and maximum height, and the near net shape rate measured on the cross-sections in Fig. 5.1. The effective width of SUS308L filler wire increased almost linearly with an increase in laser power for wire feeding rates of 20 and 30 (see in Fig. 5.2a). Figure 5.1a shows that the higher laser power yielded a wider substrate surface melting width and maintained a wider width on the third layer. The effect of wire feeding rates of 20 and 30 was large compared with the effect of laser power at both heights. The effective height and maximum height decreased almost linearly with an increase in laser power for wire feeding rates of 20 and 30. Figure 5.1a shows that an increase in width resulted in a decrease in height for a fixed wire feeding rate. The near net shape rate decreased with an increase in laser power, and it increased at the high laser power condition of 5.5 kW for both wire feeding rates of 20 and 30.

The effective width of Inconel625 filler wire increased with an increase, and the effective height and maximum height decreased with an increase in laser power for wire feeding rate of 30 (see in Fig. 5.2b). When the wire feeding rate of 40, the effective width, effective height and maximum height does not change significantly since large volume of filler material has a limitation of a wider width of the substrate, second and third layer, even with increased laser power (see in Fig. 5.1b). The near net shape rate increased with an increase in laser power for wire feeding rates of 30 and 40. The effect of wire feeding rates of 30 and 40 was large compared with the effect of laser power at near net shape rate.

In A5356WY filler wire, the effective width and near net shape rate increased first and decreased with an increase in laser power for wire feeding rate of 30 (see in Fig. 5.2c). The effective height and maximum height decreased with an increase in laser power for wire feeding rate of 30. Figure 5.1c shows that large laser power caused a uniform second and third deposited layer.

It can be conclude that the effect of wire feeding rates of 20, 30 and 40 was small compared with the effect of laser power on the effective width. The effect of wire feeding rate of 20, 30, and 40 was large compared with the effect of laser power at both heights and near net shape rate. In SUS308L filler wire, the combination of a 5.5-kW laser power and a wire feeding rate of 30 for the fixed 0.3 m/min process speed

achieved an effective width above 10 mm, an effective height above 7 mm, and a near net shape rate of over 75%. In Inconle625 filler wire, the combination of a 6-kW laser power and a wire feeding rate of 40 for the fixed 0.5 m/min process speed achieved an effective width above 11 mm, an effective height above 10 mm, and a near net shape rate of over 80%. In A5356WY filler wire, the combination of a 5-kW laser power and a wire feeding rate of 30 for the fixed 0.5 m/min process speed achieved an effective width above 9 mm, an effective height above 6 mm, and a near net shape rate of over 60%.

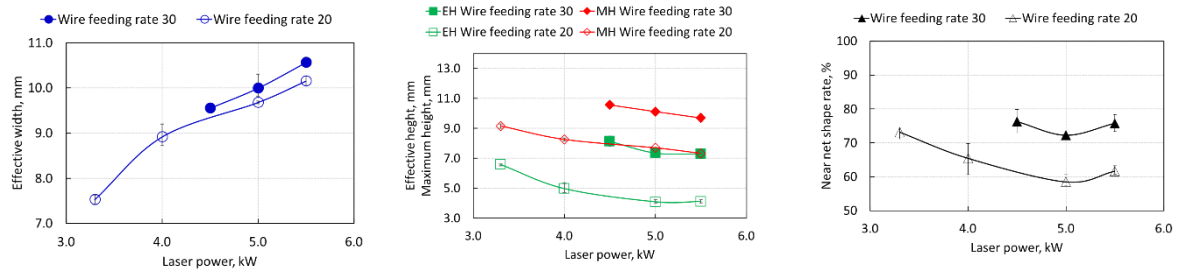

(a)

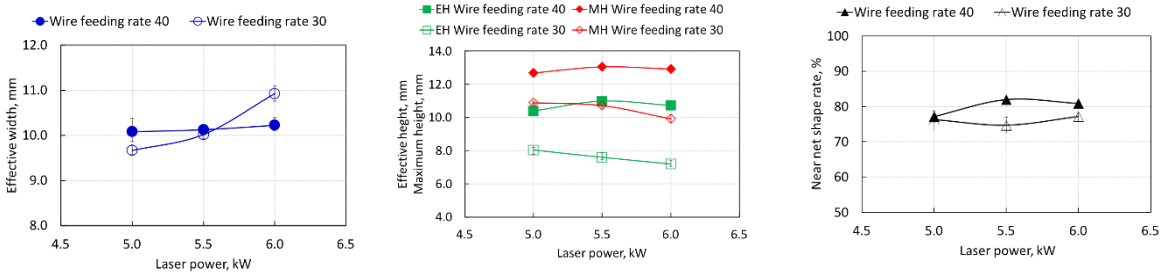

(b)

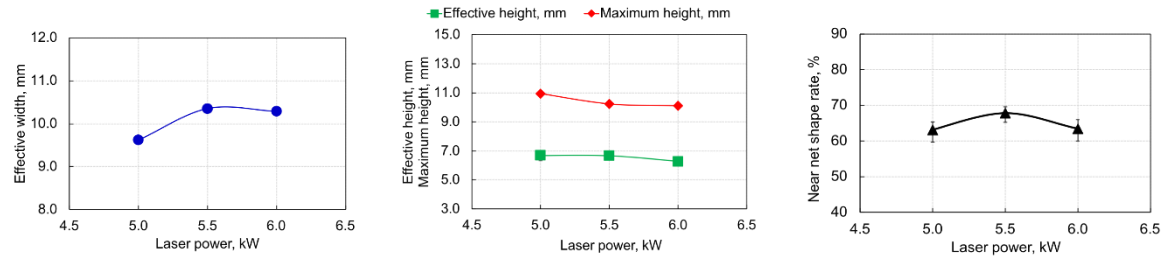

(c)

Fig. 5.2. Cross-sectional characteristics of three types of wires:
(a) SUS308L; (b) Inconel625; (c) A5356WY.

5.3.1.2 Process speed

Figure 5.3a shows the bead appearances and cross-sections of SUS308L filler wire for a varied process speed from 0.24 to 0.5 m/min, and two types of wire feeding rates of 20 and 30 at a fixed laser power of 5.5 kW. Figure 5.3b and Figure 5.3c show the bead appearances and cross-sections of Inconel625 and A5356WY filler wire when the process speed varied from 0.4 to 0.6 m/min were used at a fixed laser power of 6 kW and a fixed wire feeding rate of 30. Although the process speed varied extensively and the wire feeding rate also changed, a smooth and stable bead appearance and sound cross-sections without any defects were visible on all deposited samples. For the 20 wire feeding rates, a smaller height formed under the lower-speed condition, and a narrower width resulted for the larger speed condition. The difference in shape of deposited layer on the wire feeding rate of 30 was smaller than for the wire feeding rate of 20 (see in Fig. 5.3a).

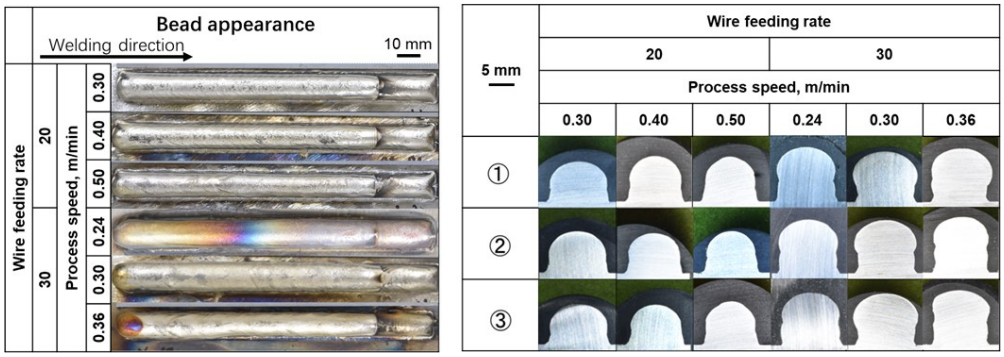

(a)

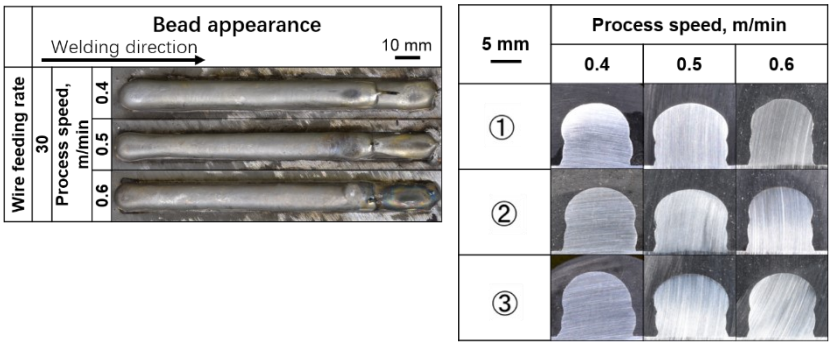

(b)

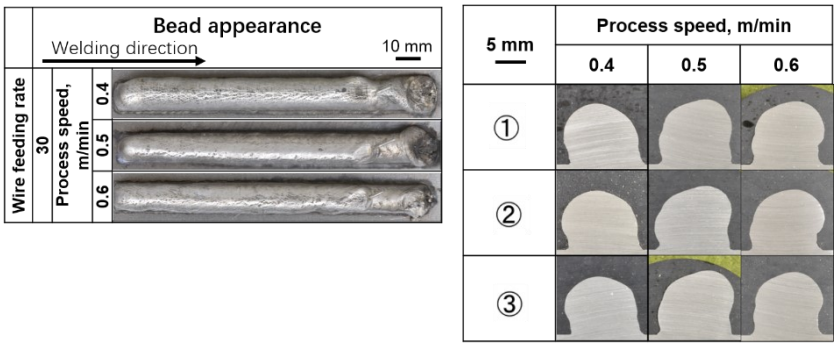

(c)

Fig. 5.3. Bead appearances and cross-sections of various process speed:
(a) SUS308L; (b) Inconel625; (c) A5356WY.

Figure 5.4 shows the effective width, the effective height and maximum height, and the near net shape rate measured on the cross-sections in Figure 5.3. The effective width of SUS308L filler wire (see in Fig. 5.4a) decreased almost linearly with the increase in process speed for both wire feeding speeds of 20 and 30 because the higher process speed decreased the heat input and melting width of the substrate surface. However, the effective width was saturated at ~10.5 mm in the slower process speed region because the laser beam spot with an 11-mm width was used in this study. The effective height and maximum height increased gradually with the increase in process speed for both wire feeding speeds of 20 and 30 because the width decreased for the fixed wire feeding speed. Height saturation occurred in the slower process speed region for both wire feeding speeds of 20 and 30 as occurred for the effective bead width. The near net shape rate increased with an increase in process speed for both wire feeding speeds of 20 and 30.

In Incone625 filler wire, the effective width and near net shape rate increased first and decreased with an increase in process speed for wire feeding rate of 30 (see in Fig. 5.4b). The effective height and maximum height increased with an increase in process speed for wire feeding rate of 30.

In A5356WY filler wire, the effective width increased first and decreased, the effective height and near net shape rate decreased first and increased with an increase in process speed for wire feeding rate of 30 (see in Fig. 5.4c). The maximum height increased with an increase in process speed for wire feeding rate of 30. The near-net shape ratio was relatively high when a process speed of 0.4 m/min, but the larger energy heat input caused the previous layer melted and spread to the lateral of deposited layer. Thus, a relatively high near-net shape rate was obtained when a process speed of 0.6 m/min.

It can be conclude that the effect of wire feeding speeds of 20 and 30 was small compared with the effect of process speed on the effective width. The effect of wire feeding speeds of 20 and 30 was large compared with the effect of process speed on

both heights. The effect of wire feeding speeds of 20 and 30 was large compared with the effect of process speed on the near net shape rate. In SUS308L filler wire, The combination of a 0.36 m/min process speed and a 30-wire feeding rate for a fixed 5.5-kW laser power achieved an effective width above 10 mm, an effective height of ~8 mm, and a near net shape rate above 75%. In Inconle625 filler wire, the combination of a 6-kW laser power and a wire feeding rate of 30 for the fixed 0.5 m/min process speed achieved an effective width above 10 mm, an effective height above 7 mm, and a near net shape rate of over 75%. In A5356WY filler wire, the combination of a 6-kW laser power and a wire feeding rate of 30 for the fixed 0.6 m/min process speed achieved an effective width above 9 mm, an effective height above 7 mm, and a near net shape rate of over 65%.

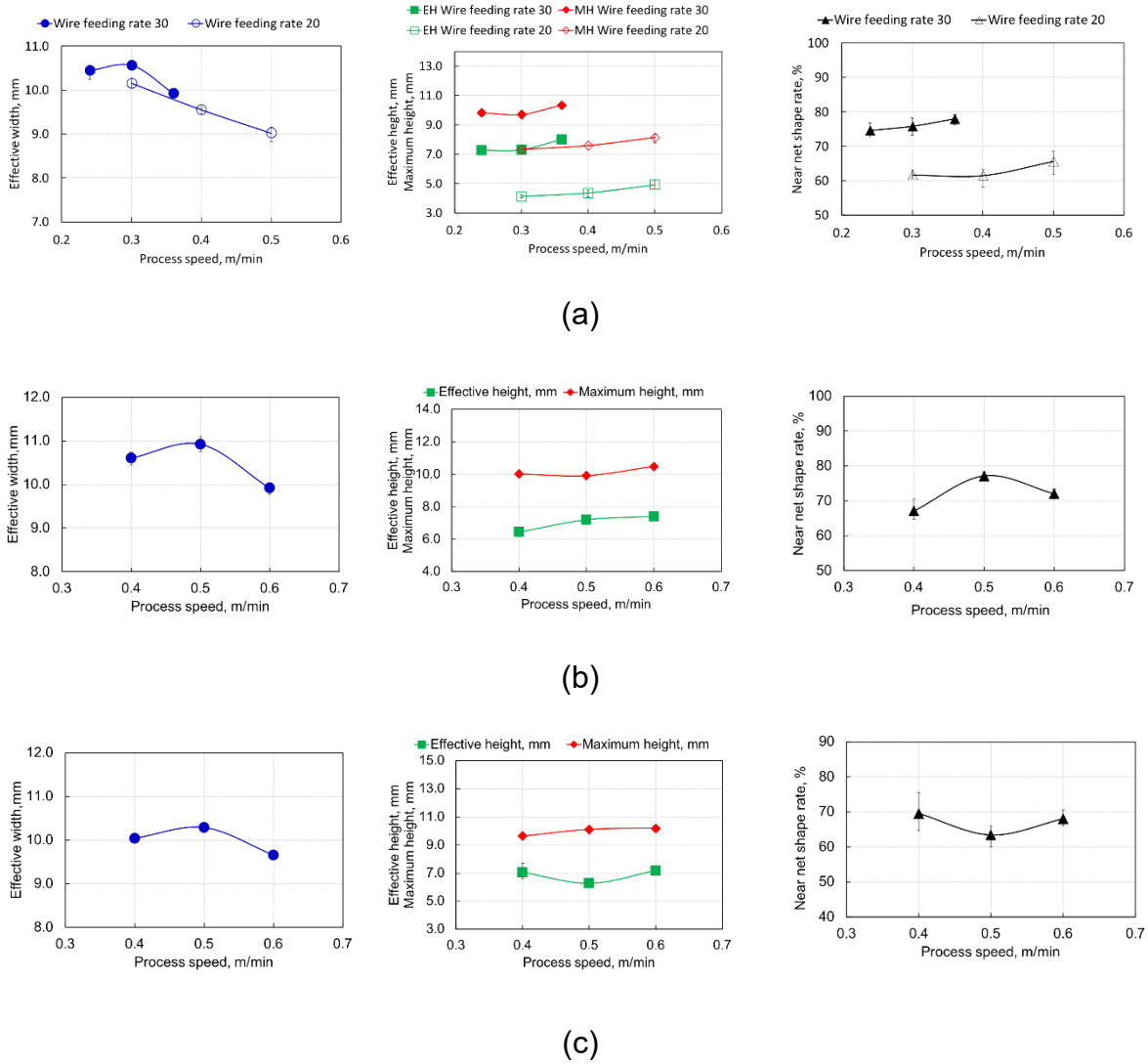

Fig. 5.4. Cross-sectional characteristics of three types of wires:
(a) SUS308L; (b) Inconel625; (c) A5356WY.

5.3.1.3 Wire feeding rate

Figure 5.5 shows the cross-sections and measured cross-sectional characteristics at various wire feeding rates of 20, 30, and 40 for the three investigated materials. The effective width, effective height, maximum height, and near-net-shape rate were measured as cross-sectional characteristics on the three cross-sections, as described in Fig. 4.9. The optimum laser power and process speed were applied for the three-layer depositions: 5 kW and 0.3 m/min for the SUS308L wire; and 6 kW and 0.5 m/min for the Inconel625 and A5356WY wires.

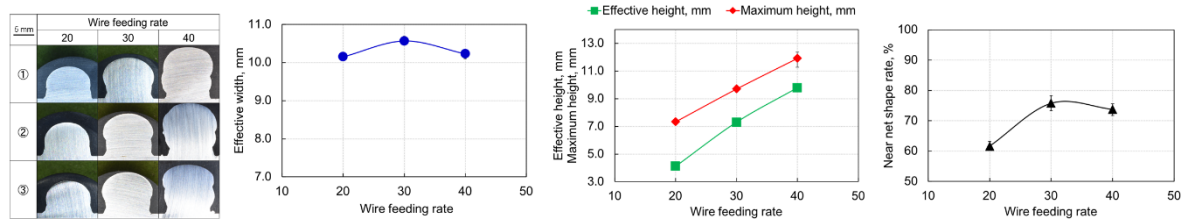

(a)

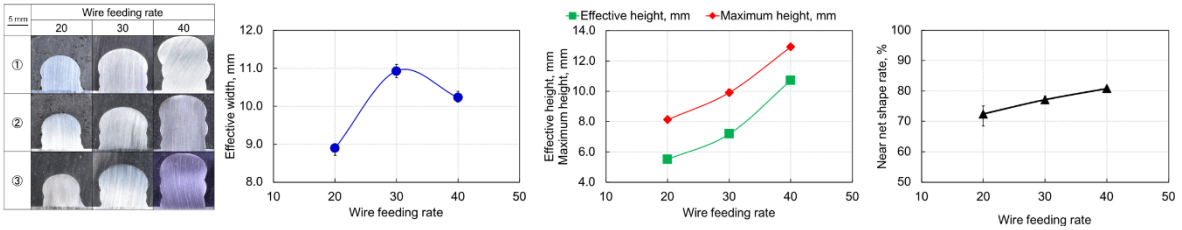

(b)

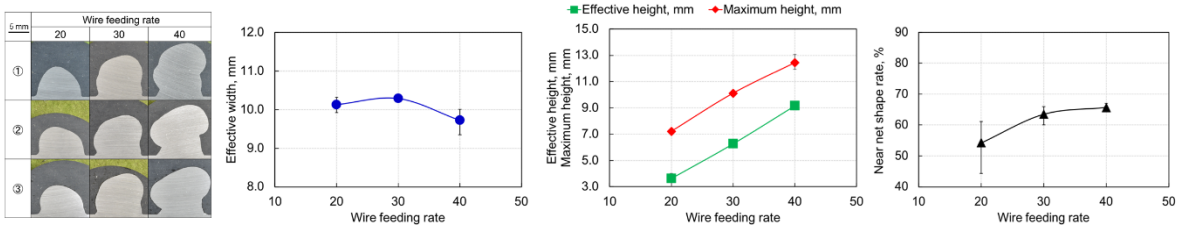

(c)

Fig. 5.5. Cross-section evaluations for wire feeding rates of 20, 30, and 40: (a) SUS308L; (b) Inconel625; (c) A5356WY.

All of the materials and conditions that formed sound and stable beads and cross-sections without any defects (e.g., imperfections, cracks) were obtained by evaluating over the three cross-sections of each specimen. The hot-wire system can provide material heated to its melting point on any wire feeding speeds without heat input from the laser irradiation by only adjusting its heating current, as shown in Fig. 3.9. The

relatively low and uniform energy density in the wide rectangle laser spot also provides uniform and stable heat input at the front of the molten pool, as shown in Fig. 4.10d. The welding condition according to the wire feeding rate was therefore not needed in the proposed process that combined the hot-wire and diode laser with a large rectangle laser spot, even if doubling the feeding rate from 20 to 40.

The effective widths of the three materials reached over 10 mm and up to 11 mm, which is almost the same as the laser spot width. The 11-mm wide-rectangle laser spot with a uniform energy distribution slightly melted the base metal surface uniformly just at the front of the molten pool. The molten pool then immediately covered the base metal surface, as shown in Fig. 4.10f. A wire feeding rate of 30 was found to create the largest effective width on all three materials. This implies that the smaller wire feeding rate of 20 could not perfectly built sufficient deposition on the laser-irradiated and slightly melted region on the base metal or previous bead surface, and parabolic shape formed with a narrow top. In contrast, the larger and excessive wire feeding rate of 40 reduced the effective width, yielding a swollen and rough side shape.

The effective height and maximum height increased almost linearly with increasing wire feeding rate for all three materials. The largest near-net-shape rate of 75% was obtained for SUS308L and 81% for Inconel625 for wire feeding rates of 30 and 40, respectively. The sufficiently effective width (>10 mm) was also obtained on both materials. However, a severely swollen and rough shape was observed for A5356WY because of its lower melting point, lower viscosity, and lower surface tension. An applied laser power of 6 kW was also too large for A5356WY under the applied process conditions.

5.3.2 Optimization of process parameters

Figure 5.6 shows the bead appearances and cross-sections when the wire feeding rate was varied at ~30 with fixed combinations of a 5.5-kW laser power and a process speed of 0.36 m/min. A smooth bead appearance and stable cross-sectional shape without defects resulted for various wire feeding rates.

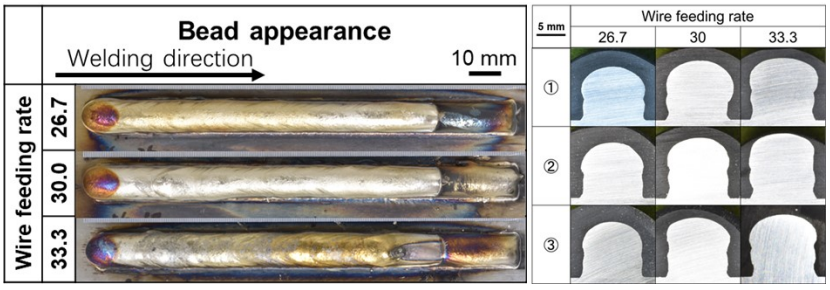

Fig. 5.6. Bead appearances and cross sections for 5.5-kW laser power and a process speed of 0.36 m/min.

Figure 5.7 shows the cross-sectional characteristics at various wire feeding rates for a fixed laser power of 5.5 kW and a process speed of 0.36 m/min. An effective

bead width of 10.2 mm with a laser spot width of 11 mm (see in Fig. 5.7a), an effective height of 8.8 mm, a maximum height of 10.9 mm (see in Fig. 5.7b), and a near net shape rate of 80% (see in Fig. 5.7c) were obtained for a wire feeding rate of 33.3. The results prove that the proposed HLAM technology can create large parts with almost 100% material utilization and a high deposition rate of 814 cm^3/h when a wire feeding rate of 33.3 and a process speed of 0.36 m/min are used.

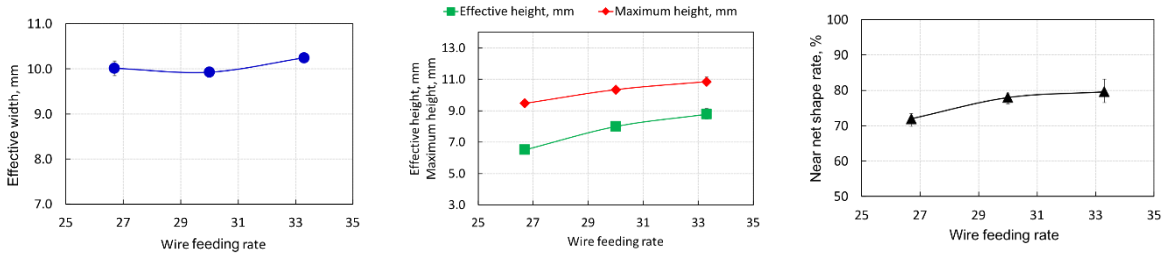

(a) (b) (c)

Fig. 5.7. Bead shape evaluation (P = 5.5 kW, V_P = 0.36 m/min):
(a) Effective width; (b) Effective height and Maximum height; (c) Near net shape rate.

The optimized three-layer deposition with both an effective width and height of approximately 10 mm (see in Fig. 5.7). A near-net-shape rate of 81% was obtained for Inconel625. In contrast, the SUS308L cross-section showed a relatively smaller effective height of 7.1 mm and smaller near-net-shape rate of 75%. The wire feeding rate, process speed, and laser power were therefore optimized based on the results, as shown in Fig. 5.7. The laser power was optimized for A5356WY because of the cross-section with a severely swollen and rough shape.

Figure 5.8 shows examples of cross-sections fabricated using the optimized process conditions listed in Table 5.4. These cross-sections were etched to confirm the base metal dilution. The effective height and near-net-shape rate of SUS308L were improved from 7.1 to 9.2 mm and from 75% to 77% using a wire feeding rate of 33.3, laser power of 5.5 kW, and process speed of 0.36 m/min. Although the near-net-shape rate was still as small as 67%, a much smoother sound shape was obtained on A5356WY by optimizing the laser power from 5.5 to 5 kW. The SUS308L and Inconel625 results also indicate that the penetration depth into the base plate was as small as 0.3 mm. This small penetration is related to the phenomenon of molten pool formation for the specific hot-wire, which is caused by the material supply just below the melting point by hot-wire feeding and the large laser beam spot with low and uniform energy density. In contrast, a relatively deep penetration is observed on the A5356WY cross-section.

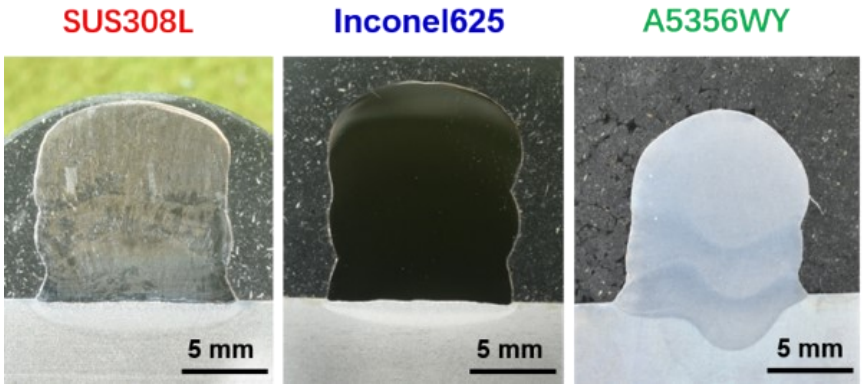

Fig. 5.8. Examples of etched cross-sections.

Table 5.4 Optimized process parameters and corresponding cross-sectional characteristics of the three-layer deposition.

Materials	Process parameters				Cross-sections characteristics			
	L_P, kW	V_P, m/min	V_F, m/min	V_F / V_P	D_P, mm	W_E, mm	H_E, mm	NNSR %
SUS308L	5.5	0.36	12	33.3	0.3	10.3	9.2	77
Inconel625	6	0.5	20	40	0.3	10.7	10.2	81
A5356WY	5	0.5	15	30	3.0	9.3	7.3	67

5.4 Large-wall parts of three type wires fabricated by using the HLAM

This section is to fabricate large-wall parts of three types wires (SUS308L, Inconel625, and A5356WY) by using the optimized process parameters, as given in Table 5.4. The three types large-wall parts were achieved in the length above 200 mm. The cross-sectional characteristics, tensile test and fracture observation were studied according to the standard specification.

5.4.1 Large wall-type sample and building path

Figure 5.9 shows a schematic illustration of the large wall-type sample and building path. Building large wall-type samples with a 250 mm length and 50 mm height was the most critical aim in the final work. In order to reduce the influence of heat accumulation, the test adopts a unidirectional scanning path for deposition, and the interlayer cooling time is 5 min.

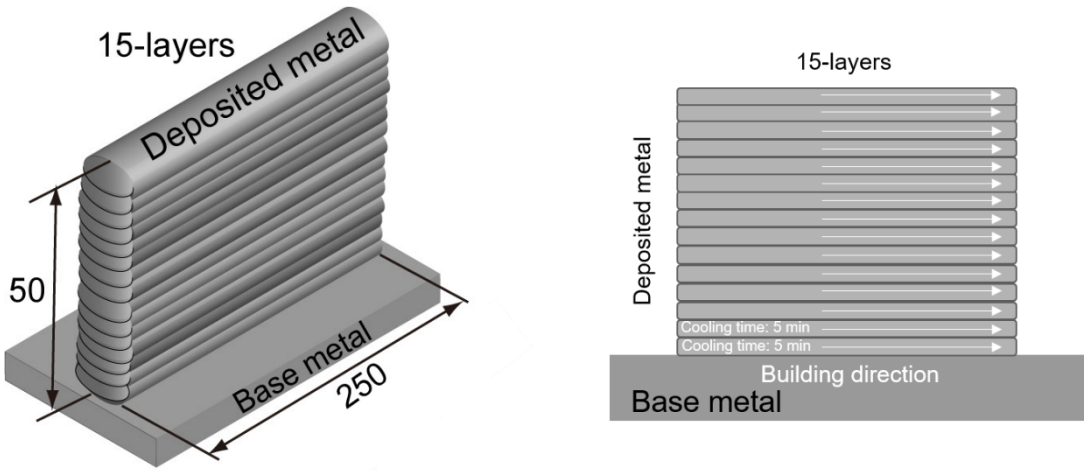

Fig. 5.9. Large wall-type sample and building path.

5.4.2 15-layer deposition

Figure 5.10 shows the appearance and cross-section of the 15-layer wall-type samples of three wires that were fabricated by using the optimized process parameters from the above investigations. Smooth and uniform appearance and a sound cross-section without any defects were obtained, although the fixed process parameters combined through all 15 layers. The effective height was from 38.6 mm to 53.6 mm, maximum height was from 42.4 mm to 59.3 mm, effective width was from 8.8 mm to 9.9 mm, and near net shape rate was from 75% to 83% were obtained by using only 15 layers.

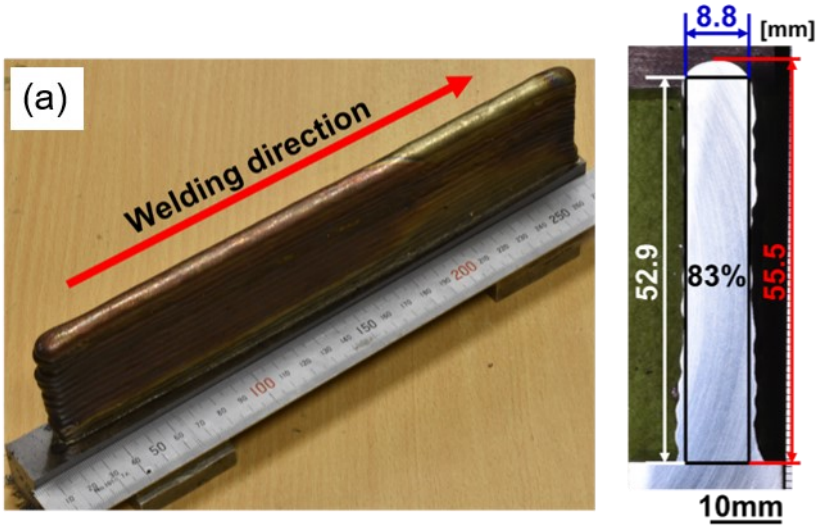

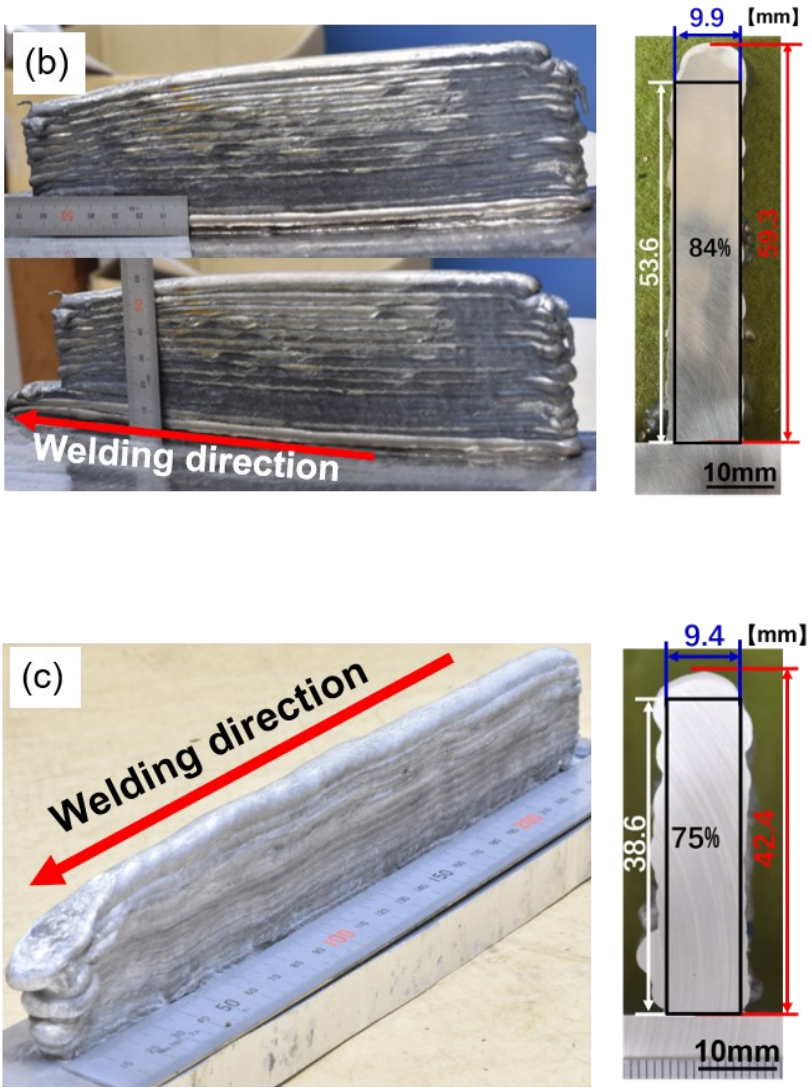

Fig. 5.10. Appearance and cross-section of 15-layer large wall-type sample with measured values of effective height, maximum height, effective width, and near net shape rate: (a) SUS308L; (b) Inconel625; (c) A5356WY.

Figure 5.11 shows the high-speed images of SUS308L that were captured on the first, fifth, tenth, and fifteenth layers during processing. The green, red, and yellow lines indicate the side shape of the molten pool, the hot-wire tip region, and the laser irradiating region, respectively. Stable molten pool formation and hot-wire feeding phenomena resulted, and almost the same phenomena were observed on all layers even when all process conditions were fixed from the first to the fifteenth layer on the substrate.

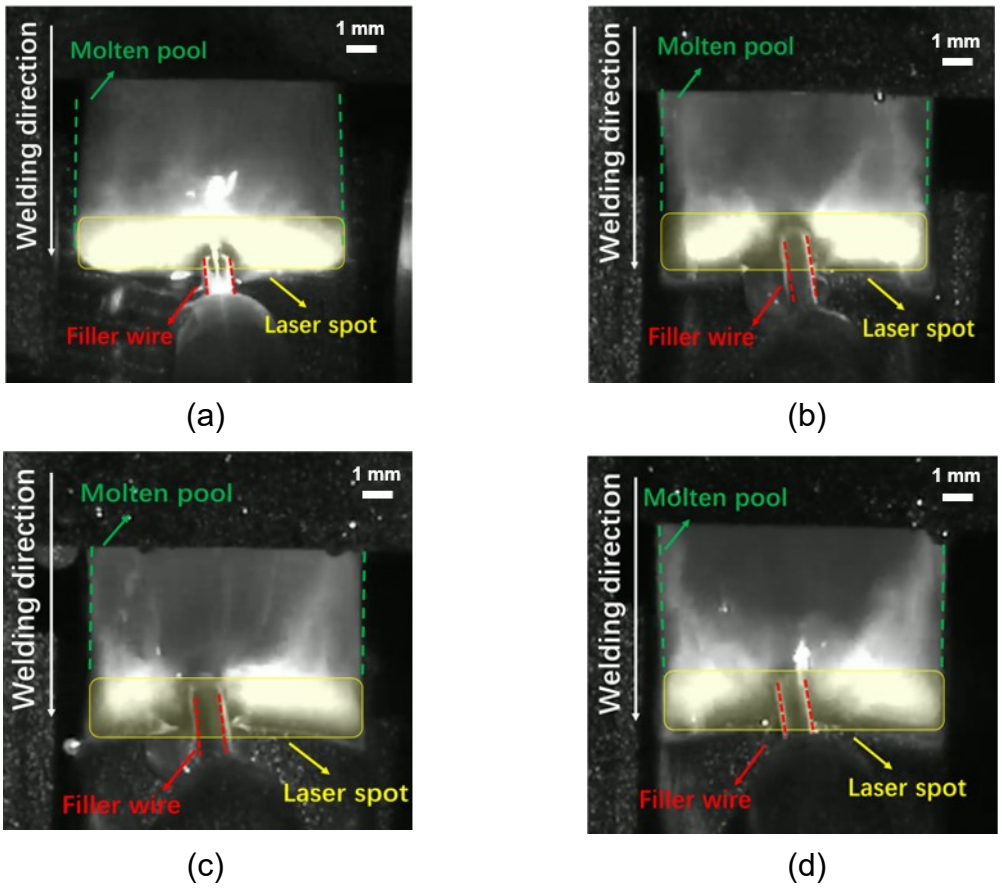

Fig. 5.11. High-speed images on (a) first, (b) fifth, (c) tenth, and (d) fifteenth layer, during 15-layer deposition.

5.5 Tensile test evaluation

Figure 5.12a shows a schematic illustration of a cut-off plan for the tensile test specimen based on JIS Z2201 No.14-B. A 200 mm tensile test piece was cut out with a position of 30 mm from the welding start point. A UH-FF1000kNI (made by Shimadzu Corporation) was used as the tensile tester. The test measures displacement by measuring the amount of displacement of the crosshead. The initial cross-sectional area of SUS308L tensile test specimen is 126 mm^2 with a thickness of 7 mm, a height of 18 mm, and a length of 200 mm (see in Fig. 5.12b). The initial cross-sectional area of Inconel625 tensile test specimen is 144 mm^2 with a thickness of 8 mm, a height of 18 mm, and a length of 200 mm (see in Fig. 5.12c). The initial cross-sectional area of A5356WY tensile test specimen is 108 mm^2 with a thickness of 6 mm, a height of 18 mm, and a length of 200 mm (see in Fig. 5.12d). For the original length, the parallel length of 80 mm was used instead of the distance between the gauge points of 60 mm. SUS308L and Inconel625 was performed at a crosshead displacement of 1 mm/min, and A5356WY was performed speed of 20 mm/min.

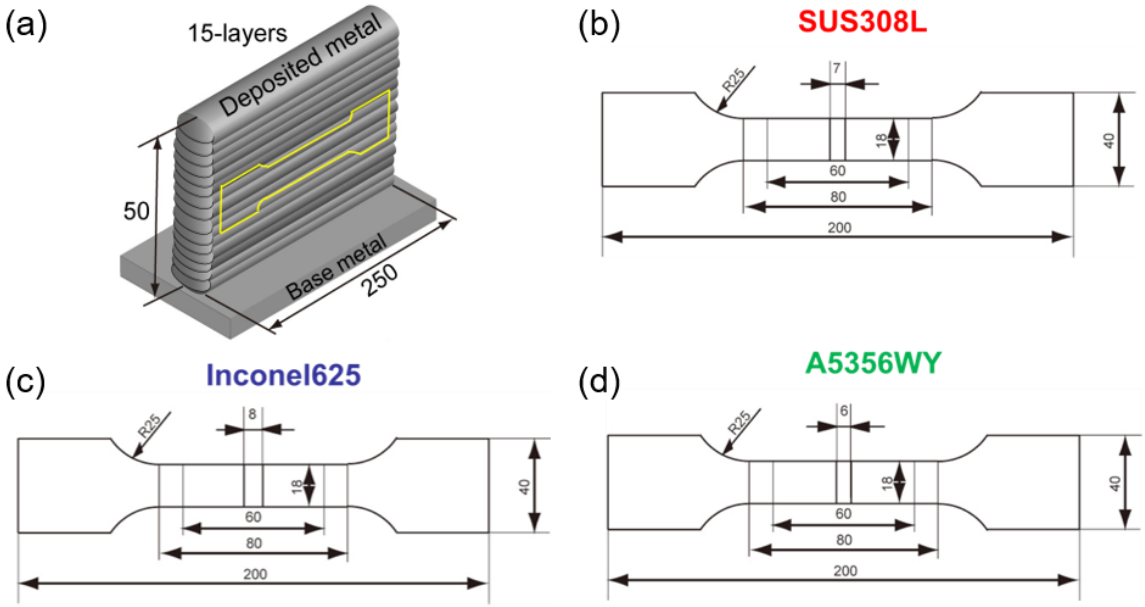

Fig. 5.12. Cut-off plan for tensile test specimen (JIS Z2201 No.14-B).

Figure 5.13 show the load–displacement and stress–strain curves of three types of wires from the tensile tests using the specimen that was cut from the fabricated 15-layer wall-type samples, as shown in Fig. 5.12. Figure 5.14 shows the tensile test results of the HLAM deposited metal. As a results, a tensile strength of 558 MPa and a 49% elongation of SUS308L were obtained (see in Fig. 5.13a). For the Inconel625 wire, a tensile strength of 713 MPa and a 66% elongation of A5356WY wire were obtained (see in Fig. 5.13b). For the A5356WY wire, a tensile strength of 265 MPa and a 23% elongation were achieved (see in Fig. 5.13c). The tensile strength and elongation of all deposited metal meet the required values of the filler material. The above results indicate that the proposed HLAM process can achieve a stable process phenomena using a simple process parameter combination and sound-deposited sample with sufficient mechanical properties without any defects.

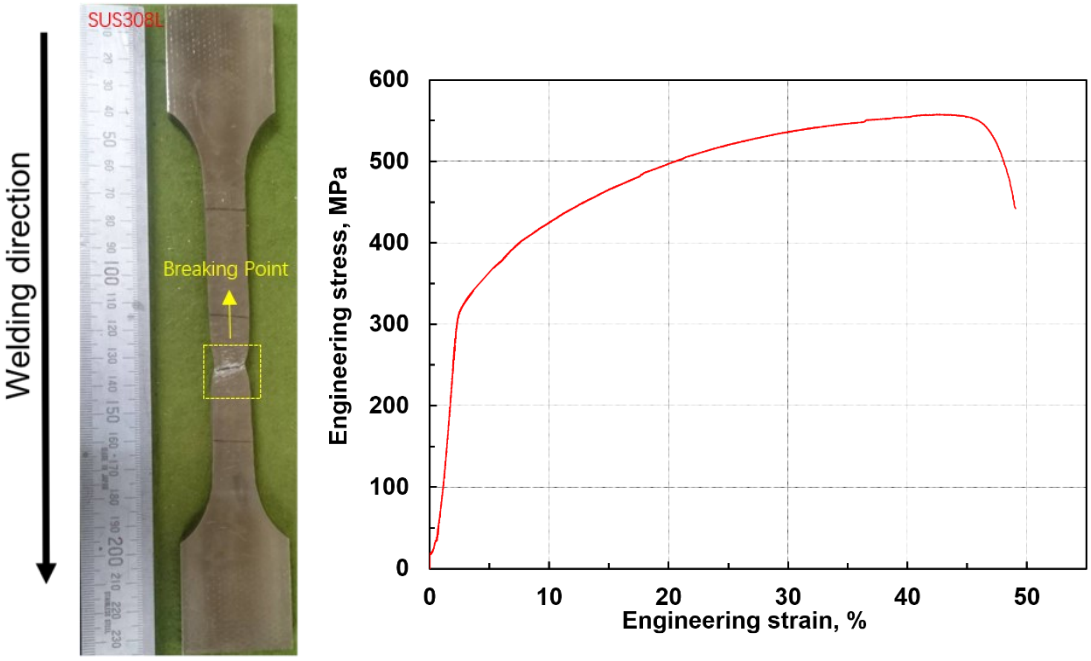
SUS308L
Welding direction
Breaking Point
Engineering stress, MPa
Engineering strain, %
0
100
200
300
400
500
600
0
10
20
30
40
50

(a)

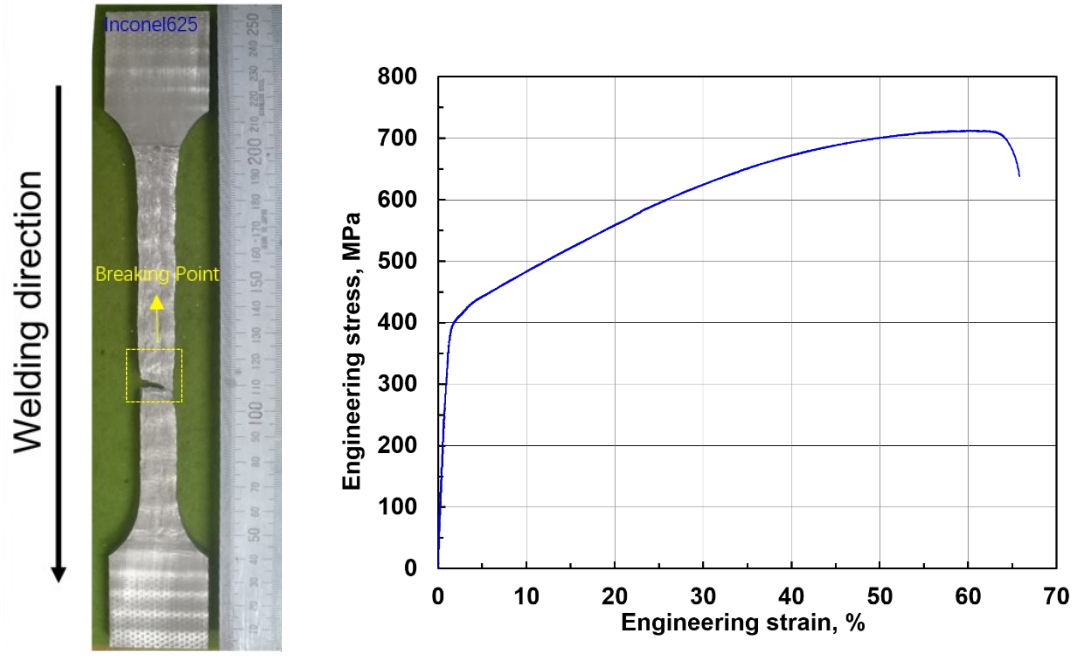
Inconel625
Welding direction
Breaking Point
Engineering stress, MPa
Engineering strain, %
0
100
200
300
400
500
600
700
800
0
10
20
30
40
50
60
70

(b)

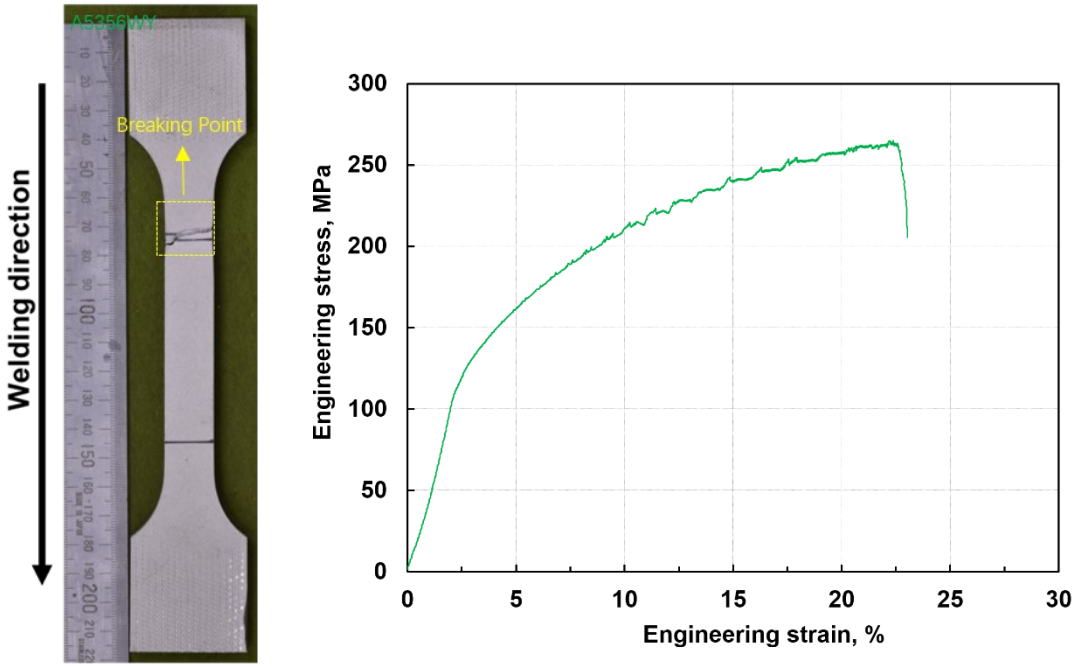

(c)

Fig. 5.13. Load–displacement and stress–strain curves of three types of wires: (a) SUS308L; (b) Inconel625; (c) A5356WY.

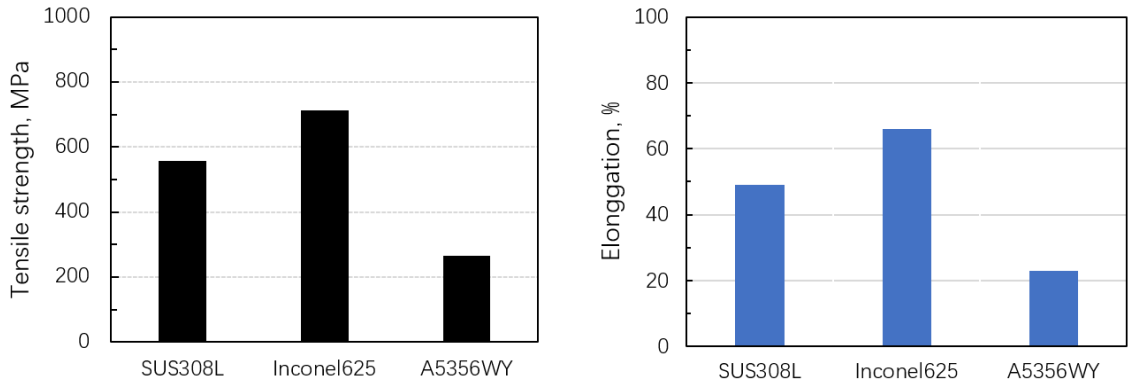

(a) (b)

Fig. 5.14. Tensile test results of 15-layer deposition samples：(a) Tensile strength; (b) Elongation.

5.6 Summary

In order to improve the proposed welding process for a practical use, the vertical hot-wire laser welding system with a self-propelled base was developed in order to do the trial for the long weld joint similar to the field welding based on the previous investigations of the optimization of welding conditions, and then the properties of the welded joint were investigated.

1) The laser power and process speed affected the effective width and effective height and maximum height, respectively. The wire feeding rate had the biggest effect on height and the near net shape rate.

2) An excessively high and low wire feeding rate resulted in a parabolic and swollen shape, respectively.

3) Sound three-layers and cross-sections without any defects were obtained for the three materials types using the optimized process parameters. A wide effective width of 9–11 mm, and a high wire feeding speed of 12–20 m/min (deposition rate of approximately 800–1300 cm^3/h) were achieved.

4) Large-wall samples for the three materials types (SUS308L, Inconel625, and A5356WY) with a maximum height of 42.4-59.3 mm and a high near net shape rate of 75-83% were obtained by using only 15 layers. Sufficient tensile strength and elongation of three materials large-wall were achieved.

Chapter 6

Optimization of process conditions in application of narrow spot beam by using SUS630 wire

6.1 Introduction

A precipitation-hardened martensitic stainless steel, i.e., 630 stainless steel (17-4 PH), is widely applied in shipbuilding, automobile and aerospace industries because of its high corrosion resistance, high strength and high wear resistance [161,162]. Many researches have dealt with the powder bed additive manufacturing, particularly powder bed fusion (PBF) and DED using 17-4 PH material [163,164]. Hu et. al [165] successful used 17-4 PH stainless steel powder to fabricate 3D parts via PBF. LeBrun et. al [166] also studied the mechanical performance at various thermal processing of tensile specimens machined from bulk 17-4 PH produced by using PBF.

The HLAM has some advantages such as low melt-back of the previous layer, high flexibility of materials choice and thermal stability. The hot-wire feeding phenomenon and quality of deposited metal have a high correlation with process conditions such as laser beam intensity, welding direction and wire feeding angle [143]. Moreover, unsuitable process conditions result in wire stubbing and wire dripping [167,168]. In Chapters 3-5, the current of filler materials could be estimated by calculation equation before deposition and a wider spot width of 11 mm with optimized parameters was achieved in SUS308L, Inconel625, and A5356WY by using HLAM. Three large wall-type parts with the effective width of ~10 mm, effective height above ~40 mm, and length above ~200 mm was fabricated. However, the thin-wall of various materials also need to apply in special industries. However, there still remains a lack of studies regarding optimized processing conditions and microstructure of 17-4 PH stainless steel by using HLAM.

In this section, a hot-wire system and high-power diode laser hybrid AM technique was investigated for the deposition of 630 stainless steel. The effect of processing conditions including the wire feeding position, defocus length and welding direction on the stability of deposition along with the effect of the energy density distribution and process speed on the neat net shape rate and microstructure of the deposited three-layer was investigated. The experimental work is assisted by the use of high-speed camera to observe the wire feeding behavior and molten pool creation. Moreover, the microstructure of the materials fabricated at difference process speed was evaluated.

6.2 Materials and methods

6.2.1. Materials and specimen used

The 630 stainless steel wire with a diameter of 1.2 mm was used as the feedstock material. The 400-MPa-Class low carbon steel plate with dimensions of 100 mm x 100 mm x 10 mm (length x width x thickness) and SUS630 stainless steel with dimensions of 100 mm x 20 mm x 10 mm (length x width x thickness) were used as the base metal. The chemical composition of the base metal and 630 stainless steel filler material are shown in Table 6.1. The surface of the cut base metal needs to be polished by abrasive paper to remove the oxides and then cleaned by acetone.

Table 6.1 Chemical compositions of base metal and filler wire

Material	Chemical composition, mass%											
	C	Si	Mn	P	S	Ni	Cr	Mo	Cu	Nb	Co	Fe
SUS630 (Wire)	0.02	0.42	0.51	0.001	0.001	4.80	16.16	0.06	3.34	0.22	-	Bal.
SUS630 (Base metal)	0.08	0.38	1.50	0.011	0.002	0.01	0.21	0.01	3.51	0.19	0.12	Bal.
400-MPa-Class low carbon steel (Base metal)	0.12	0.28	1.33	0.015	0.003	0.01	0.01	0.01	-	-	-	Bal.

6.2.2 Process conditions

The HLAM experimental system for SUS630 filler wire is composed of a laser system, a hot-wire system, a camera device and an industrial robot system, as shown in Fig. 6.1. A schematic diagram for various welding directions (laser leading and hot-wire leading) of the experimental setup is shown in Fig. 6.2.

Figure 6.3 shows the schematic illustration of bead evaluation method, the three samples were longitudinally from start with a distance of 10 mm on the deposited metal to ensure date accuracy. As the macro morphology shown that the measurement values such as near net shape rate, maximum height, effective height, and effective width) were obtained. In order to observe the effect of process speed on micro morphology, the cut samples were polished by 80, 100, 200, 500, 1200, 2000, 3000 Silicon carbide sandpaper, and polished to the mirror-like surface aspect by the diamond polishing paste. Then, all samples were ethic by the chemically rinsed for 30 s in the solution of HNO_3:HCl = 1:3 to reveal the microstructure. The micro morphology were observed by means of an optical microscopy (OM).

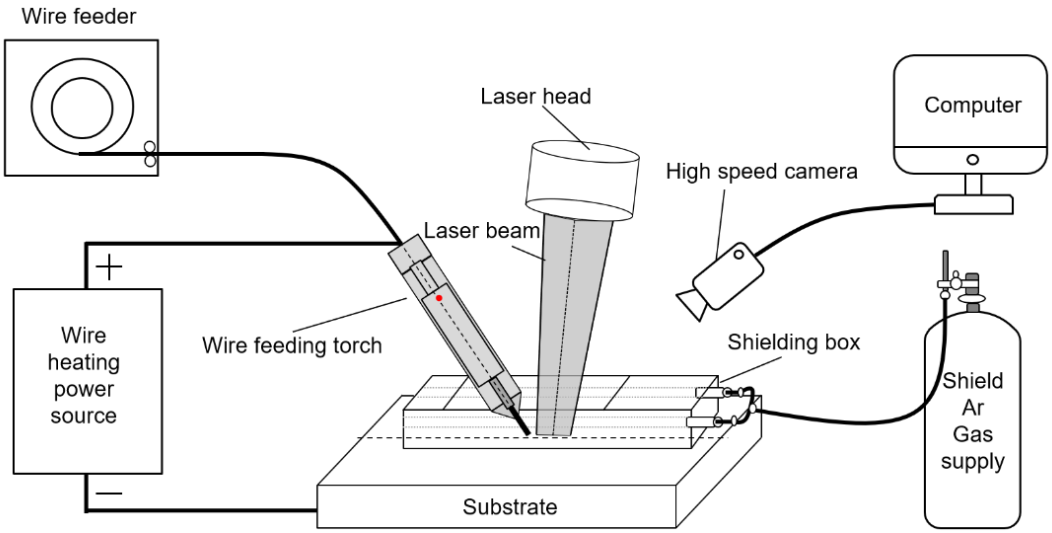

Fig. 6.1. Schematic diagram of HLAM equipment for SUS630 filler wire

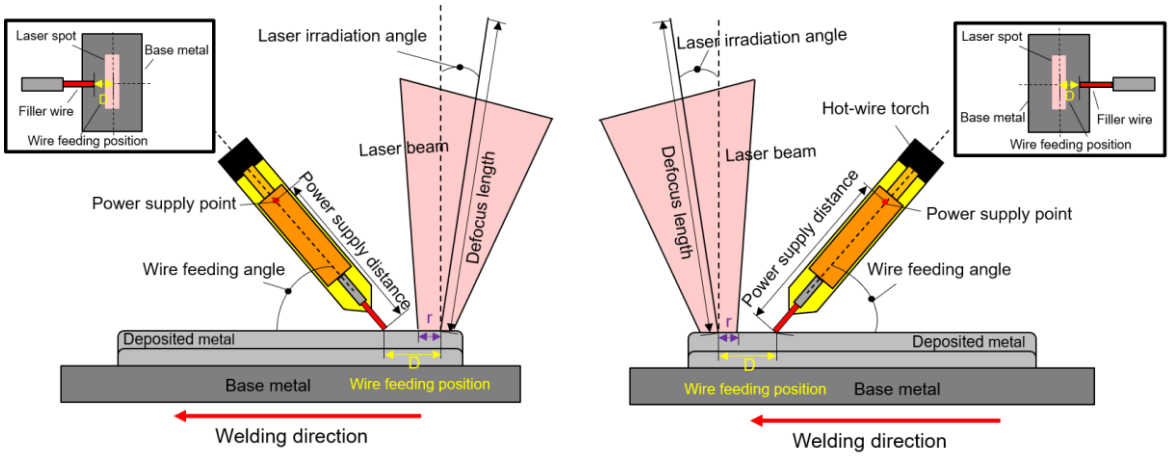

(a) (b)

Fig. 6.2. Schematic illustration for various welding directions:
(a) Forward (wire leading) and (b) Backward (laser leading).

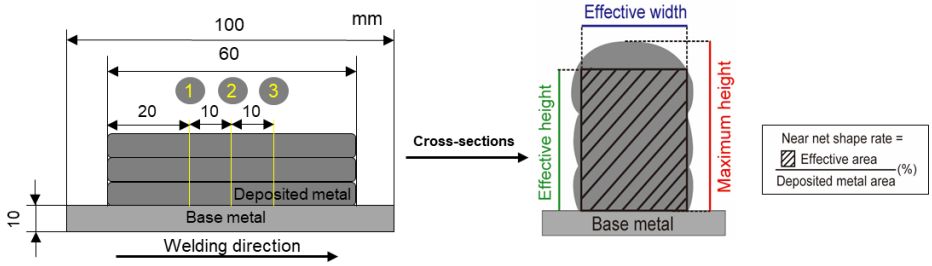

Fig. 6.3. Schematic illustration of bead evaluation.

Table 6.2 shows the process conditions used in this study. The process speed and wire feeding rate were varied as a parameter respectively. The wire feeding rate is the ratio of the wire feeding speed (V_F) and process speed (V_P). Argon was used as the shielding gas resource and shielding gas was injected at a flow rate of 30 L/min. The sizes of laser beams were measured with a beam profiler (Laser View), while the laser power was set as 2 kW. The energy density distribution was compared with that of the normal beam profile induced by various defocus lengths, as shown in Fig. 6.4.

Table 6.2 Process conditions.

Core, μm	1000		
Focus lens, mm	200		
Collimator, mm	f100		
Laser power, kW	2		
Laser irradiation angle, degree	5		
Defocus length, mm	+20	+30	+40
Laser spot size, mm	ϕ4	ϕ6	ϕ8
Welding direction	Forward (wire leading); Backward (laser leading)		
Power supply distance, mm	70		
Process speed (V_P), m/min	0.4 ~ 1.0		
Wire feeding speed (V_F), m/min	3.2 ~ 4		
Wire feeding rate, (V_F / V_P)	4 ~ 10		
Wire current, A	72 ~ 84		
Wire feeding angle, degree	75		
Wire feeding position, mm	D≤0, 0<D< r, D≥r		
Shielding gas (Ar), L/min	30		

Fig. 6.4. Energy density distribution was recorded in HLAM at defocus lengths of +20 mm, +30 mm, and +40 mm.

Defocus length, mm	+20	+30	+40
Beam profile	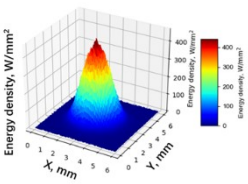	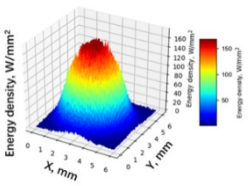	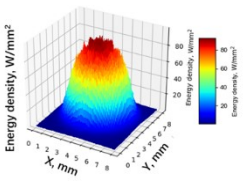
Energy density distribution	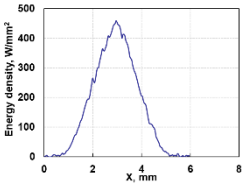	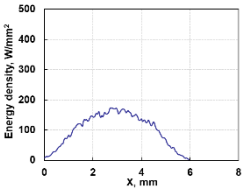	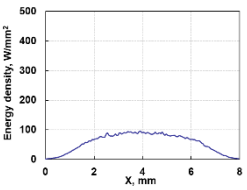

6.3 Optimization of wire feeding condition using narrow laser spot

Figure 6.5 shows the bead appearances and schematic illustrations of the wire feeding and laser irradiation. It can be considered that the positions of wire feeding and laser irradiation play an important role in bead formation during the HLAW process. Therefore, the process was conducted under three different positions.

First, the wire feeds in the middle of laser beam (D ≤ 0 mm) as shown in Fig. 6.5a. Second, the wire feeding position is between the middle and edge of laser beam in the process direction (0 < D < r mm) as shown in Fig. 6.5b. Third, the wire feeding position contacts with the edge of the laser diameter range in the process direction (D ≥ r mm) as shown in Fig. 6.5c. It was found that when the wire feeding position was set across the center of the laser beam (D ≤ 0 mm), the hot-wire was melted in advance by irradiation of the laser at an excessive height and resulted in a humped deposited metal (see in Fig. 6.5a). When the wire feeding position was placed near the boundary of the laser beam (D ≥ r mm), the un-stable bead with wire stubbing defect was presented in Fig. 6.5c. When the wire feeding position is between the middle and edge of laser beam in the process direction (0 < D < r mm), a uniform and smooth bead could be obtained.

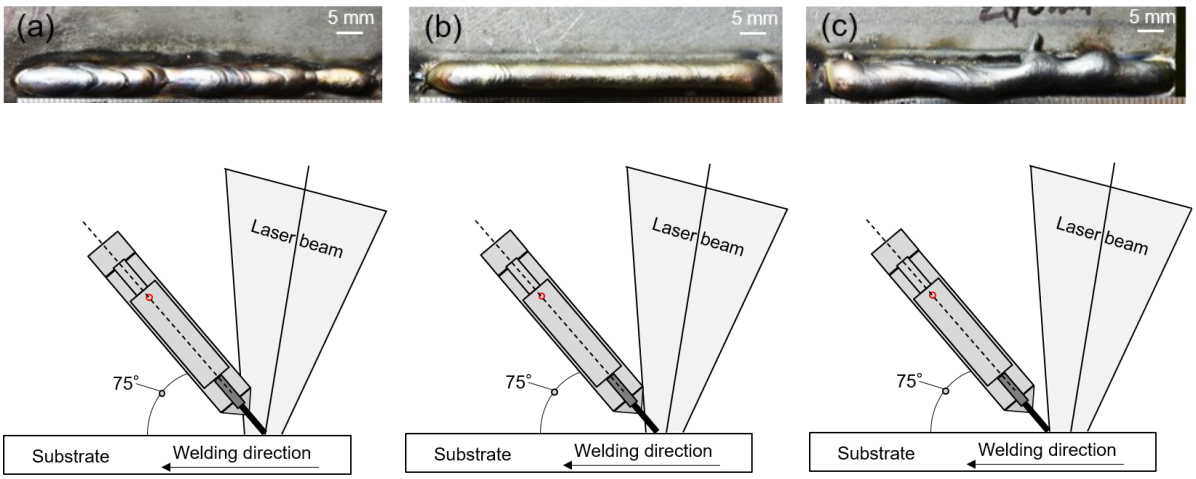

Position 1: D ≤ 0 mm Position 2: 0 ≤ D ≤ r mm Position 3: D ≥ r mm

Fig. 6.5. The effect of wire feeding position to the deposited layer stability.

In order to closely examine the melting of the base material and the wire feeding phenomenon, the HLAM process was taken by the high-speed camera. Fig. 6.6 shows the obtained images when feeding the wire to the edge of the laser beam (D ≥ r mm). It can be seen that the droplets were formed discontinuously in the tip of the filler wire and dropped on the substrate, as shown in Fig. 6.6b. The temperature of the hot-wire was close to its melting point and the excessive central laser energy exhibited the wire dripping defects (see in Fig. 6.6d). Fig. 6.7 shows the images of wire stubbing defects taken by the high-speed camera when feeding the wire to the center of the laser beam (D ≤ 0 mm). It can be seen that the excessive low energy density of the laser beam sides could not melt hot-wire completely, which caused the unmelt wire to slip off the molten pool as demonstrated in Fig. 6.7c. This confirms that the selection of the wire feeding position is very important for smooth hot-wire feeding and uniform bead formation.

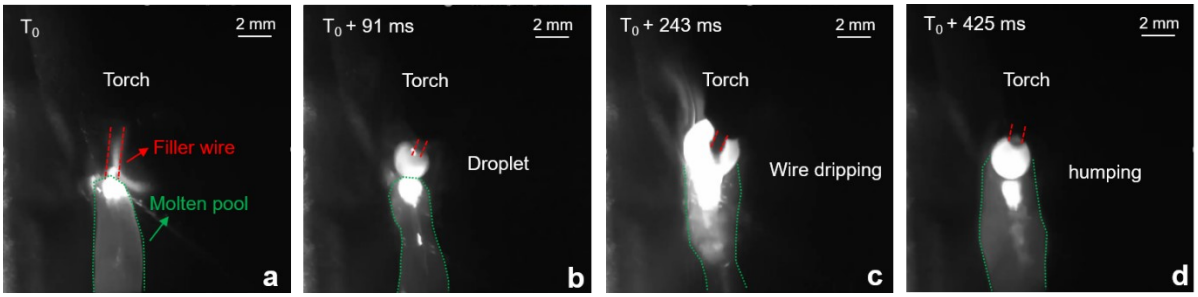

Fig. 6.6. High-speed images of wire dripping defects (D ≥ r mm).

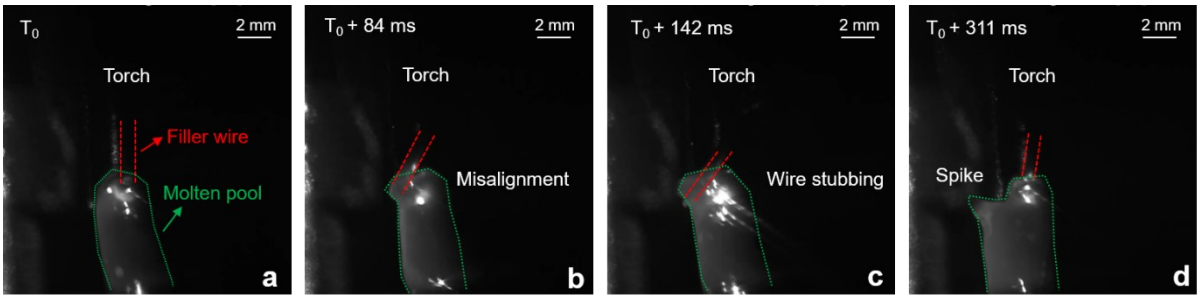

Fig. 6.7. High-speed images of wire stubbing defects (D ≤ 0 mm).

6.4 The process characteristics of deposited layer

In a diode laser beam, the energy density in the central region is higher than in the edge region. It is significant to study the appropriate energy density, which influences by the laser spot area, laser power, and defocuses length, to achieve a constant and stable molten pool formation.

The following equations can be used to calculate the energy heat input (Q_E):

$$Q_E = E / V_P \quad (6.1)$$

Where E is the energy density, in W/mm^2, obtained from the laser beam profile (see in Table 3) and V_P is the process speed, in mm/sec;

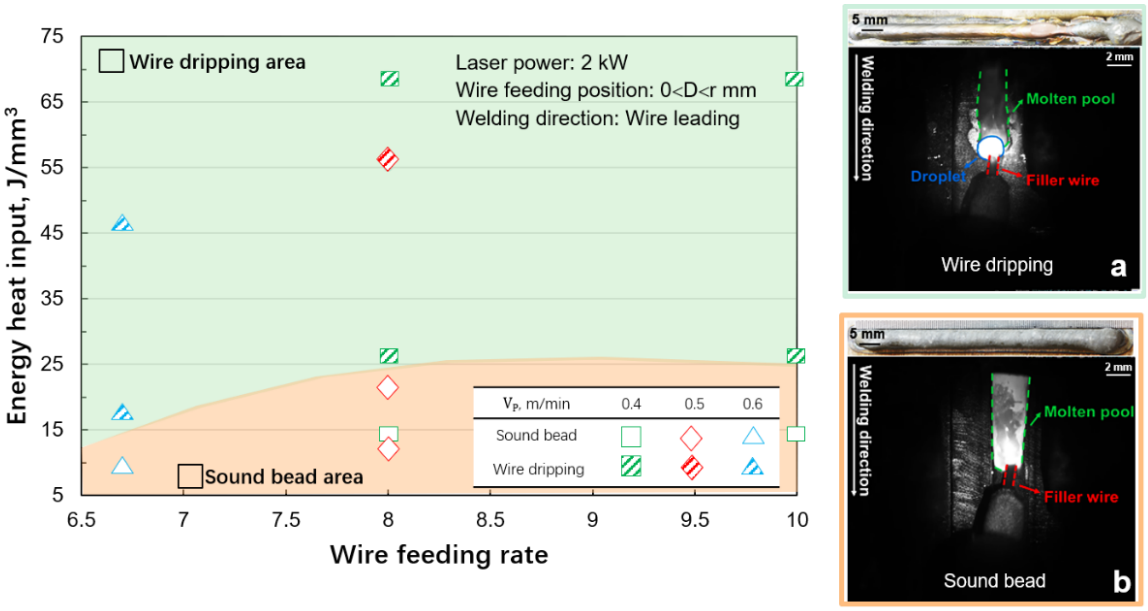

Fig. 6.8. The process characteristics of deposited layer.

Figure 6.8 shows the evaluated process characteristics results of the deposited layer on the relationship between the energy heat input (see Equation 6.1) and the wire feeding rate. The orange color area and green color area indicate the sound bead and wire dripping, respectively. When the wire feeding rate was 8 and 10, The energy heat input of 21 J/mm^3 as the limitation of the maximum energy heat input to achieve the stable wire feeding even if the process speed was varied from 0.4 to 0.5 m/min. When the wire feeding rate decreased to 6.7, the limitations of the maximum energy heat input of ~10 J/mm^3 resulted to achieve a sound bead, respectively. When the energy heat input was excessive, the droplet size exceeding 2.5 mm in diameter was formed in the tip of wire and dropped on the previous layer, leading to an irregular bead, as shown in Fig. 6.8a. When the energy heat input decreased to an appropriate range, there were no droplets formed in the process and the bead was uniform and smooth, as shown in Fig. 6.8b. Thus, the wire dripping defects during the deposition was obviously depended on the relationship between the wire feeding rate and the energy heat input, which determined by the defocus length when the laser spot size and laser power were fixed.

Moreover, the energy heat input increases with increasing the energy density, which means excessive energy heat input of central region resulted in filler wire melting before touch the substrate. In other words, small diode laser beam with uniform and suitable energy heat input can avoid wire dripping defects. Based on the obtained results, it can be concluded that the sound bead with no defects could be fabricated under the suitable energy heat input ranging from ~10 to 21 J/mm^3 when the wire feeding rate is from 6.7 to 10.

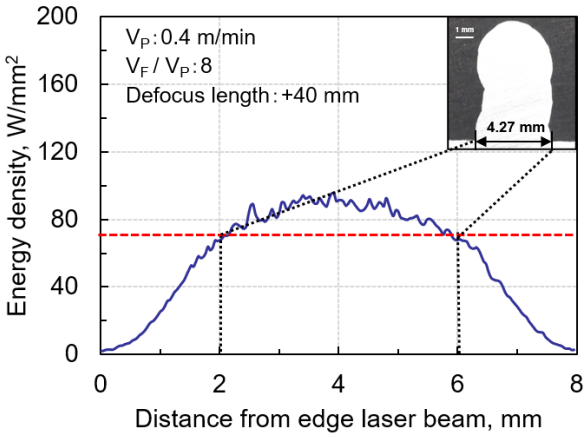

Fig. 6.9. Bead width as a function of minimum energy density.

Fig. 6.9 shows the bead width as a function of minimum energy density to melt the base metal. It can be seen that the energy density can exceed the critical value of 70 W/mm^2 when the distance from the edge laser beam is between 2 and 6 mm. When the distance from the edge laser beam is below 2 mm and over 6 mm, the energy density cannot reach the critical energy density to obtain the stable bead with no defects since the laser power is too low to distribute the sufficient energy to enable the base material to be melted. On the other hand, it can be presumed that the energy was dispersed rather than concentrated during laser irradiation since defocus length increases, resulting in lower energy heat input. Therefore, it can be noted that the sound bead with a width of 4.27 mm without any defects can be achieved with the limitation of energy heat input was ~10.5 J/mm^3.

6.5 Comparison between wire leading and laser leading

The effect of welding direction such as hot-wire leading and laser leading on the surface quality and deposited metal was investigated. Figure 6.10 shows the typical examples of high-speed images and bead appearance during the HLAM process under different welding directions. For the wire leading direction, the convex molten pool was formed under the thin layer and the uneven liquid metal flow caused a humping defect, as shown in Fig. 6.10a. On the other hand, for the laser leading direction, the liquid metal flowed uniformly in the molten pool and produced the sound bead with no defects, as provided in the low side of Fig. 6.10b. Most of the laser energy cannot be irradiated on the hot-wire because the hot-wire has a certain distance from the laser spot. Nevertheless, the tip of hot-wire has been heated to near the melting point before reaching the molten pool. Therefore, hot-wire can be continuously melted in the rear molten pool.

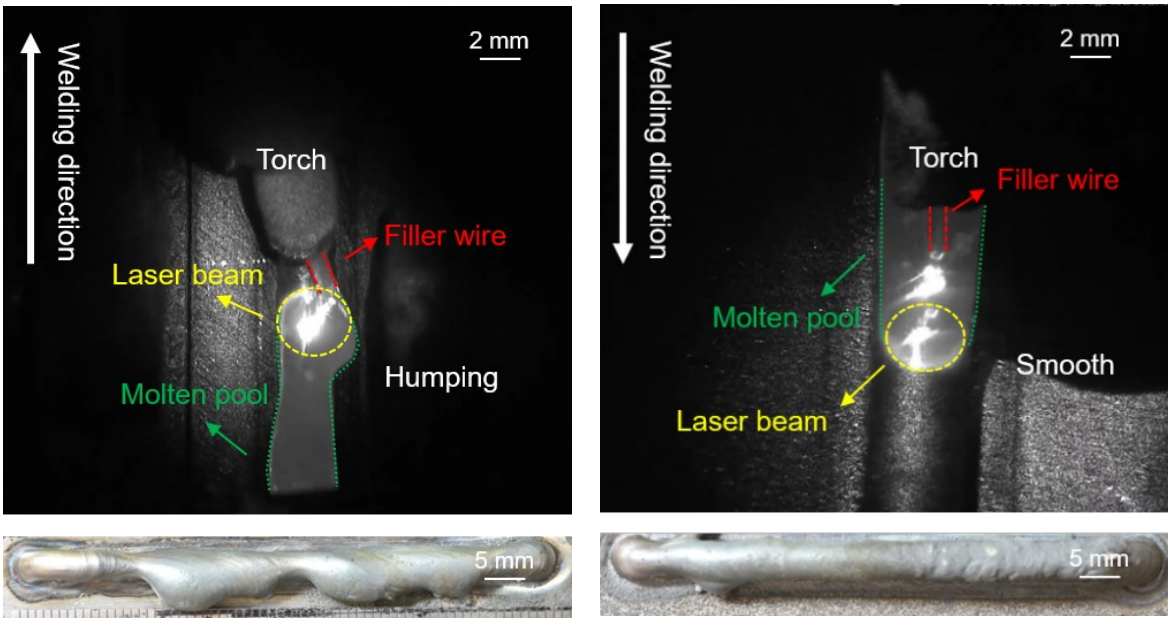

(a) (b)

Fig. 6.10. Typical high-speed images and bead appearance of welding direction: (a) Wire leading; (b) Laser leading.

The schematic illustrations of liquid metal flows in the molten pool are provided in Fig. 6.11. The schematic illustration of the hot-wire leading is indicated in Fig. 6.11a, while that of the laser leading is indicated in Fig. 6.11b. As shown in Fig. 6.11a, when the hot-wire feeds in front of the molten pool on the substrate, a strong backward liquid

metal flowed to the rear in the molten pool. This phenomenon exhibited oscillations and instability of wire feeding produced a convex and concave deposited metal. On the other hand, as shown in Fig. 6.11b, when the how-wire feeds behind the molten pool, the feeding of the hot-wire pushed a forward flow of the liquid metal, thus the hot-wire could be successfully provided in the molten pool. Meanwhile, the small molten pool is created at the forefront of the weld bead due to the laser irradiation in advance, which acids the backward flow along the edges of the molten pool. This liquid metal flow condition can significantly avoid the humping defects and improved the shape of the bead, which leads to the outstanding mechanical properties.

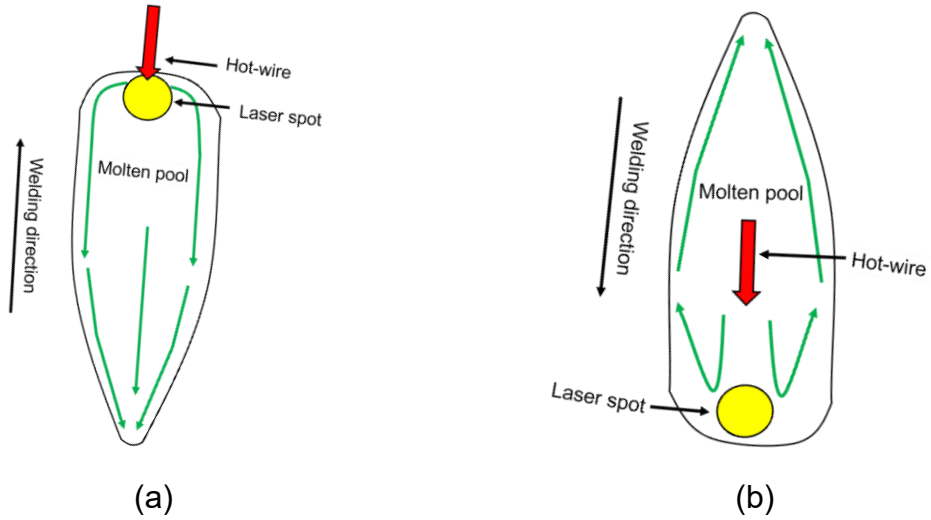

Fig. 6.11. Schematics illustration of liquid metal flow in the molten pool: (a) Wire leading; (b) Laser leading.

6.6 Effect of process speed on deposited bead characteristics and microstructure

The aim of the HLAM technique was to maximize the near net shape rate and to improve material utilization at narrow beam size. In order to investigate the influence of process speeds on the cross-sectional characteristics including the effect width, the effective height, the maximum height and the near-net shape rate and microstructure, the process speed (V_P) was varied from 0.4 to 0.8 m/min at a constant laser power (L_P) of 2 kW, a defocus length of +40 mm, and laser leading feeding angle of 75°. Fig. 6.12 and Table 6.4 show the cross-sectional characteristics of deposited three-layer at the different process speed. The results show that as the process speed increased from 0.4 to 0.8 m/min, the effective width (W_E) and the effective height (H_E) were reduced from 3.8 mm to 2.7 mm and from 6.2 mm to 3.8 mm, respectively, as shown in Fig. 6.12b and Fig. 6.12c. Meanwhile, with increasing the process speed from 0.4

to 0.6 m/min, the near net shape rate increased, while it decreased with increasing the process speed from 0.6 to 0.8 m/min, as shown in Fig. 6.12d. These results can suggest that the combination of wire feeding speed and process speed is one of the most significant factors on the bead characteristics. It is worth noting that when the process speed and wire feeding rate is appropriate (V_P = 0.6 m/min, V_F / V_P = 6.7), the shape of cross-sections becomes more spherical and full and a high material utilization rate (near net shape rate= 81%) was produced. At a lower process speed of 0.4 m/min (V_F / V_P = 10), the bead appearance became unstable as the amount of deposited wire increased, causing the waste of materials. Thus, the near net shape rate was reduced. While at a higher process speed of 0.8 m/min (V_F / V_P = 5), it can be considered that even though the bead formation was stable, the material efficiency was lowered since the amount of wire feeding was insufficient.

Table 6.4 Process conditions.

Samples	Process parameters				Cross-sections characteristics		
	L_P, kW	V_P, m/min	V_F, m/min	V_F / V_P	W_E, mm	H_E, mm	NNSR, %
DM1	2.0	0.4	4.0	10	3.8	7.6	72.6
DM2	2.0	0.6	4.0	6.7	3.5	6.0	80.3
DM3	2.0	0.8	4.0	5	3.0	4.2	75.9

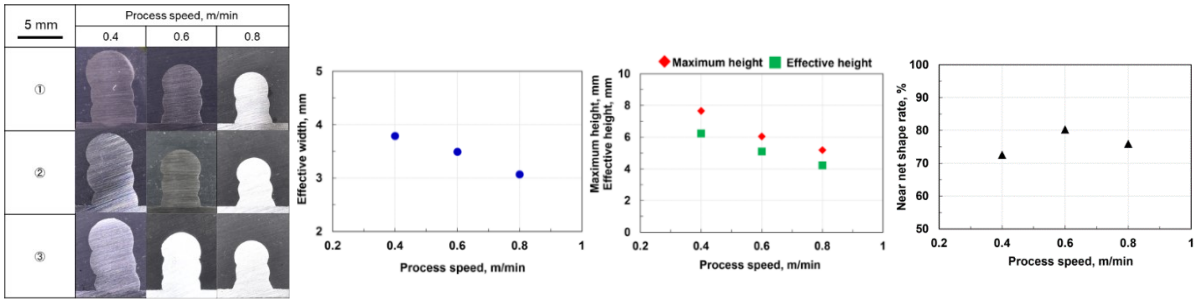

(a) (b) (c) (d)

Fig. 6.12. Cross-sectional evaluation of (a) cross-section surface, (b) effective width, (c) effective height and maximum height, and (d) near net shape rate.

In order to provide an insight into the microstructure evolutions associated with the hot-wire laser AM process, the microstructure formed in the deposited materials fabricated at the different process speed was examined; the results are shown in Fig. 6.13. The microstructure characterizations showed that the columnar dendrite was

formed since the process of melting and solidification experienced during the HLAM process, which induced non-equilibrium cooling conditions. At 0.4 m/min, the vermicular and skeletal δ-ferrite phases in a γ austenite matrix were formed, as shown in Fig. 6.13a. At 0.6 m/min as shown in Fig. 6.13b, the vermicular and both the skeletal and lathy δ-ferrite phases inside distinct prior austenite grains. While at 0.8 m/min, the microstructure is mainly formed by a large number of lathy δ-ferrite phases and a small amount of γ austenite, as shown in Fig. 6.13c. It can be recognized that the diameter of the prior austenite grains decreased with the increasing process speeds. This result can be attributed to that the peak process temperature decreased as the process speed increased. When the peak temperature was low, the materials suffered the less time to grain growth during the melting and solidification processes. Moreover, the lamellar spacing formed inside the prior austenite grains gradually decreased with the process speeds. This result is presumed to be due to the different cooling rates. It can be considered that the cooling rate of the bead fabricated at a higher process speed is generally lower than that fabricated at a lower process speed and a lower cooling rate could effectively suppress the growth of lamellar spacing during the solidification process.

Furthermore, the microstructure formations at the different process speeds can be discussed as follows. It is well known that the solidification variation in microstructure of stainless steel can be determined by the ratio of Cr_{eq}/Ni_{eq}. In order to clarify this phenomenon, the Eq. (6.2) and (6.3) can be adopted to calculate the ratio of the filler materials [23, 32-33]:

$$\mathrm{Cr_{eq}(wt\%) = Cr + 2(Si) + 1.5(Mo) + 5(V) + 5.5(Al) + 1.75(Nb) + 1.5(Ti) + 0.5(W)} \quad (6.2)$$

$$\mathrm{Ni_{eq}(wt\%) = Ni + (Co) + 0.5(Mo) + 0.3(Cu) + 25(N) + 30(C)} \quad (6.3)$$

The calculated ratio of the Cr_{eq}/Ni_{eq} was found to be 2.99. Thus, the solidification mode of the three samples is recognized as F mode as shown in Eq. (6.4) which is :

$$L \rightarrow L + \delta \rightarrow \delta \rightarrow \delta + \gamma \text{ (F mode)} \quad (6.4)$$

Where L is the liquid, δ is delta-ferrite and γ is austenite and, respectively. The L+ δ-ferrite then transforms to δ-ferrite followed by a solid-state transformation during cooling. It can be concluded that the solidification mode of the three deposited metals are actually F mode. The morphology of the ferrite is significantly influence by the values of Cr_{eq}/Ni_{eq} and cooling rates. At 0.4 m/min, the normal morphology of phase is composed by vermicular and skeletal residual δ-ferrite phases because the low cooling rates allowed the growth of the γ-austenite and sufficient diffusion. At 0.6 m/min, the lathy phases were formed because diffusion-controlled transformation of γ-austenite. At 0.8 m/min, the content of lathy δ-ferrite increases with increasing process speed because the diffusion controlled transformation limited the γ-austenite occur at high cooling rates.

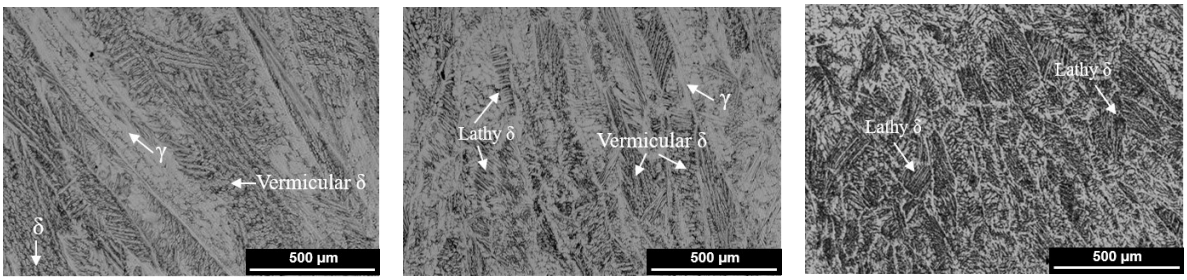

(a) (b) (c)

Fig. 6.13. Microstructure: (a) V_P = 0.4 m/min, (b) V_P = 0.6 m/min, and (c) V_P = 0.8 m/min.

6.7 Summary

This section demonstrated the use of an HLAM method with 630 stainless steel wire. The optimization of processing conditions, such as wire feeding position, defocus length, welding directions, and process speed was studied. The main conclusions of the work are as follows:

1) The wire feeding position significantly affected the stability of the HLAM process. The wire feeding position that is too close (D ≤ 0 mm) or too far (D ≥ r mm) from laser beam center results in wire dripping or wire stubbing, respectively. When the wire feeding position (0 < D < r mm) was appropriate, the homogeneous width deposited metal without any defects could be obtained.

2) A process map between the energy heat input and wire feeding rate was established for predicting the suitable defocus length. The sound bead with no defects could be fabricated under the suitable energy heat input ranging from ~10 to 21 J/mm^3 when the wire feeding rate is from 6.7 to 10. The substrate can be melted with the limitation of energy heat input was ~10.5 J/mm^3.

3) Compared with wire leading, the laser leading process that pushed a forward flow of the liquid metal and acids the backward flow along the edges of the molten pool. The laser leading condition can significantly avoid the humping defects and improved the shape of the bead.

4) In narrow beam spot, the HLAM process can change the processing speed dramatically, which can easily control the cooling rate, energy heat input, and microstructure phases.

Chapter 7

Summary and future work

The final purpose of this research is to develop a novel additive manufacturing technology using a combination of a high-power diode laser and hot-wire method with three types of metallic materials: Stainless steel, Ni-based alloy, and 5xxx-series Aluminum alloy. In this method, a laser beam with high controllability serves as the main heat source, and another heat source is Joule heat that is generated by a hot-wire current, which heats the filler cold-wire to its melting point independently from the heat input of the main heat source for base metal melting.

Firstly, the theoretical backgrounds, history of AM technology, and the objectives and construction of this thesis were discussed. The novel and relative research of the metal additive manufacturing (e.g. powder-feeding MAM and wire-feeding MAM) technology and MAM technologies of various metallic materials (e.g. stainless steel, Ni-based alloys, and Aluminum alloy) were summarized.

In order to easily control the hot-wire phenomenon, a simple calculation method to predict the appropriate wire current was proposed and confirmed by hot-wire feeding experiments without laser irradiation. As a result, the appropriate hot-wire current for heating the wire tip to nearly its melting point for four wires (SUS308L, SUS630, Inconel625, and A5356WY) with different electrical resistivity was obtained by both theoretical calculation and experiment methods. In this calculation equations, the appropriate current value under different conditions (e.g. wire feeding speed, wire diameters, temperature-dependent specific heat, temperature-dependent specific gravity, and temperature-dependent specific electrical resistivity) could be obtained. When considering both heat loss from heat convection and heat generation by contact resistance, the estimated current is in good agreement with the experimental values over a wide range of wire feeding speeds from 0 to 20 m/min for all four filler materials.

Then, the hot-wire laser AM by using SUS308L wire was investigated at first. The two-layer and three-layer deposited samples were then proposed and evaluated. High-speed imaging was performed to monitor clear wire melting phenomena and molten pool formation during AM processing. In two-layer deposition, a large width above 10 mm and a high deposition rate above 800 cm^3/h were achieved. In three-layer-deposition, there are many parameters involved in the process conditions, including laser power, process speed, wire feeding rate, and energy heat input, mainly affect the melting phenomenon and bead appearance. It is found that the energy heat input was proposed as being key to obtaining adequate and stable melting phenomena. Moreover, a sufficiently high wire feeding speed (rate) should be used according to the laser beam width and processing speed before optimizing other parameters in the proposed HLAM process.

Next, the optimization of the process parameters of three types of wires (SUS308L, Inconel625, and A5356WY) by using the HLAM method was investigated. The process parameters (i.e. laser power, process speed, and wire feeding rate affected obviously the bead shape (i.e. effective width, effective height, maximum height, and near net shape rate). As a result, all three-layers and cross-sections are uniform without any defects. The wire feeding rate had the biggest effect on height and the near net shape rate. The optimized AM process parameters were obtained from the viewpoint of higher material utilization and more stable bead formation according to cross-sectional evaluations. An excessively high and low wire feeding rate resulted in a parabolic and swollen shape, respectively. Therefore, sound three-layers and cross-sections without any defects were obtained for the three materials types using the optimized process parameters. A wide effective width almost 10 mm, and a high wire feeding speed of 12–20 m/min (deposition rate of approximately 800–1300 cm^3/h) were achieved. Moreover, three large wall-type parts with the effective width of ~10 mm, effective height above ~40 mm, and length above ~200 mm were fabricated by using optimized process conditions. A sufficient tensile strength and elongation of three materials were achieved.

Finally, a hot-wire method combined with narrow laser spot size (4-8 mm) for the deposition of 630 stainless steel was investigated. The effect of processing conditions including the wire feeding position, defocus length and welding direction on the stability of deposition along with the effect of the energy density distribution and process speed. In narrow spot size, the wire feeding position significantly affected the stability of the HLAM process. The wire feeding position that is too close ($D \leq 0$ mm) or too far ($D \geq r$ mm) from laser beam center results in wire dripping or wire stubbing, respectively. The sound bead with no wire dripping defects could be fabricated under the suitable energy heat input ranging from ~10 to 21 J/mm^3 when the wire feeding rate is from 6.7 to 10. Compared with wire leading, the laser leading process can pushed a forward flow of the liquid metal and keep a nice and enough molten pool. Thus, the laser leading condition can significantly avoid the humping defects and improved the shape of the bead. In narrow spot size, the effect of process speed on the bead shape and microstructure of the deposited three-layer was also investigated. As a results, the deposited metals solidify in F mode, and the morphologies of ferrite are vermicular, skeletal and lathy. The HLAM process can change the processing speed dramatically, which can easily control the cooling rate, energy heat input, and microstructure phases.

In this study, the novel HLAM method of the similar to single materials (SUS/SUS, Al/Al) was mainly introduced. The investigation of wire feeding phenomena and creation of molten pool during multi-layer deposition were also proposed. Moreover, the optimized parameters, such as laser power, wire feeding rate, wire current, and process speed under different process conditions, such as the laser beam with large rectangle and narrow spot shape, defocus length, wire feeding position, welding direction and so on were studied in detail.

In the future, we are conducting further experiments, related to mechanical properties (i.e. tensile test, hardness distribution) in the building direction and welding direction, and material characterizations. It is significant to analyze materials

characterization and hardness distributions for the future reported pater. In this case, the relationship between the microstructures, hardness distribution, and mechanical properties of the obtained deposited metal by this process can be clearly investigated. Moreover, the HLAM method will be used in multi-materials and gradient materials. Because the energy heat input of the hot-wire laser process is uniform and relatively low, this method can be heated wire to its melting point while minimizing the energy heat input to the substrate which is beneficial to reducing the IMC thickness and avoiding interfacial defects. Therefore, the development of hot-wire laser process for the deposition of Al/Fe and Al/Ti dissimilar material is significant and interesting.

Acknowledgements

I must first and foremost express my deepest gratitude to Professor Motomichi Yamamoto for his support, guidance, patience, motivation, and insight throughout this research. He allowed me to work in his laboratory and gave me his valuable time and expertise to make this dissertation possible. There is no amount of gratitude I can express that comes close to appreciating his kindness on me.

I am also grateful to Professor Kenji Shinozaki, who gave me encouragement, confidence, and instructive discussion in my study, I have learnt so much from him. Furthermore, I would like to thank Assistant Professor Jeong-Won Choi. He gave me so much positive help on my dissertation and broadened my research horizons.

I would like to thank the rest of my dissertation committee for their insightful comments and encouragement, but also for the hard question which incented me to widen my research from various perspectives.

I would like to appreciate the help of Mr. Nakahara, Mr. Marumoto, Mr. Kono, Mr. Hourai, Mrs. Luo, Mr. Yang, and Mr. Su. I would also like to thank all the past and present members of the Materials Joining Science and Engineering Laboratory, in the Department of Mechanical Science and Engineering, Hiroshima University, for their enthusiastic help to both my life and study.

I would like thank my parents for their support and encouragement from my youth to my time as a doctoral student. Their teaching is gratefully appreciated and has been invaluable in my life.

Reference

1) E. Davoodi, H. Montazerian, A.S. Mirhakimi, and et al. Additively manufactured metallic biomaterials, Bioactive materials, 14(2022), 214-249.
2) L.Y. Chen, S.X. Liang, Y.J. Liu, and L.C. Zhang. Additive manufacturing of metallic lattice structures: Unconstrained design, accurate fabrication, fascinated performances, and challenges, Materials Science and Engineering: R: Reports, 146(2021), 100648.
3) J.O. Milewski. Additive manufacturing of metals, Springer series in materials science, 258(2017), 7-33.
4) W.E. Frazier. Metal Additive Manufacturing: A Review, ASM International, 23(2014), 1917-1928.
5) V. Schultz, T. Seefeld, and F. Vollertsen. Gap bridging ability in laser beam welding of thin aluminum sheets, Physics Procedia, 56(2014), 545–553.
6) R. Suzuki, Engineering Data sheet, J.JWS, 75–6(2005), 459.
7) A. Bandyopadhyay and S. Bose. Additive Manufacturing, CRC Press, Florida, 2015.
8) I. Gibson, D.W. Rosen, and B. Stucker. Additive Manufacturing Technologies: Rapid Prototyping to Direct Digital Manufacturing, Springer, Berlin, 2009.
9) J.D. Cawley. Solid freeform fabrication of ceramics. Current Opinion in Solid State and Materials Science, 4(1999), 483–489.
10) S.W. Williams, F. Martina, A.C. Addison, J. Ding, G. Pardal, and P. Colegrove. Wire+ Arc Additive Manufacturing, Materials Science and Technology, 32(2016), 641-647.
11) F. Chen, Y.R. Wu, J.M. Wu, and et al. Preparation and characterization of ZrO_2-Al_2O_3 bioceramics by stereolithography technology for dental restorations, Additive manufacturing, 44(2021), 102055.
12) T. DebRoy, H.L. Wei, J.S. Zuback, T. Mukherjee, J.W. Elmer, J.O. Milewski, A.M. Beese, A. Wilson-Heid, A. De, and W. Zhang. Additive manufacturing of metallic components-Process, structure and properties, Progress in Materials Science, 92(2018), 112-224.
13) S. Zakaria, P. Mativenga, and A. Cseke. Energy Consumption and Scope 2 Emissions for Fused Deposition Modelling, Procedia CIRP, 105(2022), 31-36.
14) M. Moradi, Z. Pourmand, A. Hasani, and et al. Direct laser metal deposition (DLMD) additive manufacturing (AM) of Inconel 718 superalloy: Elemental, microstructural and physical properties evaluation, Optik, 249(2022), 169018.
15) M.J. Cotteleer. 3D opportunity: Additive manufacturing paths to performance

innovation, and growth, Deloitte Services, LLP, 2014.
16) Y.W. Zhai, D.A. Lados, and J.L. Lagoy. Additive Manufacturing: Making Imagination the Major Limitation, The Minerals, Metals & Materials Society, 66(2014), 808-816.
17) T. Wohlers. Report 201Fort Collins, CO: Wohlers Associates, 2011.
18) B. Berman. 3-D printing: The new industrial revolution, Business Horizons, 55(2012), 155-162.
19) D.K.R. Robinson, A. Lagnau, and W.P.C. Boon. Innovation pathways in additive manufacturing: Methods for tracing emerging and branching paths from rapid prototyping to alternative applications, Technological Forecasting and Social Change, 146(2019), 733-750.
20) C. Tutor. Additive Manufacturing: analysis of the economic context and evaluation of the indoor air quality, with a Total Quality Management approach, Department of Economics, Society, Politics, University of Urbino, 2018.
21) S.A.M. Tofail, E.P. Koumoulos, A. Bandyopadhyay, S. Bose, L.O. Donoghue, and C. Charitidis. Additive manufacturing: scientific and technological challenges, market uptake and opportunities, Materials Today, 21(2018), 22-37.
22) X. Lin, K.P. Zhu, J.Y.H Fuh, and X.Y. Duan. Metal-based additive manufacturing condition monitoring methods: From measurement to control, ISA Transactions, 120(2022), 147-166.
23) S.G. Chen, H.J. Gao, Y.D. Zhang, Q. Wu, Z.H. Gao, and X. Zhou. Review on residual stresses in metal additive manufacturing: formation mechanisms, parameter dependencies, prediction and control approaches, Journal of Materials Research and Technology, 17(2022), 2950-2974.
24) H. Monteiro, G.C. Aparicio, I. Lei, and M. Despeisse. Energy and material efficiency strategies enabled by metal additive manufacturing – A review for the aeronautic and aerospace sectors, The 8th International Conference on Energy and Environment Research ICEER 2021, 8(2022), 13-17.
25) C. Sungail and A. Abid. Spherical tantalum feed powder for metal additive manufacturing, Metal Powder Report, 73(2018), 316-318.
26) J.L. Zou, Z. Wang, Y. Zhao, X. Han, and J.J. Gong. In situ measurement of particle flow during fiber laser additive manufacturing with powder feeding, Results in Physics, 37(2022), 105483.
27) H.S. Dhami, P.R. Panda, and K. Viswanathan. Production of powders for metal additive manufacturing applications using surface grinding, Manufacturing Letters, 32(2022), 54-58.
28) X.X. Yao, J.Y. Li, Y.F. Wang, X. Gao, T. Li, and Z. Zhang. Experimental and

numerical studies of nozzle effect on powder flow behaviors in directed energy deposition additive manufacturing, International Journal of Mechanical Sciences, 210(2021), 106740.
29) Z. Zhang, P. Ge, T. Li, L.E. Lindgren, W.W. Liu, G.Z. Zhao, and X. Guo. Electromagnetic wave-based analysis of laser–particle interactions in directed energy deposition additive manufacturing, Additive Manufacturing, 32(2020), 101284.
30) S.A. Khairallah, A.T. Anderson, A. Rubenchik, and W.E. King. Laser powder-bed fusion additive manufacturing: Physics of complex melt flow and formation mechanisms of pores, spatter, and denudation zones, Acta Materialia, 108(2016), 36-45.
31) A. Heralića, A.K. Christiansson, M. Ottosson, and B. Lennartson. Increased stability in laser metal wire deposition through feedback from optical measurements, Optics and Lasers in Engineering, 48(2010), 478-485.
32) D.H. Ding, Z.X. Pan, D. Cuiuri, and H.J. Li. Wire-feed additive manufacturing of metal components: technologies, developments and future interests, The International Journal of Advanced Manufacturing Technology, 81(2015), 465-481.
33) A. Kapil, T. Suga, M. Tanaka, and A. Sharma. Towards hybrid laser-arc based directed energy deposition: Understanding bead formation through mathematical modeling for additive manufacturing, Journal of Manufacturing Processes, 76(2022), 457-474.
34) M.X. Yao, Z.J. Yao, X.W. Tao, C.J. Huang, and S.S. Zhang. Alleviating plastic anisotropy of boron modified titanium alloy by constructing layered structure via electron beam directed energy deposition, Additive Manufacturing, 50(2022), 102561.
35) Y. Li, C. Su, and J.J. Zhu. Comprehensive review of wire arc additive manufacturing: Hardware system, physical process, monitoring, property characterization, application and future prospects, Results in Engineering, 13(2022), 100330.
36) N.A. Rosli, M.R. Alkahari, M.F.B. Abdollah, S. Maidin, F.R. Ramli, and S.G. Herawan. Review on effect of heat input for wire arc additive manufacturing process, Journal of Materials Research and Technology, 11(2021), 2127-2145.
37) Z.Y. Liang, B.H. Chang, H.Y. Zhang, Z.X. Li, and et al. Electric current evaluation for process monitoring in electron beam directed energy deposition, International Journal of Machine Tools and Manufacture, 176(2022), 103883.
38) I. Utke, P. Swiderek, K. Höflich, K. Madajska, J. Jurczyk, and et al. Coordination

and organometallic precursors of group 10 and 11: Focused electron beam induced deposition of metals and insight gained from chemical vapour deposition, atomic layer deposition, and fundamental surface and gas phase studies, Coordination Chemistry Reviews, 458(2022), 213851.

39) D.X. Yang, X.Y. Li, D.Y. He, Z.R. Nie, and H. Huang. Optimization of weld bead geometry in laser welding with filler wire process using Taguchi's approach, Optics & Laser Technology, 44(2012), 2020-2025.
40) F. Du, J.Q. Zhu, X.P. Ding, Q. Zhang, H.L. Ma, and et al. Dimensional characteristics of Ti-6Al-4V thin-walled parts prepared by wire-based multi-laser additive manufacturing in vacuum, Rapid Prototyping Journal, 25(2019), 849-856.
41) P. Wen, Z.P. Cai, Z.H. Feng, and G. Wang. Microstructure and mechanical properties of hot wire laser clad layers for repairing precipitation hardening martensitic stainless steel, Optics & Laser Technology, 75(2015), 207-213.
42) A. Pai, I. Sogalad, P. Kumar, S. Basavarajappa, and S.J. Suresha. Impact properties of modified 9Cr 1Mo steel welds: Comparison between cold wire and hot wire gas tungsten arc welding processes, International Journal of Pressure Vessels and Piping, 2022, 104672.
43) J.P.M. Pragana, R.F.V. Sampaio, L.M.F. Braganca, C.M.A. Silva, and P.A.F. Martins. Hybrid metal additive manufacturing: A state–of–the-art review, 2(2021), 100032.
44) P.D. Murugan, S. Vijayananth, M.P. Natarajan, D. Jayabalakrishnan, K. Arul, V. Jayaseelan, and J. Elanchezhian. A current state of metal additive manufacturing methods: A review, Materials Today: Proceedings, 2021.
45) R.S. Mahale, V. Shamanth, K. Hemanth, S.K. Nithin, P.C. Sharath, R. Shashanka, A. Patil, and D. Shetty. Processes and applications of metal additive manufacturing, Materials Today: Proceedings, 54(2021), 228-233.
46) G.H. Gong, J.J. Ye, Y.M. Chi, Z.H. Zhao, Z.F. Wang, and et al. Research status of laser additive manufacturing for metal: a review, Journal of Materials Research and Technology, 15(2021), 855-884.
47) C.L. Tan, F. Weng, S. Sui, Y.X. Chew, and G.J. Bi. Progress and perspectives in laser additive manufacturing of key aeroengine materials, International Journal of Machine Tools and Manufacture, 170(2021), 103804.
48) K. Moeinfar, F. Khodabakhshi, S.F. Kashani-bozorg, M. Mohammadi, and A.P. Gerlich. A review on metallurgical aspects of laser additive manufacturing (LAM): Stainless steels, nickel superalloys, and titanium alloys, 16(2022), 1029-1068.

49) M.M. Ruthandi. High-efficiency and High-quality Laser Welding of Difficult-to-weld Materials, Graduate School of Natural Science and Technology, Okayama university, 2019.
50) H.S. Prasad, F. Brueckner, J. Volpp, and A.F.H. Kaplan. Laser metal deposition of copper on diverse metals using green laser sources, The International Journal of Advanced Manufacturing Technology, 107(2020), 1559-1568.
51) M. Matsui, T. Ono, T. Kamei, and K. Mori. Generating conditions of argon laser-sustained plasma by disk, fiber and diode lasers, Vacuum, 167(2019), 490-494.
52) K. Saida, W. Song, and K. Nishimoto. Diode laser brazing of aluminium alloy to steels with aluminium filler metal, Science and Technology of Welding and Joining, 10(2005), 227-235.
53) H. Nasim and Y. Jamil. Diode lasers: From laboratory to industry. Optics & Laser Technology, 56(2014), 211-222.
54) S.B. Zhao, C.P. Jia, Y.X. Yuan, L.X. Wang, Y.M. Huang, and L.J. Yang. Effects of laser remelting on microstructural characteristics of Ni-WC composite coatings produced by laser hot wire cladding, Journal of Alloys and Compounds, 908(2022), 164612.
55) W.H. Huang, J. Xiao, S.J. Chen, X.Q. Jiang. Control of wire melting behavior during laser hot wire deposition of aluminum alloy, Optics and Laser Technology, 150(2022), 107978.
56) M. Kottman, S.J. Zhang, J. McGuffin-Cawley, P. Denney, and B.K. Narayanan. Laser Hot Wire Process: A Novel Process for Near-Net Shape Fabrication for High-Throughput Applications, The Minerals, Metals & Materials Society, 67(2015), 622-628.
57) S.Y. Chin, V. Dikshit, B.M. Priyadarshini, and Y. Zhang. Powder-Based 3D Printing for the Fabrication of Device with Micro and Mesoscale Features, Micromachines, 11(2020), 658.
58) Y. Wang, Z.Y. Xu, D.D. Wu, and J.M. Bai. Current Status and Prospects of Polymer Powder 3D Printing Technologies, Materials, 13(2020), 2406.
59) E.O. Olakanmi, R.F. Cochrane, and K.W. Dalgarno. A review on selective laser sintering/melting (SLS/SLM) of aluminium alloy powders: Processing, microstructure, and properties, Progress in Materials Science, 74(2015). 401-477.
60) K. Mumtaz and N. Hopkinson. Top surface and side roughness of Inconel 625 parts processed using selective laser melting, 15(2009), 96-103.
61) H.H. Zhu, L. Lu, and J.Y.H. Fuh. Development and characterisation of direct laser sintering Cu-based metal powder, Journal of Materials Processing

Technology, 140(2003), 314-317.
62) J.S. Keist and T.A. Palmer. Role of geometry on properties of additively manufactured Ti-6Al-4V structures fabricated using laser based directed energy deposition, Materials & Design, 106(2016), 482-494.
63) S.I. Shah, G.H. Jaffari, E. Yassitepe, and B. Ali. Chapter 4 - Evaporation: Processes, Bulk Microstructures, and Mechanical Properties, Handbook of Deposition Technologies for Films and Coatings (Third Edition), 2010, 135-252.
64) S.D. Jadhav, P.P. Dhekne, E. Brodu, B.V. Hooreweder, S.Dadbakhsh, and et al. Laser powder bed fusion additive manufacturing of highly conductive parts made of optically absorptive carburized CuCr1 powder, Materials & Design, 198(2021), 109369.
65) E.M. Sefene. State-of-the-art of selective laser melting process: A comprehensive review, Journal of Manufacturing Systems, 63(2022), 250-274.
66) C. Pauzon, E. Hryha, P. Forêt, and L. Nyborg. Effect of argon and nitrogen atmospheres on the properties of stainless steel 316 L parts produced by laser-powder bed fusion, Materials & Design, 179(2019), 107873.
67) R. Singh, A. Gupta, O. Tripathi, S. Srivastava, and et al. Powder bed fusion process in additive manufacturing: An overview, Materials Today: Proceedings, 2020.
68) P.L. Zhang, J. Tan, Y.T. Tian, H. Yan, and Z.S. Yu. Research progress on selective laser melting (SLM) of bulk metallic glasses (BMGs): a review, The International Journal of Advanced Manufacturing Technology, 118(2021), 2017-2057.
69) Y. Nakahara. Development of Addictive Manufacturing Technology Using High-power Diode Laser and Hot-wire Method, Hiroshima university, 2020.
70) K. Odum, M. Soshi, and K. Yamazaki. Measurement and analysis of impact dynamics suitable for modelling pneumatic transport of metallic powder flow through a directed energy deposition nozzle, Advanced Powder Technology, 33(2022), 103515.
71) M. Ansari, E. Jabari, and E. Toyserkani. Opportunities and challenges in additive manufacturing of functionally graded metallic materials via powder-fed laser directed energy deposition: A review, Journal of Materials Processing Technology, 294(2021), 117117.
72) D. Svetlizky, B.L. Zheng, A. Vyatskikh, M. Das, and et al. Laser-based directed energy deposition (DED-LB) of advanced materials, Materials Science and Engineering: A, 840(2022), 142967.
73) L. Liang, R.Z. Hu, J.S. Wang, A.G. Huang, S.Y. Pang. A thermal fluid

mechanical model of stress evolution for wire feeding-based laser additive manufacturing, Journal of Manufacturing Processes, 69(2021), 602-612.
74) Z.D. Lin, K.J. Song, and X.H. Yu. A review on wire and arc additive manufacturing of titanium alloy, Journal of Manufacturing Processes, 70(2021), 24-45.
75) Y.Z. Fu, A.R.J. Downey, L. Yuan, T.Y. Zhang, A. Pratt, and Y. Balogun. Machine learning algorithms for defect detection in metal laser-based additive manufacturing: A review, 75(2022), 693-710.
76) X.S. Li, Z.J. Yao, X.W. Tao, M.X. Yao, and S.S. Zhang. Developing Cu modified Ti6Al4V alloys with a combination of high strength and ductility by electron beam freeform fabrication, Vacuum, 194(2021), 110638.
77) X. Shu, G.Q. Chen, J.P. Liu, B.G. Zhang, and J.C. Feng. Microstructure evolution of copper/steel gradient deposition prepared using electron beam freeform fabrication, Materials Letter, 213(2018), 374-377.
78) J.Q. Xu, J. Zhu, J.K. Fan, Q. Zhou, Y. Peng, and S. Guo. Microstructure and mechanical properties of Ti–6Al–4V alloy fabricated using electron beam freeform fabrication, 167(2019), 364-373.
79) Z.X. Li, Y.N. Cui, L. Wang, H.Y. Zhang, Z.Y. Liang, C.M. Liu, and D. Du. An investigation into Ti-22Al-25Nb in-situ fabricated by electron beam freeform fabrication with an innovative twin-wire parallel feeding method, Additive Manufacturing, 50(2022), 102552.
80) P.M. Cordero, J. Mireles, S. Ridwan, and R.B. Wicker. Evaluation of monitoring methods for electron beam melting powder bed fusion additive manufacturing technology, Progress in Additive Manufacturing, 2(2017), 1-10.
81) Y.C. Wu, C.N. Kuo, Y.C. Chung, C.H. Ng, and J.C. Huang. Effects of Electropolishing on Mechanical Properties and Bio-Corrosion of Ti6Al4V Fabricated by Electron Beam Melting Additive Manufacturing, Materials, 12(2019), 1466.
82) K.M. Taminger and R.A. Hafley. Electron Beam Freeform Fabrication for Cost Effective Near-Net Shape Manufacturing, NATO/RTO, Amsterdam, 2006.
83) S.W. Williams, F. Martina, A.C. Addison, J. Ding, G. Pardal, and P. Colegrove. Wire + Arc Additive Manufacturing, Materials Science and Technology, 32(2016), 641-647.
84) J. Xiong, R. Li, Y.Y. Lei, and H. Chen. Heat propagation of circular thin-walled

parts fabricated in additive manufacturing using gas metal arc welding, Journal of Materials Processing Technology, 251(2018), 2019.

85) B.T. Wu, Z.X. Pan, D.H. Ding, D. Cuiuri, H.J. Li, J. Xu, and J. Norrish. A review of the wire arc additive manufacturing of metals: properties, defects and quality improvement, Journal of Manufacturing Processes, 35(2018), 127-139.

86) F. Honarvar and A.V. Farahani. A review of ultrasonic testing applications in additive manufacturing: Defect evaluation, material characterization, and process control, Ultrasonics, 108(2020), 106227.

87) N. Khanna, K. Zadafiya, T. Patel, Y. Kaynak, R. Abdul, R. Rashid, and A. Vafadar. Review on machining of additively manufactured nickel and titanium alloys, Journal of Materials Research and Technology, 15(2021), 3192-3221.

88) P.A. Colegrove, H.E. Coules, J.L. Fairman, F. Martina, T. Kashoob, H. Mamash, and L.D. Cozzolino. Microstructure and residual stress improvement in wire and arc additively manufactured parts through high-pressure rolling, Journal of Materials Processing Technology, 213(2013), 1782-1791.

89) Z.U. Arif, M.Y. Khalid, and E.U. Rehman. Laser-aided additive manufacturing of high entropy alloys: Processes, properties, and emerging applications, 78(2022), 131-171.

90) L. Yan, Y.T. Chen, and F. Liou. Additive manufacturing of functionally graded metallic materials using laser metal deposition, 31(2020), 100901.

91) Z.R. Yan, W.W. Liu, Z.J. Tang, X.Y. Liu, and et al. Review on thermal analysis in laser-based additive manufacturing, Optics & Laser Technology, 106(2018), 427-441.

92) M. Nankali, J. Akbari, M. Moradi, Z. Malekshahi, and Beiranvand. Effect of laser additive manufacturing parameters on hardness and geometry of Inconel 625 parts manufactured by direct laser metal deposition, Optik, 249(2022), 168193.

93) D.X. Yang, X.Y. Li, D.Y. He, Z.R. Nie, and H. Huang. Optimization of weld bead geometry in laser welding with filler wire process using Taguchi's approach, Optics & Laser Technology, 44(2012), 2020-2025.

94) W.H. Huang, S.J. Chen, J. Xiao, X.Q. Jiang, and Y.Z. Jia. Laser wire-feed metal additive manufacturing of the Al alloy, Optics & Laser Technology, 134(2021), 106627.

95) M.O. Shaikh, C.C. Chen, H.C. Chiang, J.R. Chen, Y.C. Chou, T.Y. Kuo, K. Ameyama, and C.H. Chuang. Additive manufacturing using fine wire-based laser metal deposition, Rapid Prototyping Journal, 26(2020), 473-483.
96) R. Ghanavati and H.N. Moosavy. Additive manufacturing of functionally graded metallic materials: A review of experimental and numerical studies, Journal of Materials Research and Technology, 13(2021), 1628-1664.
97) A.D. Plessis, S.M.J. Razavi, M. Benedetti, and et al. Properties and applications of additively manufactured metallic cellular materials: A review, 125(2022), 100918.
98) V. Vinoth, S. Sathiyaurthy, U. Natarajan, D. Venkatkumar, J. Prabhakaran, and K.S. Prakash. Examination of microstructure properties of AISI 316L stainless steel fabricated by wire arc additive manufacturing, Materials Today: Proceedings, 2022.
99) D. Zhang, A. Liu, B.Z. Yin, and P. Wen. Additive manufacturing of duplex stainless steels - A critical review, 73(2022), 496-517.
100) A.H. Ettefagh, S.M. Guo, and J. Raush. Corrosion performance of additively manufactured stainless steel parts: A review, 37(2021), 101689.
101) C.M. Xu, Y.H. Zhang, G.X. Cheng, and W.S. Zhu. Localized corrosion behavior of 316L stainless steel in the presence of sulfate-reducing and iron-oxidizing bacteria, Materials Science and Engineering: A, 443(2007), 235-241.
102) S. Ocylok, M. Leichnitz, S. Thieme, and S. Nowotny. Investigations on laser metal deposition of stainless steel 316L with coaxial wire feeding, 9th International Conference on Photonic Technologies LANE, 2016.
103) Z.H. Hu, H.H. Zhu, H. Zhang, and X.Y. Zeng. Experimental investigation on selective laser melting of 17-4PH stainless steel, Optics & Laser Technology, 87(2017), 17-25.
104) T. Lebrun, K.C. Tanigaki, K. Horikawa, and H. Kobayashi. Strain rate sensitivity and mechanical anisotropy of selective laser melted 17-4 PH stainless steel, The Japan Society of Mechanical Engineers, 2014.
105) V.T. Le, D.S. Mai, T.K. Doan, and H. Paris. Wire and arc additive manufacturing of 308L stainless steel components: Optimization of processing parameters and material properties, Engineering Science and Technology, an International

Journal, 24(2021), 1015-1026.
106) M. Li, T. Lu, J.W. Dai, X.J. Jia, X.H. Gu, and T. Dai. Microstructure and mechanical properties of 308L stainless steel fabricated by laminar plasma additive manufacturing, Materials Science and Engineering: A, 770(2020), 138523.
107) D.X. Wen, P. Long, J.J. Li, L. Huang, and Z.Z. Zheng. Effects of linear heat input on microstructure and corrosion behavior of an austenitic stainless steel processed by wire arc additive manufacturing, Vaccum, 173(2020),109131.
108) X.H. Chen, J. Li, X. Cheng, H.M. Wang, and Z. Huang. Effect of heat treatment on microstructure mechanical and corrosion properties of austenitic stainless steel 316L using arc additive manufacturing, Materials Science and Engineering: A, 715(2018), 307-314.
109) N. Chen, G.Q. Ma, W.Q. Zhu, A. Godfrey, Z.J. Shen, G.L. Wu, and X.X. Huang. Enhancement of an additive-manufactured austenitic stainless steel by post-manufacture heat-treatment, 759(2019), 65-69.
110) V. Dhinakaran, J. Ajith, A. Fathima Yasin Fahmidha, T. Jagadeesha, T. Sathish, and B. Stalin. Wire Arc Additive Manufacturing (WAAM) process of nickel based superalloys- A review, Materials Today: Proceedings, 21(2020), 920-925.
111) C.E. Seow, J. Zhang, H.E. Coules, G.Y. Wu, C. Jones, J.L. Ding, and S. Williams. Effect of crack-like defects on the fracture behaviour of Wire + Arc Additively Manufactured nickel-base Alloy 718, Additive manufacturing, 36(2020).
112) D. Clark, M.R. Bache, and M.T. Whittaker. Shaped metal deposition of a nickel alloy for aero engine applications, Journal of Materials Processing Technology, 203(2008), 439-448.
113) M. Rombouts, G. Maes, M. Mertens, and W. Hendrix. Laser metal deposition of Inconel 625: Microstructure and mechanical properties, Journal of Laser Application, 24(2012), 2575-2581.
114) S. Li, Q.S. Wei, Y.S. Shi, Z.C. Zhu, and D.Q. Zhang. Microstructure Characteristics of Inconel 625 Superalloy Manufactured by Selective Laser Melting, Journal of Materials Science & Technology, 9(2015), 946-952.
115) B. Baufeld. Mechanical Properties of INCONEL 718 Parts Manufactured by Shaped Metal Deposition(SMD), Journal of Materials Engineering and Performance, 21(2012), 1416-1421.
116) J.F. Wang, Q.J. Sun, H. Wang, J.P. Liu, and J.C. Feng. Effect of location on

microstructure and mechanical properties of additive layer manufactured Inconel 625 using gas tungsten arc welding, Materials Science & Engineering A, 676(2016), 395-405.

117) F.J. Xu, Y.H. Lv, Y.X. Liu, F.Y. Shu, P. He, and B.S. Xu. Microstructure Evolution and Mechanical Properties of Inconel 625 Alloy during Pulsed Plasma Arc Deposition Process, Journal of Materials Science & Technology, 29-5(2013), 480-488.

118) Y.H. Wang, X.Z. Chen, and S.V. Konovalov. Additive Manufacturing Based on Welding Arc: A low-Cost Method, Journal of Surface Investigation: X-ray, Synchrotron and Neutron Techniques, 11(2017), 1317-1328.

119) P. Jia, E.G. Wang, H. Lu, and J.C. He. Effect of electromagnetic field on microstructure and mechanical property for Inconel 625 superalloy, Acta Metallurgica Sinica, 49(2013), 1573-1580.

120) Y.F. Wang, X.Z. Chen, Q.K. Shen, C.C. Su, Y.P. Zhang, S. Jayalakshmi, and R.A. Singh. Effect of magnetic Field on the microstructure and mechanical properties of Inconel 625 superalloy fabricated by wire arc additive manufacturing, Journal of Manufacturing Processes, 64(2021), 10-19.

121) K.N. Amato, J. Hernandez, L.E. Murr, E. Martinez, S.M. Gaytan and P.W. Shindo. Comparison of Microstructures and Properties for a Ni-Base Superalloy(Alloy 625) Fabricated by Electron and Laser Beam Melting, Journal of Materials Science Research, 1(2012), 435-438.

122) S.A. Jawade, R.S. Joshi, and S.B. Desai. Comparative study of mechanical properties of additively manufactured aluminum alloy, Materials Today: Proceedings, 46(2021), 9270-9274.

123) S.C. Altıparmak, V.A. Yardley, Z.S. Shi, and J.G. Lin. Challenges in additive manufacturing of high-strength aluminium alloys and current developments in hybrid additive manufacturing, International Journal of Lightweight Materials and Manufacture, 4(2021), 246-261.

124) X.W. Fang, L.J. Zhang, G.P. Chen, K. Huang, F. Xue, L. Wang, J.Y. Zhao, and B.H. Lu. Microstructure evolution of wire-arc additively manufactured 2319 aluminum alloy with interlayer hammering, Materials Science & Engineering A, 800(2021), 140168.

125) D.H. Ding, R.Z. Zhao, Q.H. Lu, Z.X. Pan, H.J. Li, K. Wang, and K.F. He. A shape control strategy for wire arc additive manufacturing of thin-walled aluminium structures with sharp corners, Journal of Manufacturing Processes, 64(2021), 253-264.

126) S.Y. Zhou, Y. Su, H. Wang, J. Enz, T. Ebel, and M. Yan. Selective laser melting

additive manufacturing of 7xxx series Al-Zn-Mg-Cu alloy: Cracking elimination by co-incorporation of Si and TiB_2, Additive Manufacturing, 36(2020), 101458.

127) A. Mehta, L. Zhou, T. Huynh, S. Park, H. Hyer, S.T. Song, Y.L. Bai, D.D. Imholte, N.E. Woolstenhulme, D.M. Wachs, and Y.H. Sohn. Additive manufacturing and mechanical properties of the dense and crack free Zr-modified aluminum alloy 6061 fabricated by the laser-powder bed fusion, Additive Manufacturing, 41(2021), 101966.

128) B.L. Dong, X.Y. Cai, S.B. Lin, and C.L. Fan. Microstructures and mechanical properties of wire arc additive manufactured 5183-Al: Influences of deposition dimensions, CIRP Journal of Manufacturing Science and Technology, 35(2021), 744-752.

129) Y.M. Huang, D.J. Zhao, H.B. Chen, L.J. Yang, and S.B. Chen. Porosity detection in pulsed GTA welding of 5A06 Al alloy through spectral analysis, Journal of Materials Processing Technology, 259(2018), 332-340.

130) T. Hauser, R.T. Reisch, P.P. Breese, B.S. Lutz, M. Pantano, Y. Nalam, K. Bela, T. Kamps, J. Volpp, A.F.H. Kaplan. Porosity in wire arc additive manufacturing of aluminium alloys, Additive Manufacturing, 41(2021), 101993.

131) M. Schuster, A.D. Luca, A. Mathur, E. Hosseini, and C. Leinenbach. Precipitation in a 2xxx series Al-Cu-Mg-Zr alloy fabricated by laser powder bed fusion, Materials & Design, 211(2021), 110131.

132) R. Fu, S.Y. Tang, J.P. Lu, Y.N. Cui, Z.X. Li, H.R. Zhang, T.Q. Xu, Z. Chen, and C.M. Liu. Hot-wire arc additive manufacturing of aluminum alloy with reduced porosity and high deposition rate, Materials & Design, 199(2021), 109370.

133) N.T. Aboulkhair, M. Simonelli, L. Parry, I. Ashcroft, C. Tuck, and R. Hague. 3D printing of Aluminium alloys: Additive Manufacturing of Aluminium alloys using selective laser melting, Progress in Materials Science, 106(2019), 100578.

134) K. Shinozaki, M. Yamamoto, Y. Nagamitsu, T. Uchida, K. Mitsuhata, T. Nagashima, T. Kanazawa, and H. Arashin. Melting Phenomenon during Ultra-High-Speed GTA Welding Method using Pulse-heated Hot-wire, Quarterly Journal of The Japan Welding Society, 27(2009), 22-26.

135) K. Hori, H. Watanabe, T. Myoga, and K. Kusano. Development of Hot Wire TIG Welding Methods Using Pulsed Current to Heat Filler Wire, Quarterly Journal of

The Japan Welding Society, 21(2003), 362-373.

136) K. Hori, H. Watanabe, T. Myoga, and K. Kusano. Development of hot wire TIG welding methods using pulsed current to heat filler wire – research on pulse heated hot wire TIG welding processes, Welding International, 18(2004), 456-468.

137) K. Shinozaki, M. Yamamoto, K. Mitsuhata, T. Nagashima, T. Kanazawa, and H. Arashin. Bead formation and wire temperature distribution during Ultra-High-Speed GTA Welding using pulse-heated hot-wire, welding in the world, 55(2011), 12-18.

138) W. Liu, S. Liu, J.J. Ma, and R. Kovacevic. Real-time monitoring of the laser hot-wire welding process. Optics & Laser Technology. 57(2014), 66–76.

139) P. Wen, Z.P. Cai, Z.H. Feng, and G. Wang. Microstructure and mechanical properties of hot wire laser clad layers for repairing precipitation hardening martensitic stainless steel, 75(2015), 207-213.

140) M. Yamamoto, K. Shinozaki, K. Kadoi, D. Fujita, T. Inoue, M. Fukahori, and Y. Kitahara. Development of Hot-wire Laser Welding Method for Lap Joint of Steel Sheet with Wide Gap, Quarterly Journal of The Japan Welding Society, 29(2011), 58-61.

141) R. Phaoniam, K. Shinozaki, M. Yamamoto, K. Kadoi, S. Tsuchiya, and A. Nishijima. Development of a highly efficient hot-wire laser hybrid process for narrow-gap welding—welding phenomena and their adequate conditions, Welding in the World, 57(2013), 607-613.

142) K. Kadoi, K. Shinozaki, M. Yamamoto, K. Owaki, K. Inose, and D. Takayanagi. Development of High-efficiency / High-quality Hot-wire Laser Fillet Welding Process, Quarterly Journal of The Japan Welding Society, 29(2011), 62-65.

143) M. Todo, K. Shinozaki, M. Yamamoto, K. Kadoi, M. Yamamoto. R. Phaonaim, and T. Okagaito. Hot-wire Laser Welding Process Using Laser Diode for Large-Diameter Pipe with Narrow Gap Joint. Quarterly Journal of The Japan Welding Society, 33(2015), 107-110.

144) M. Bambach, I. Sizova, F. Silze, and M. Schnick. Comparison of laser metal deposition of Inconel 718 form powder, hot and cold wire, 10th CIRP Conference on Photonic Technologies, 74(2018), 206-209.

145) Z.G. Nie, G. Wang, J.D.M. Cawley, B. Narayanan, S.J. Zhang, D. Schwam, M. Kottman, and Y.M.K. Rong. Experimental study and modeling of H13 steel

deposition using laser hot-wire additive manufacturing, Journal of Materials Processing Technology, 235(2016), 171-186.

146) J. Nurminen, J. Riihimäki, J. Näkki, and P. Vuoristo. Comparison of laser cladding with powder and hot and cold wire techniques, ICALEO, 1006, 2006.

147) H.Y. Wei, Y. Zhang, L.P. Tan, and Z.H. Zhong. Energy efficiency evaluation of hot-wire laser welding based on process characteristic and power consumption, Journal of Cleaner Production, 87(2015), 255-262.

148) Z.X. Li, C.M. Liu, T.Q. Xu, L. Ji, D.H. Wang, J.P. Lu, S.Y. Ma, and H.L. Fan. Reducing arc heat input and obtaining equiaxed grains by hot-wire method during arc additive manufacturing titanium alloy, Materials Science and Engineering: A, 742(2019), 287-294.

149) F. Martina, J. Mehnen, S.W. Williams, P. Colegrove, and F. Wang. Investigation of the benefits of plasma deposition for the additive layer manufacture of Ti–6Al–4V, Journal of Materials Processing Technology, 212(2012), 1377-1386.

150) T.A. Rodrigues, N. Bairrão, F.W.C. Farias, and et al. Steel-copper functionally graded material produced by twin-wire and arc additive manufacturing (T-WAAM), Materials & Design, 213(2022), 110270.

151) P. Poolperm, W. Nakkiew, and N. Naksuk. Experimental Investigation of Additive Manufacturing Using a Hot-Wire Plasma Welding Process on Titanium Parts, Materials, 14(2021), 1270.

152) S. Charunetratsamee, E. Warinsiriruk, K. Shinozaki, and M. Yamamoto. Melting by Reflected Laser Beam during Vertical Welding via Hot-Wire Laser Welding. Quarterly Journal of The Japan Welding Society, 37(2019), 208–214.

153) S. Takaya, M. Yamamoto, K. Shinozaki, H. Matsuda, and R. Ikeda. Hot-wire Laser Brazing Technology for Steel/Aluminum Alloy Dissimilar Joint. Quarterly Journal of The Japan Welding Society, 35(2017), 255–159.

154) M. Xiao, C.K. Gao, C.W. Tan, Y.X. Zhao, H.B. Liu, and J. Yang. Experimental and numerical assessment of interfacial micro-structure evolution in dissimilar Al/steel joint by diode laser welding-brazing. Optik. 245(2021), 167706.

155) S. Kono. Development of Addictive Manufacturing Technology Using High-power Diode Laser and Hot-wire Method, Hiroshima university, 2019.

156) J. Beddoes and J.G. Parr. Stainless Steel Handbook 3rd Edition, Stainless Steel Association, ASM International, 1999.

157) O. Outokumpu. Handbook of Stainless Steel, Sandvikens Tryckeri AB, Sweden, 2013.
158) J.C. Lippold and D.J. Kotecki. Welding Metallurgy and Weldability of Stainless Steels, USA, 2004.
159) Metal Data Book, Japan Metal Society Vol. 3, Japan, 1993.
160) Aluminum Handbook, Japan Institute of Light Metals, Japan, 2007.
161) S. Sabooni, A. Chabok, S.C. Feng, H. Blaauw, T.C. Pijper, H.J. Yang, and Y.T. Pei. Laser powder bed fusion of 17–4 PH stainless steel: A comparative study on the effect of heat treatment on the microstructure evolution and mechanical properties, Additive Manufacturing, 46(2021), 102176.
162) W.J. Oh, Y. Son, S.Y. Cho, S.W. Yang, G.Y. Shin, and D.S. Shim. Solution annealing and precipitation hardening effect on the mechanical properties of 630 stainless steel fabricated via laser melting deposition, Materials Science and Engineering: A, 794(2020), 139999.
163) L. Carneiro, B. Jalalahmadi, A. Ashtekar, and Y.Y. Jiang. Cyclic deformation and fatigue behavior of additively manufactured 17–4 PH stainless steel, International Journal of Fatigue, 123(2019), 22-30.
164) A. Caballero, J.L. Ding, S. Ganguly, and S. Williams. Wire + Arc Additive Manufacture of 17-4 PH stainless steel: Effect of different processing conditions on microstructure, hardness, and tensile strength, Journal of Materials Processing Technology, 268(2019), 54-62.
165) Z.H. Hu, H.H. Zhu, H. Zhang, and X.Y. Zeng. Experimental investigation on selective laser melting of 17-4PH stainless steel, Optics & Laser Technology, 87(2017), 17-25.
166) T. LeBrun, T. Nakamoto, K. Horikawa, and H. Kobayashi. Effect of retained austenite on subsequent thermal processing and resultant mechanical properties of selective laser melted 17–4 PH stainless steel, Materials & Design, 81(2015), 44-53.
167) T.E. Abioye, J. Folks, and A.T. Clare. A parametric study of Inconel 625 wire laser deposition, Journal of Materials Processing Technology, 213(2013), 2145-2151.
168) S.B. Zhao, L.J. Yang, Y.M. Huang, and S. Xu. Feasibility study of producing Ni/WC composite coatings by laser deposition with a tubular cored wire. Journal of Materials Processing Technology, 285(2020), 116745.

Published or Submitted Papers in Regard to This Thesis

1. **S. Zhu,** Y. Nakahara, H. Aono, R. Ejima, and M. Yamamoto: “Derivation of Appropriate Conditions for Additive Manufacturing Technology using Hot-wire Laser Method”, Materials Proceedings, 2021, 3(1), 9. (Chapter 4 & 5)

2. **S. Zhu,** Y. Nakahara, and M. Yamamoto: “Optimization of Process Conditions for Additive Manufacturing Technology Combining High-Power Diode Laser and Hot Wire”, Metals, 2021, 11(10), 1583. (Chapter 4 & 5)

3. **S. Zhu,** Y. Nakahara, M. Yamamoto, K. Shinozaki, H. Aono, R. Ejima: “Additive Manufacturing Phenomena of Various Wires using Hot-wire and Diode Laser”, Welding in the World, 2022. (Chapter 3 & 5)

Presentations

1. **S. Zhu,** Y. Nakahara, M. Yamamoto, K. Shinozaki, H. Aono, R. Ejima: “Development of High-efficiency Additive Manufacturing Technology using High-power Diode Laser and Hot-wire”, National Conference of Japan Welding Society, Kobe Hyogo ken, Japan, 2020. (Chapter 3 & 4)

2. **S. Zhu,** Y. Nakahara, H. Aono, R. Ejima, and M. Yamamoto: “Derivation of Appropriate Conditions for Additive Manufacturing Technology using Hot-wire Laser Method”, The 1st International Electronic Conference on Metallurgy and Metals (IEC2M), Basel, Switzerland, 2021. (Chapter 4 & 5)

3. **S. Zhu,** Y. Nakahara, M. Yamamoto, K. Shinozaki, H. Aono, R. Ejima: “Highly Efficient Additive Manufacturing Phenomena of Various Wires using Hot-wire and Diode Laser”, 74th IIW Annaual Assembly and International Conference, Japan, Genoa, Italy, 2021. (Chapter 3 & 5)